X-ray Magnetic Circular Dichroism and Scanning Tunnelling Microscopy applied to Molecular Spintronics

Thesis submitted in accordance with the requirements of the University of Liverpool for the degree of Doctor in Philosophy by:

Gary Ledger

Supervised at the University of Liverpool by

Professor Rasmita Raval

Dr Steve D Barrett

Supervised at the Diamond Light Source by

Professor Sarnjeet Dhesi

October 2017

Abstract

X-RAY MAGNETIC CIRCULAR DICHROISM AND SCANNING TUNNELLING MICROSCOPY APPLIED TO MOLECULAR SPINTRONICS BY GARY LEDGER

The PhD project is a joint collaboration between the Surface Science Research Centre at the University of Liverpool (supervised by Prof. Rasmita Raval and Dr Steve Barrett) and the Diamond Light Source (DLS), Didcot (supervised by Prof. Sarnjeet Dhesi). The aims of the project are to more fully understand the magnetic sites in organic molecular structures; particularly porphyrin-metal systems grown on the Cu(110) surface. A combination of surface science techniques and synchrotron-based X-ray methods provides all the capabilities to grow, characterise and ultimately investigate the magnetic behaviour of such systems for applications in molecular spintronics.

The PhD project focused predominantly on metal-porphyrin systems grown on Cu(110). The first molecule studied was cobalt-tetraphenyl porphyrin (CoTPP) which forms a range of 2-dimensional supra-molecular assemblies on the Cu(110) surface. The system was reproduced at the DLS and by using X-Ray Magnetic Circular Dichroism (XMCD) it was shown that the Co centre remains magnetically active even upon strong chemisorption to the Cu(110) substrate. Additionally, angular dependent measurements determined an in-plane/out-of-plane anisotropy in the magnetic moment of the Co.

In light of this success, the CoTPP molecule was modified to cobalt-diphenyl porphyrin (CoDPP) by removal of two phenyl rings at opposite meso-positions of the CoTPP macrocycle. This new Co-porphyrin system exhibits a wholly different behaviour on the Cu(110) surface with an absence of any 2-dimensional assemblies, unlike its CoTPP counterpart. However, upon annealing the substrate, the CoDPP molecules link together along a preferred [001] direction producing 1-dimensional, chain-like nanowires of up to 20 molecules in length. Once again this system was reproduced at the DLS and tested using XMCD to determine whether this 1-dimensional, structural anisotropy gives rise to any magnetic anisotropy. Preliminary results showed that the Co centre within the molecule is again magnetically active whilst adsorbed onto the surface albeit with a much smaller magnetic moment compared to that of CoTPP.

The smaller magnetic moment on the central Co atom within the CoDPP molecule was attributed to strong interactions between the unpaired electron on the Co atom and the Cu substrate. To explore this, multilayers of CoDPP molecules were deposited onto the Cu(110) surface to produce a system of CoDPP layers not directly interacting with the metal surface. This system was again investigated using XMCD and was found to be the most magnetically active of the systems tested.

Acknowledgements

Table of Contents

1   Introduction and Background

1.1   Spintronics Introduction

1.1.1   Spintronics and Applications

Magnetic materials are of particular interest in the magnetic data storage industry, with an ever increasing demand for smaller devices with greater storage capacity and lower power output. The potential storage capacity of devices can be related to Moore's Law which was first proposed in 1965 [1.1]. Moore's Law gave an outline for the future production of electronic devices since its inception. The prediction was that the number of transistors per unit area, and hence processing power and data storage capacity, would double every year, later refined to every 2 years by Moore himself [1.2]. **Figure 1.1** details the original plots by Moore to show how the number of components within devices was expected to increase. The successful miniaturisation of semi-conductor transistors, using pioneering lithography techniques [1.3], following this meant that Moore's Law was realised and continued to hold true for 40 years resulting in ever increasing amounts of information being stored in a smaller space.
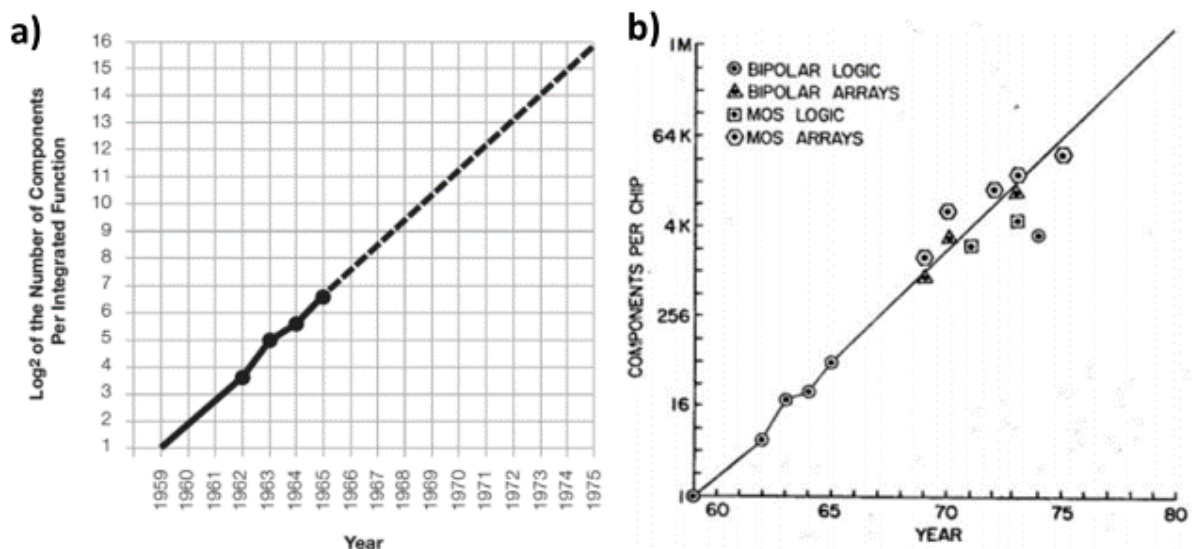
Figure 1.1: Original plots of Moore's Law predictions: a) The plot from [1.1] shows how the number of components per integrated function was suspected to increase from 1965 onwards b) A plot from the refined Moore's Law paper [1.2] showing how the number of components per chip for manufactured devices has increased from 1965-1975 (shown by scatter points on the plot) and how it was expected to continue.

Whilst Moore's Law has been tremendously successful in accurately predicting the sustained development of electronic devices over the years, it has begun to falter more recently. The use of conventional electronics, such as semiconductor transistors, to store ever increasing quantities of information required by current technological applications with more sophisticated software, is becoming less viable. These devices can only be so small and this limiting case is rapidly drawing closer as the length scales of these devices, which are already of the order of nanometers, approach the atomic limit. At this length scale quantum effects become more significant including current leakage caused by electrons which are able to quantum mechanically tunnel through the insulating region of the semiconductors. The 'top-down' approach to making semiconductors smaller and smaller cannot continue in the same fashion for much longer due to this limit.

The reduction in size of devices also introduces issues with heat generation; the increased density of components within a device requires greater energy consumption which leads to vast amounts of residual heat being produced. The amount of heat generated far outweighs the capabilities of cooling systems within current electronics. This has already imposed limits on the processing power of microchips which in 2004 began to have their clocking speeds restricted in order to reduce residual heat output [1.4]. It is now imperative that device technology must evolve and explore innovative methods of information storage and it has been suggested that Moore's Law may even be abandoned completely for the pursuit of these novel technologies [1.5].

One key, new development is the emerging field of spintronics where devices exploit the spin of an electron to gain additional functionality, in contrast to conventional electronics where only the charge on the electron is utilised. The spin of electrons can be easily manipulated using external magnetic fields to align them in a particular direction and by doing so information can be stored based upon these known electron spin orientations. There are many advantages of this approach including lower energy consumption and vastly

increased information storage capacity per unit area [1.6]. This approach to information storage became more viable after the discovery of the giant magnetoresistance (GMR) effect [1.7, 1.8]. The GMR effect is observed in materials consisting of 2 thin layers of ferromagnetic material, separated by a non-magnetic layer. The magnetisation of the ferromagnetic layers can be manipulated to change the electrical resistance across the material: when the magnetisation directions in the 2 ferromagnetic layers are parallel the electrical resistance of the material is low yet when the magnetisation directions in the 2 ferromagnetic layers are antiparallel then the electric resistance is vastly increased. This means that the direction of magnetisation of ferromagnetic layers within the structure has an influence on how easily an electron, and hence current flow, can travel through the material. The magnetisation of the ferromagnetic layers can be modified by using an external magnetic field such that the flow of electrons through the structure can be controlled. GMR represented one of the first demonstrations of spin-dependent electron transport through a material and once suitable materials which exhibited this effect at room temperature were discovered using Co/Cu multilayers [1.9, 1.10], devices began to be readily developed to take advantage of the effect [1.11].

Concurrently to the discovery of the GMR effect, it was found that spin-polarised electrons could be injected and measured within other magnetic materials [1.12] opening up an additional method of spin-dependent electron transport. In this instance, the interface between a ferromagnetic metal adjacent to a paramagnetic metal can induce a coupling between the charge of an electron and its spin leading to a spin-polarised flow of electrons across the interface. Analogous to the GMR effect, electron transport could now be controlled through a material by using external magnetic fields to influence the magnetisation of the ferromagnetic metal and subsequently the spin-polarisation of the electrons. The ability to spin-polarise electrons meant that their magnetic moments could be orientated along a desired vector by changing the magnetisation of the ferromagnetic metal and would remain as such whilst travelling through the paramagnetic metal. As the spin-polarised electrons travel through the paramagnetic metal they retain the original orientation of

their magnetic moments and this can be measured. This effect gives an unprecedented level of spin-dependent sensitivity to electron currents within materials and offers applications for spin-dependent sensors, spin valves and even spin transistors [1.13].

The development of spintronic devices has continued since the discovery of these phenomena and are now prolific in modern day technology [1.14]. Devices such as MRAM chips became able to successfully store information by manipulating the spin of electrons within magnetic materials and able to retain this information even when the device itself is switched off [1.15]. So far, spintronic devices have been largely based on solid-state materials consisting of multilayer structures of ferromagnetic metals which can exhibit a magneto-resistive effect for functionality [1.16]; however, it has been suggested that molecular-based spintronics devices could confer numerous benefits over their solid-state counterparts [1.17]. The molecular approach to spintronics is the focus of this PhD project.

1.1.2 Molecular Spintronics

Molecules, due to their natural nanoscale size, offer an alternative route to miniaturisation via a 'bottom-up' approach and are as such an important consideration in developing spintronic materials [1.18]. Molecules have unique properties compared to conventional inorganic magnetic materials which can be utilised to provide more control over their resulting magnetic properties and functionality to enable them to fulfil a desired role [1.19]. Molecules can be more readily synthesised and modified to alter their properties due to the rich chemistry associated with their organic building blocks. This immense flexibility of molecular architectures gives access to a large degree of control when designing molecular spintronic materials; it is theoretically possible to tailor a molecule specifically for an intended function. As well as this, molecular magnetic materials could potentially be mass produced at a much lower cost [1.20] and are as such an attractive option for large-scale technological applications. If

suitable magnetic molecules can be discovered and functionalised then it is highly likely that they can be developed into innovative information-storage devices with unprecedented capabilities [1.21].

The goal of molecular spintronics is to be able to control and manipulate the spin of individual molecules such that each molecule can behave as a distinct storage unit [1.22] which would lead an increase in the storage capability of magnetic materials by several orders of magnitude. The main candidates for this are known as single-molecule magnets which are organometallic molecules consisting of metal ions, surrounded by an organic framework which houses them [1.23]. These metal ions can be transition metals, lanthanides or actinides and act as the carriers of spin in the molecule and give rise to their magnetic functionality. The organic part of the molecules provide a chemically-stable surrounding for these spin-carrying metal centres. **Figure 1.2** shows 2 examples of manganese-based single molecule magnets.
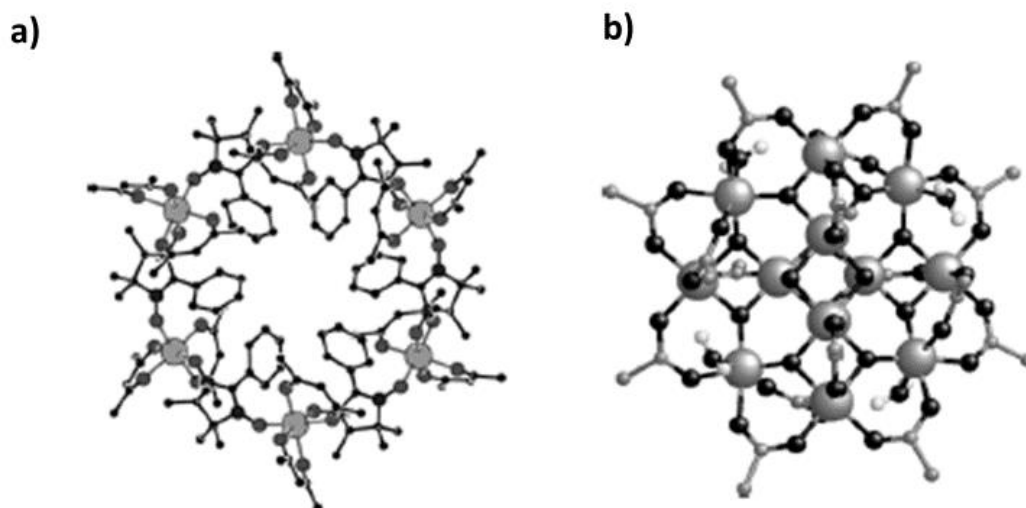
Figure 1.2: Schematics of Manganese-based organic single-molecule magnets: a) [Mn(hfac)$_2$(NITPh)]$_6$ one of the earliest discovered single molecule magnets and b) [Mn$_{12}$O$_{12}$(CH$_3$COO)$_{16}$(H$_2$O)$_4$] a pioneering single-molecule magnet which exhibits long magnetic relaxation times even at high temperatures. Manganese ions are represented by the large grey spheres, enclosed by an organic network. Schematics adapted from [1.20].

The manganese ions in these single-molecule magnets couple with each other magnetically to produce the spin moment on the molecule. In the

case of the $[Mn_{12}O_{12}(CH_3COO)_{16}(H_2O)_4]$ molecule [**Figure 1.2b**], the manganese ions exist as a mix of Mn^{3+} and Mn^{4+} which couple ferrimagnetically with each other leading to an overall net spin state on the molecule. This magnetic coupling only occurs within individual molecules and there is no long range ordering of magnetic spins between molecules which means that each molecule can be considered as a distinct carrier of spin and potentially a single storage unit which was a huge breakthrough for the viability of molecular spintronics. In order to capitalise on this potential, it is necessary to find a template in which molecules can be manipulated and addressed individually so that they can indeed be treated as distinct spin-carrying storage units. One method of achieving this is to use metallic surfaces which these single-molecule magnets can be adsorbed onto to provide an interface of magnetic molecules [1.24].

1.2 Molecular Nanostructures on Surfaces

1.2.1 Ordered Magnetic Nanostructures and Systems

To pursue investigation into molecular spintronics a suitable template is required. One prospect is to translate molecules to a metal surface, producing an interface of magnetic molecules. Ultimately the surface-molecule system will enable information storage via the direct addressing of individual, adsorbed magnetic molecules which behave as single, independent quantum magnets on the surface [1.25]. This approach is particularly fruitful from a research perspective as the resulting systems can be easily probed with a variety of complimentary experimental methods, allowing for a complete exposition of associated properties. These methods include surface-sensitive techniques such as Scanning Tunneling Microscopy (STM) to explore the structural properties of these molecule/surface interfaces and X-Ray Magnetic Circular Dichroism (XMCD) to elucidate magnetic properties of the magnetically active part of the material. These experimental techniques which have been used in this project will be discusses in more detail in **Chapter 2**.

Research into this approach to molecular spintronics has blossomed recently largely due to the development of these surface-sensitive techniques which provide ample information about the structural and magnetic properties of these molecule/surface systems. It has been observed that a large variety of molecular-based materials can be deposited onto metal surfaces to produce an array of surface magnetic materials with a range of properties. Crucially, the magnetic behaviour of the candidate molecules can be retained upon adsorption to the metal surface and is not necessarily quenched when interacting with the surface [1.26] thus validating the viability of this approach to molecular spintronics research.

There are a number of approaches to developing these magnetic molecule/surface materials. One option is to use magnetic molecules which can be deposited onto a metal surface and remain intact upon adsorption and do not interact with each other [1.27]. In this case the surface simply acts as an anchor for the molecule producing an interface of non-interacting independent magnetic molecules which are not ordered on the metal surface. Ordered structures can also be produced such as Co nanorods formed from on surface reactions involving cobalt chloride and sodium oleate which then self-assemble to form a large ordered network [1.28, 1.29]. Another approach is to develop molecules, which already house a metal ion, and which then interact with each other upon adsorption to produce an ordered network. In this case the molecules self-assemble with each other when they are adsorbed onto the surface usually through their organic frameworks [1.30, 1.31]. This approach offers the benefit of being very easy to mass-produce as molecules only need to be deposited onto the surface and readily self-assemble to produce ordered structures. Self-assembled structures offer huge benefit to the viability of these materials in industrial large-scale applications as they readily form their desired structures. Furthermore, having an ordered structure on the surface makes it easier to probe and address individual molecules such as would be the case in a storage device where each molecule represents a unit of information in a

distinct position on the surface. Finally, magnetic networks can be grown directly on the metal surface itself by depositing mixtures of transition metal ions and organic building blocks [1.32]. **Figure 1.3** shows one example of this approach using Fe ions deposited onto a Cu(100) surface along with terephthalic acid (TPA). The Fe and TPA mixture self-assembles as the carboxylic acid groups on the TPA molecule orientate themselves around the Fe ions forming repeating $Fe(TPA)_4$ units across the entire surface shown in **Figure 1.3a**. Interestingly, the magnetic properties of the Fe centres are altered whether it is deposited discretely onto the Cu(100) surface compared to when the TPA is added to form the network. This can be seen in **Figure 1.3b** which shows how the X-Ray Magnetic Circular Dichroism signal (XMCD), which is proportional to the total magnetic moment of the Fe centre, changes when the Fe ions are isolated on the Cu(100) surface or complexed with the TPA molecules. This further reinforces the idea of how molecules can be used to tailor the magnetic properties of these spintronic materials.
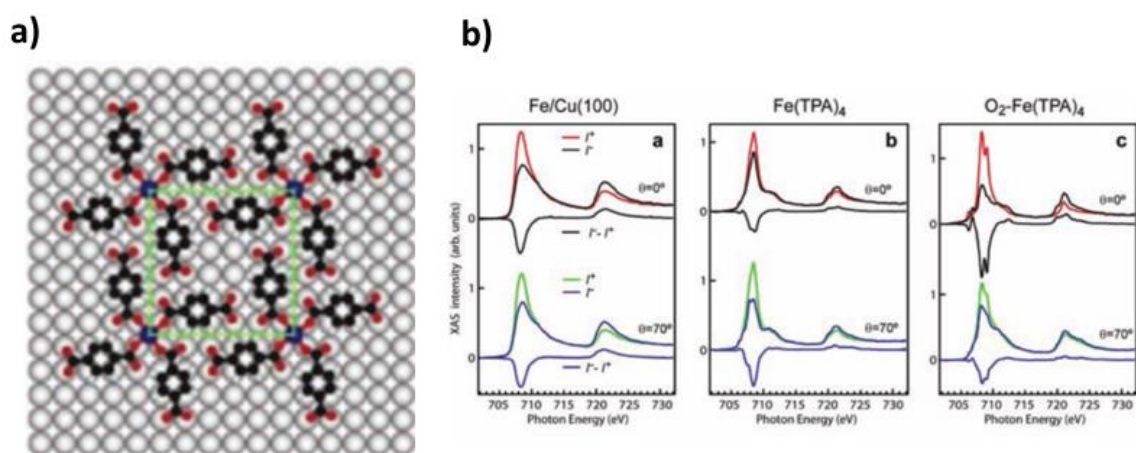
Figure 1.3: The $Fe(TPA)_4$ network on Cu(100) a) A schematic of the $Fe(TPA)_4$ system showing the central Fe ion in blue and the surrounding TPA groups b) Resulting XMCD spectra showing the magnetic behaviour of the central Fe ion when deposited as isolated Fe, Fe within the TPA network and after oxygen adsorption. Taken from [1.32].

1.2.2 Porphyrin-based Magnetic Systems

One family of molecules of particular interest in their potential applications to molecular spintronics are porphyrins. Porphyrin molecules consist of a chemically stable organic tetrapyrrole macrocycle which can house a single metal ion in its centre. They are prolific in nature, performing a wide range of key biological functions such as oxygen-transport in haemoglobin and photo-synthesis in chlorophyll. The porphyrin molecule's ability to fulfil multiple roles is due to the tremendous degree of flexibility in functionalisation of both the central metal ion (for example Fe in haemoglobin and Mg in chlorophyll as shown in **figure 1.4**) and the outer organic macrocycle. For molecular spintronics applications a magnetic functionality is required and as such a magnetic metal ion (such as Fe, Co or Ni) is used. The molecule then acts as a carrier of spin. It is imperative that this spin is preserved upon adsorption onto a substrate in order for the magnetic functionality of the molecule to be maintained.
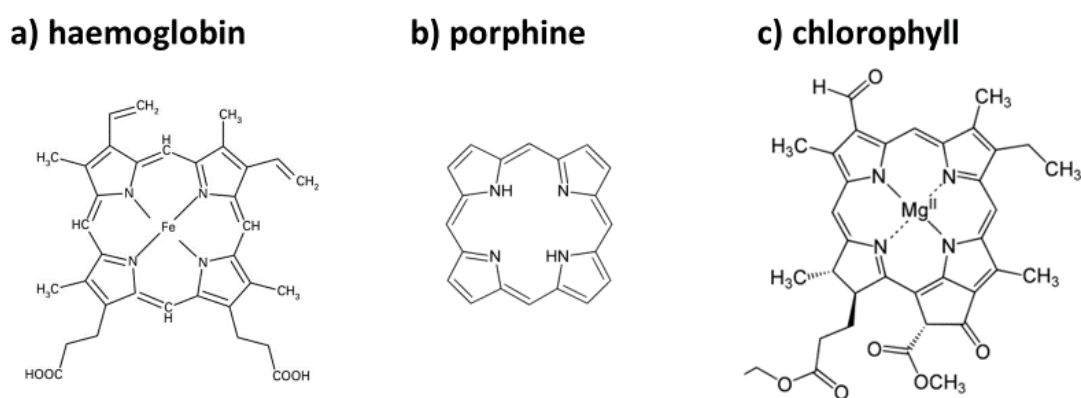
Figure 1.4: The porphine core and example porphyrin-based molecules: a) Haemglobin with a Fe ion core used for oxygen transport b) the porphine core c) Chlorophyll with a Mg ion core use for light harvesting properties. This illustrates the flexibility in functionalising the porphine core to achieve different properties.

Porphyrin molecules readily self-assemble when adsorbed onto metal surfaces forming a variety of different structures [1.33-1.38]. It has been shown that porphyrins, and chemically similar phthalocyanines, can be successfully adsorbed onto a range of non-magnetic metallic substrates including Ag(110) [1.39] and Au(111) [1.40] and also various ferromagnetic substrates such as

11

Co, Ni and Fe [1.41, 1.42] thin films; the substrate playing a critical role in the supramolecular assemblies which form, if any, and also the molecule's observed spin polarisation. As well as the composition of the molecule, such as the central metal ion, the nature of the substrate-metal interaction has a prominent influence on both the structural and magnetic properties of the adsorbed molecules.

A ferromagnetic metal surface can induce magnetic ordering in the metal centres within the molecules. For examples, ferromagnetic Ni and Co thin films grown on non-metallic substrates have been shown to cause alignment of spins in the magnetic centres of the porphyrin molecules and even result in magnetic ordering of the Fe centres [1.43-1.47]. The magnetic moments from the metal ions within the porphyrin molecules couple with those in the adjacent magnetic thin film. In this instance, the magnetisation of the ferromagnetic substrate can be changed and the subsequent magnetisation of the Fe centres within the molecules will align parallel to it allowing their spins to be manipulated. This effect is only observed for molecules in direct contact with the substrate, indicating a very short range of the substrate-metal interaction and the importance of this interaction. These magnetic thin films can also induce magnetic behaviour in other transition metals such as Mn and Co also housed within porphyrins [1.48-1.51]; highlighting the extent of which the substrate can influence the magnetic properties of the adsorbed molecules.

Although magnetic ordering within these molecules can be induced by use of a ferromagnetic substrate, it is not a firm requirement as spin alignment can also be achieved via the use of a strong external magnetic field. This opens up the possibility of using non-magnetic substrates. The substrate-metal interaction still plays a pivotal role in the in the resulting magnetic behaviour of the molecules but in this case use of a non-magnetic substrate can cause the magnetic functionality of the molecule to be quenched. This has been observed for a Co phthalocyanine monolayer adsorbed on Au(111) [1.40] which shows no XMCD signal, indicating no magnetic response to an external field.

This can be explained in terms of the degree of hybridisation of the orbitals involved [1.52, 1.53] in forming the substrate-metal bond: electrons which are unpaired in the metal ion within the molecule in the gas phase are then involved in interactions with the metal substrate upon adsorption and as such the molecule loses magnetic functionality. These observations demonstrate the sensitivity of the magnetic properties of the metal centre to the nature of the substrate-metal bond.

To avoid this quenching of the magnetic properties of the molecule upon adsorption it has been shown that depositing multilayers of molecules on non-magnetic metal surfaces leads to a much larger XMCD signal measured on the metal centre [1.54]. This indicates that a larger magnetic moment is present for molecules deposited on top of the first monolayer, reinforcing the idea that the substrate has quenched the magnetism on directly adsorbed molecules in the first monolayer. Although this approach minimises the effect of the substrate-molecule interaction it also makes the overall structure of the molecules/substrate interface less certain as molecules can stack on top of each other in a variety of ways and as such become disordered which would be undesirable for use in technological applications. There is a compromise between having full structural information on a system and having desired magnetic properties; self-assembled systems often only occur in sub-monolayer coverages.

Another method of modifying the interaction between the magnetic molecules and metal substrate is to use a layer of graphene as an interface between the two. Not only does the graphene layer prevent the magnetic molecules from interacting directly with the metal substrate but the graphene layer itself has unique electronic properties which influences the overall magnetic behaviour of the system [1.55-1.57]. It has been shown that Co porphyrin molecules can be successfully deposited onto the graphene layer and have magnetic properties measurable with XMCD [1.58]. The graphene layer can also mediate magnetic interactions between the metal substrate and the metal ions

13

within the molecule leading to unexpected phenomena such as antiferromagnetic coupling [1.59].

Another avenue to pursue when investigating the molecule-substrate interaction is using some simple surface chemistry [1.60-1.64]. This has been explored by exposing molecule/substrate systems to gases such as NO, CO, NH_3 and O_2 which can bind to the metal centre within the molecule. The gas molecule then acts as an additional ligand on the metal centre and can change the distance between the metal ion and the underlying surface changing the metal ion environment and thus influencing its magnetic behaviour. It has recently been shown that this approach can reduce the size of the XMCD by half [1.65] and even quench it completely [1.66]. For other systems, such as a 2-dimensional $Fe(TPA)_4$ network (mentioned in **Section 1.2.1 figure 1.3**), exposure to O_2 can cause an anisotropic change in the magnetic moment on the Fe [1.32]. One feature of these systems is that by annealing the substrate the gas molecules desorb, restoring the initial magnetic properties of the metal centre. This reversibility makes the process particularly desirable for device applications as it gives a switch-like functionality.

This body of research illustrates that there are a large number of controllable variables which all influence the magnetic properties of these systems: the central metal ion used in the molecule; the organic molecular architecture surrounding the central metal ion; the choice of metallic substrate and the use of additional molecular layers or residual gases to influence the molecule-substrate interaction. This offers a large degree of freedom to explore this area of molecular spintronics.

1.2.3 Ordered Molecular Nanostructures on Cu(110)

This project aims to explore the relationship between the supramolecular structures which are formed when these types of magnetic molecules are

14

adsorbed onto metal substrates and their resulting, if any, magnetic properties. This is done by modifying the organic macrocycle of the candidate molecules, by adding or removing functional groups using organic synthetic techniques, to alter how they interact with each other and the metal substrate upon adsorption to determine the resulting supramolecular structures which are formed.

The Cu(110) substrate was chosen as a template for this study as Cu surfaces are highly reactive which encourages strong interactions between it and adsorbed molecules which often results in self-assembled, highly ordered nanostructures being formed [1.67-1.72]. The viability of this study has recently been explored at the University of Liverpool with a range molecules deposited at sub-monolayer concentration onto the Cu(110) surface. These molecules fall into two distinct categories: purely organic molecules with nitric oxide radical groups (NO) which possess localised unpaired electrons and porphyrin molecules; housing magnetic metals such as cobalt for magnetic functionality. The results of these experiments demonstrate that these molecules can successfully adsorb on Cu(110) to form robust interfaces which are stable at room temperature, thus making them ideal candidates for use in spintronic devices. These prototype systems form the basis of the first stage of the project: determining whether the adsorbed molecules are magnetically active upon adsorption to the Cu(110) substrate.

To explore the behaviour of purely organic systems which utilise the NO radical, the 3-carboxypyrrolidine nitroxide (3CP) molecule which contains an NO group was adsorbed onto Cu(110) [1.74]. Unlike the porphyrin systems, the 3CP molecule doesn't contain any magnetic metal ions, instead it possesses an unpaired electron localised on the NO group. These NO radical groups are essential components in nitronyl nitroxide single molecule magnets [1.20]. They are relatively stable and have previously been used for applications such as spin probes and spin labels. The 3CP molecule has been shown to adsorb onto the Cu(110) surface via bonding through the carboxylate group, anchoring the molecule and, importantly, holding the NO radical upwards away

from the surface. This helps to reduce the interactions between the substrate and the magnetically active NO radical. Density Functional Theory results predict that due to this orientation of the molecule when adsorbed onto the surface, there is a strong likelihood that the spin on the NO radical is preserved. Furthermore, methyl groups attached to the C atoms adjacent to the NO radical help to provide a steric repulsion, effectively isolating the NO radical from other radicals on neighbouring 3CP molecules. The purposefully designed structure of the 3CP molecule should minimise all interactions with the NO radical and help to preserve its unpaired spin. Whilst this system is particularly interesting for molecular spintronic research, as it uses no metal ions for magnetic functionality, this also means that the system is difficult to investigate using XMCD which is primarily used to elucidate the magnetic properties of metals. As such this project focuses instead on the porphyrin structures which form on Cu(110) which can contain magnetic centres easily probed with XMCD.

The porphyrin-based molecules have been shown to form a variety of different structures upon adsorption to the Cu(110) substrate. The cobalt tetra-phenyl porphyrin (CoTPP) molecule has been successfully deposited onto the Cu(110) substrate to form 2-dimensional self-assembled structures [1.75]. The substituent phenyl rings surrounding the porphine core were shown to twist upon adsorption due to strong interactions with the Cu(110) which produce chiral 2-dimensional islands on the substrate. This system is discussed in more detail in **Chapter 3**.

Other porphyrin-based molecules such as the Cu porphyrin molecule and di-phenyl porphyrin have been shown to produce 1-dimensional structures when deposited on Cu(110) and heated [1.76-1.77]. The heating of the substrate causes Cu atoms in the surface to rise up and bridge gaps between the porphine cores, linking them together to form molecular chains as shown in **Figure 1.5**. This system is discussed further in **Chapter 4**.
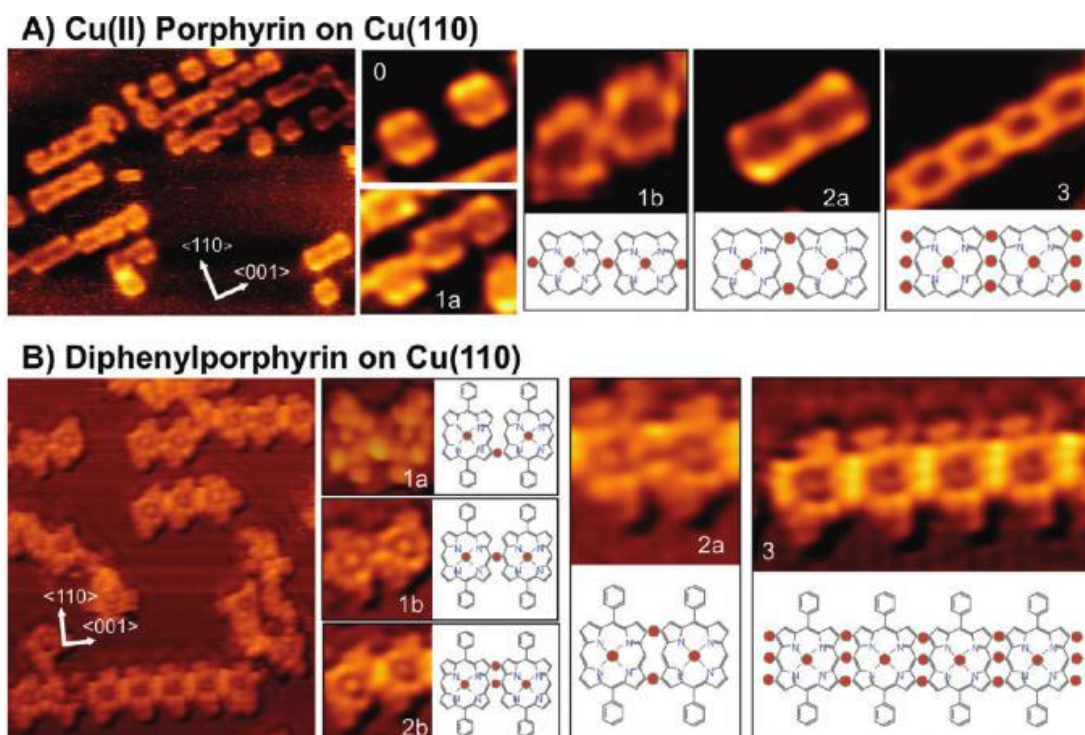
Figure 1.5: Scanning Tunneling Microscopy Images and Schematics showing the 1 dimensional molecular structures of a) Cu(II) Porphyrin and b) Diphenylporphyrin on Cu(110) upon heating. Bridging Cu atoms are visible in the images showing how the molecules link together. Image taken from [1.76].

Finally, the tetra(mesityl) porphyrin molecule adsorbs onto the Cu(110) as isolated molecules which are non-interacting and do not self-assemble at room temperature. However; upon annealing, methyl groups between adjacent molecules covalently bond to link the molecules together forming 2-dimensional networks upon the surface as shown in **Figure 1.6**. These structures are strongly bonded together and can even be seen to diffuse over the Cu(110) surface whilst remaining intact.
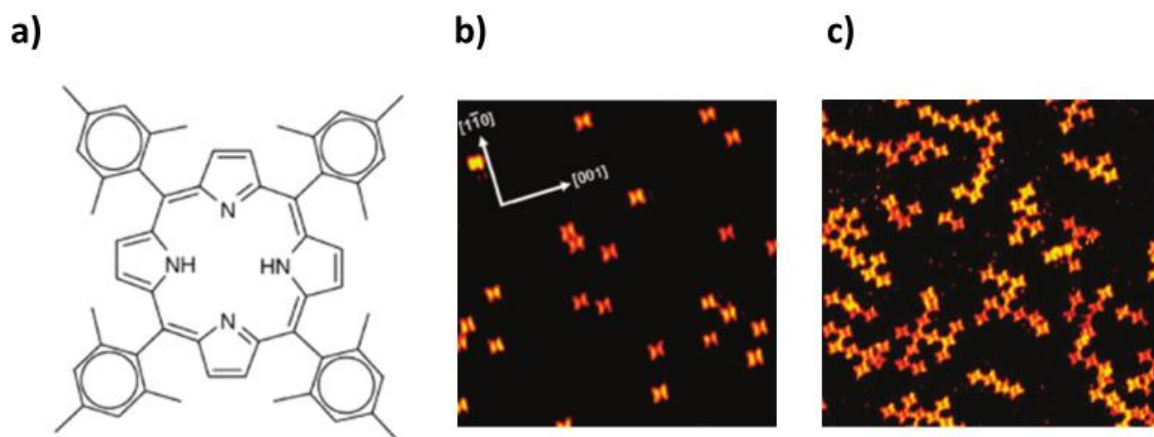
Figure 1.6: Scanning Tunneling Microscopy Images and Schematics showing Tetra(mesityl) porphyrin on Cu(110) a) Schematic of the tetra(mesityl) porphyrin molecule b) STM image of isolated tetra(mesityl) porphyrin molecules upon adsorption at room temperature c) STM image of 2-dimensional networks formed between tetra(mesityl) porphyrin molecules upon heating. Images taken from [1.77].

These experiments into porphyrins on surfaces demonstrate a large range of different nanostructures which have been achieved by altering the organic macrocycle of the porphine core with the porphyrin molecules. The first stage of this PhD project is focused on the CoTPP/Cu(110) system (see **Chapter 3**) to verify if the Co centres of Co-porphyrin systems retain their magnetic properties, even when strongly adsorbed and interacting with Cu(110). This will demonstrate the feasibility of this approach to molecular spintronics. This then opens up the opportunity to pursue investigations into exploring whether Co centres can be added to the other porphyrin systems mentioned on Cu(110) to investigate if the magnetic moment on the active site of these molecules differs based on their new nanostructures. Thus, by implementing the modifications of the Co-porphyrin molecules it should be possible to manipulate the Co environment so that more desirable and more useful magnetic properties are preserved on the Co. The effects of these modifications will then again be tested using XMCD to determine any change in the magnetic behaviour of Co centres.

1.3 Introduction and Background References

[1.1] G. Moore. *Cramming more Components onto Integrated Circuits*. Electronics. 38. 8. (1965).

[1.2] G. Moore. *Progress in Digital Integrated Electronics.* IEDM Tech Digest. 11-13. (1975).

[1.3] G. Moore. *Lithography and the Future of Moore's Law.* Advances in Resist Technology and Processing XII, 2. (1995).

[1.4] V. Victor *et al. Limits to Binary Logic Swtich Scaling – A Gedanken Model.* Proceedings of the IEEE. 91, 11, 1934-1939. (2003).

[1.5] M. M. Waldrop. *The chips are down for Moore's Law.* Nature. 530, 144-147. (2016).

[1.6] S. Wolf; A. Y. Chtchelkanova & D. M. Treger. *Spintronics – A Retrospective and Perspective.* IBM Journal of Research and Development. 50, 101-110. (2006).

[1.7] G. Binasch; P. Grünberg; F. Saurenbach & W. Zinn. *Enhanced Magnetoresistance in Layered Magnetic Structures with Antiferromagnetic Interlayer Exchange.* Phys. Rev. B. 39, 4828-4830. (1989)

[1.8] M. N. Baibich *et al. Giant Magnetoresistance of (001)Fe/(001)Cr Magnetic Superlattices.* Phys. Rev. Lett. 61, 2472-2475. (1988).

[1.9] S. S. P. Parkin; K. P. Roche & T. Suzuki. *Giant Magnetoresistance in Antiferromagnetic Co/Cu Multilayers Grown on Kapton.* J. Appl. Phys. 31, 1246-1249. (1992).

[1.10] S. S. P. Parkin; R. Bhadra & K. P. Roche. *Oscillatory Magnetic Exchange Coupling through Thin Copper Layers.* Phys. Rev. Lett. 66, 2152-2155. (1991).

[1.11] E. Y. Tsymbal & D. G. Pettifor. *Perspectives of Giant Magnetoresistance.* Solid State Physics: Advances in Research and Applications. 56, 113-237. (2001).

[1.12] M. Johnson & R. H. Silsbee. *Interfacial charge-spin coupling: Injection and Detection of Spin Magnetization in Metals.* Phys. Rev. Lett. 55, 1790-1793. (1985).

[1.13] I. Zutic; J. Fabian & S. Das Sarma. *Spintronics: Fundamentals and Applications.* Rev. Mod. Phys. 76, 323-410. (2004).

[1.14] M. Johnson. *Magnetoelectronics.* Elsevier: Oxford Academic Press. 1st Edition. p 205-230. (2004).

[1.15] I. L. Prejbeanu *et al. Thermally Assisted MRAM.* Journal of Physics. 19, 16. (2007).

[1.16] J. Akerman. *Toward a Universal Memory.* Science. 308, 5721, 508-510. (2005).

[1.17] A. R. Rocha *et al. Towards Molecular Spintronics.* Nature Materials. 4, 335-339. (2005).

[1.18] S. Sanvito. *Molecular Spintronics.* Chem. Soc. Rev. 40, 3336-3355. (2011).

[1.19] V. N. Prigodin *et al. New Advances in Organic Spintronics.* Journal of Physics. 292, 121001. (2011).

[1.20] D. Gatteschi; R. Sessoli & J. Villain. *Molecular Nanomagnets.* Oxford University Press. (2006).

[1.21] M. Bazarnik *et al. Toward Tailored All-Spin Molecular Devices.* Nano. Lett. 16, 577-582 (2016).

[1.22] D. Gatteschi *et al. Organizing and Addressing Magnetic Molecules.* Inorg. Chem. 48, 3408-3419. (2009).

[1.23] R. A. Layfield. *Organometallic Single-Molecule Magnets.* Organnometallics. 33, 1084-1099. (2014).

[1.24] M.Mannini. *et al. Magnetic memory of a single-molecule quantum magnet wired to a gold surface.* Nature Materials. 8, 194-197 (2009).

[1.25] M. Mannini *et al. XAS and XMCD Investigation of Mn_{12} Monolayers on Gold.* Chem. Eur. J. 14, 7530-7535. (2008).

[1.26] F. Moro *et al. Addressing the Magnetic Properties of Sub-Monolayers of Single-Molecule Magnets by X-ray Magnetic Circular Dichroism.* Nanoscale. 2, 2698-2703. (2010).

[1.27] S. Stepanow *et al. Spin and Orbital Magnetic Moment Anisotropies of Monodispersed Bis(Phthalocyaninato)Terbium on a Copper Surface.* J. Am. Chem. Soc. Comm. 132, 11900-11901. (2010).

[1.28] K. An *et al. Synthesis, Characterization, and Self-Assembly of Pencil-Shaped CoO Nanorods.* J. Am. Chem. Soc. 128, 9753-9760. (2006).

[1.29] X. D. Ma *et al. Magnetic Properties of Self-Assembled Co Nanorods Grown on Cu(110)-(2x3)N.* Phys. Rev. B. 78, 104420. (2008).

[1.30] T. R. Umbach *et al. Ferromagnetic Coupling of Mononuclear Fe Centres in a Self-Assembled Metal-Organic Network on Au(111).* Phys. Rev. Lett. 109, 267207. (2012).

[1.31] C. Carbone *et al. Self-Assembled Nanometer-Scale Magnetic Networks on Surfaces: Fundamental Interactions and Functional Properties.* Advanced Functional Materials. 21, 7, 1212-1228. (2011).

[1.32] P. Gambardella *et al. Supramolecular Control of the Magnetic Anisotropy in Two-Dimensional high-spin Fe Arrays at a Metal Interface.* Nature Materials. 8, 189-193. (2009).

[1.33] J. M. Gottfried. *Surface Chemistry of Porphyrins and Phthalocyanines.* Surfaces Science Reports. 70, 3, 259-379. (2015).

[1.34] S. Barlow et al. *Scanning Tunneling Microscopy Study of the Structure and Orbital-Mediated Tunneling Spectra of Cobalt(II) Phthalocyanine and Cobalt(II) Tetraphenylporphyrin on Au(111): Mixed Composition Films.* Langmuir 20, 11 (2004).

[1.35] Heim, D. *et al*. Surface-assisted assembly of discrete porphyrin-based cyclic supramolecules. *Nano Lett.* **10**, 122–128 (2009).

[1.36] W. Auwärter *et al. Site-specific electronic and geometric interface structure of Co-tetraphenyl-porphyrin layers on Ag(111).* Phys. Rev. B. 81, 245403 (2010).

[1.37] W. Auwärter *et al. Self-assembly and conformation of tetrapyridyl-porphyrin molecules on Ag(111).* J. Chem. Phys. 124, 194708–194706 (2006).

[1.38] W. Auwärter *et al. Porphyrins at Interfaces.* Nature Chemistry. 7, 105-120. (2015).

[1.39] M. Fanetti *et al. Structure and Molecule-Substrate Interaction in a Co-octaethyl Porphyrin Monolayer on the Ag(110) Surface.* J. Phys. Chem. C. 115, 23, 11560-11568. (2011).

[1.40] S. Stepanow *et al. Mixed-Valence Behavior and Strong Correlation effects of Metal Phthalocyanines Adsorbed on Metals.* Phys. Rev. B. 83, 220401 (2011).

[1.41] K. Eguchi *et al. Magnetic Interactions of Vanadyl Phthalocyanine with Ferromagnetic Iron, Cobalt, and Nickel Surfaces.* J. Phys. Chem. C. 118, 31, 17633-17637. (2014).

[1.42] J. Girovsky *et al. Antiferromagnetic Coupling of Cr-Porphyrin to a bare Co substrate.* Phys. Rev. B. 90, 220404. (2014).

[1.43] H. Wende *et al. Substrate-Induced Magnetic Ordering and Switching of Iron Porphyrin Molecules.* Nature Materials. 6, 516-520. (2007).

[1.44] M. Bernien *et al. Fe-Porphyrin Monolayers on Ferromagnetic Substrates: Electronic Structure and Magnetic Coupling Strength*. Phys. Rev. B. 76, 214406. (2007).

[1.45] K. Baberschke *et al. Magnetic Switching of Fe- Porphyrin Molecules on Adsorbed on Surfaces: An XAFS and XMCD study.* Journal of Physics. 190, 012012 (2009).

[1.46] Bhandary, S. *et al. Manipulation of spin state of iron porphyrin by chemisorption on magnetic substrates.* Phys. Rev. B **88**, 024401 (2013).

[1.47] S. Bhandary *et al. Manipulation of Spin State of Iron Porphyrin by Chemisorption on Magnetic Substrates.* Phys. Rev. B. 88, 024401. (2013).

[1.48] A. Scheybal *et al. Induced Magnetic Ordering in a Molecular Monolayer. Chem. Phys. Lett.* 411, 214-220. (2005).

[1.49] D. Chylarecka *et al. Indirect Magnetic Coupling of Manganese Porphyrin to a Ferromagnetic Cobalt Substrate.* J. Phys. Chem. C. 115, 1295-1301. (2011).

[1.50] M. E. Ali *et al. Tuning the Magnetic Interaction between Manganese Porphyrins and Ferromagnetic Co Substrate through Dedicated Control of the Adsorption.* J. Phys. Chem. C. 113, 32, 14381-14383. (2009).

[1.51] E. Annese *et al. Control of the Magnetism of Cobalt Phthalocyanine by a Ferromagnetic Substrate.* Phys. Rev. B. 84, 174443. (2011).

[1.52] S. Javaid *et al. Impact on Interface Spin Polarization of Molecular Bonding to Metallic Surfaces.* Phys. Rev. Lett. 105, 077201. (2010).

[1.53] N. Ballav *et al. Emergence of On-Surface Magnetochemistry.* J. Phys. Chem. Lett. 4, 14, 2303-2311. (2013).

[1.54] J. Bartolomé *et al. Highly Unquenched Orbital Moment in Textured Fe-Phthalocyanine Thin Films*. Phys. Rev. B. 81, 195405. (2010).

[1.55] W. Han; R. K. Kawakami; M. Gmitra & J. Fabian. *Graphene Spintronics.* Nature Nanotechnology. 9, 794-807. (2014).

[1.56] H. Yang *et al. Anatomy and Giant Enhancement of the Perpendicular Magnetic Anisotrophy of Cobalt-Graphene Heterostructures.* Nano. Lett. 16, 145-151. (2016).

[1.57] A. Candini *et al. Graphene Spintronic Devices with Molecular Nano-magnets.* Nano Letters. 11, 2634-2639. (2011).

[1.58] D. Klar *et al. Field-Regulated Switching of the Magnetization of Co-Porphyrin on Graphene.* Phys. Rev. B. 89, 144411. (2014).

[1.59] C. Hermanns *et al. Magnetic Coupling of Porphyrin Molecules Through Graphene.* Advanced Materials. 25, 25, 3473-3477. (2013).

[1.60] C. Wäckerlin *et al. On-Surface Coordination Chemistry of Planar Molecule Spin Systems: Novel Magnetochemical effects induced by Axial Ligands.* Chem. Sci. 3, 3154. (2012).

[1.61] Wäckerlin, C. *et al. Ammonia coordination introducing a magnetic moment in an on-surface low-spin porphyrin.* Angew. Chem. Int. Ed. **52**, 4568–4571 (2013).

[1.62] Seufert, K. *et al. Cis-dicarbonyl binding at cobalt and iron porphyrins with saddle-shape conformation.* Nature Chem. **3**, 114–119 (2011).

[1.63] H. Kim *et al. Switching and Sensing Spin States of Co-Porphyrin in Bimolecular Reactions on Au(111) Using Scanning Tunneling Microscopy.* ACS Nano. 7, 10, 9312-9317. (2013).

[1.64] Flechtner, K., Kretschmann, A., Steinrück, H-P. & Gottfried, J. M. *NO-induced reversible switching of the electronic interaction between a porphyrin-coordinated cobalt ion and a silver surface.* J. Am. Chem. Soc. **129**, 12110–12111 (2007).

[1.65] J. Miguel *et al. Reversible Manipulation of the Magnetic Coupling of Single Molecular Spins in Fe-Porphyrins to a Ferromagnetic Substrate.* J. Phys. Chem. Lett. 2, 1455-1459 (2011).

[1.66] C. Wäckerlin *et al. Controlling Spins in Adsorbed Molecules by a Chemical Switch.* Nat. Commun. 1, 61. (2010).

[1.67] K. Diller *et al. Self-metalation of 2H-tetraphenylporphyrin on Cu(111): An X-ray spectroscopy study.* J. Chem. Phys. 136, 014705–014713 (2012).

[1.68] Buchner, F. *et al. Diffusion, rotation, and surface chemical bond of individual 2H-tetraphenylporphyrin molecules on Cu(111).* J. Phys. Chem. C **115**, 24172–24177 (2011).

[1.69] Diller, K. *et al. Investigating the molecule-substrate interaction of prototypic tetrapyrrole compounds: Adsorption and self-metalation of porphine on Cu(111).* J. Chem. Phys. **138**,154710–154719 (2013).

[1.70] M. Dyer *et al. Understanding the Interaction of the Porphyrin Macrocycle to Reactive Metal Substrates: Structure, Bonding, and Adatom Capture.* ACS Nano. 5, 3, 1831-1838. (2011).

[1.71] W. Auwärter *et al. Conformational adaptation and selective adatom capturing of tetrapyridyl-porphyrin molecules on a copper (111) surface.* J. Am. Chem. Soc. 129, 11279–11285. (2007).

[1.72] U. Perera *et al. Spatially Extended Kondo State in Magnetic Molecules Induced by Interfacial Charge Transfer.* Phys. Rev. Lett. 105, 106601. (2010).

[1.73] A. Robin *et al. Adsorption and Organization of the Organic Radical 3-Carboxy Proxyl on a Cu(110) Surface.* J. Phys. Chem. C. 113, 13223-13230. (2009).

[1.74] P. Donovan *et al. Unexpected Deformations Induced by Surface Interaction and Chiral Self-Assembly of Co(II)-Tetraphenyl-porphyrin adsorbed on Cu(110).* Chem. Eur. J. 16, 38, 11641-11652. (2010).

[1.75] S. Haq *et al. Clean Coupling of Unfunctionalized Porphyrins at Surfaces To Give Highly Oriented Organometallic Oligomers*. J. Am. Chem. Soc*. 133, 12031-12038. (2011).

[1.76] F. Hanke *et al. Heat-to-Connect: Surface Commensurability Directs Organometallic One Dimensional Self-Assembly.* ACS Nano. 5, 9093-9103. (2011).

[1.77] M. In't Veld *et al. Unique Intermolecular Reaction of Simple Porphyrins at a Metal Surface gives Covalent Nanostructures.* Chemical Commun. 13, 1536-1538. (2008).

2 Surface Science Theory and Experimental Set Up

2.1 Surface Science Theory

2.1.1 Ultra-High Vacuum

The nature of surface science experiments requires that the surfaces that are being investigated are sufficiently clean to ensure that only the desired interactions are being observed. In this case, the interactions we are interested in are the metal surface-molecule interaction and also the interaction between the adsorbed molecules themselves. This necessitates the metal surface remaining free from contaminants so that we can be confident that the molecules we are depositing onto it are interacting directly with the metal atoms of the surface and not with any contaminants that are present. It is also important to be sure that what we are observing on the surface are indeed these molecules that have been intentionally deposited and not any other contaminant molecules which may be difficult to differentiate using STM alone. Furthermore, when conducting X-Ray experiments at the synchrotron light source to investigate the magnetic properties of these molecule-surface structures, we need to be certain that contamination levels remain low throughout the duration of the experiment because remnant gases in the vacuum (such as CO and O_2) could potentially interact with the central cobalt atom in the porphyrin molecules and even alter the measured magnetic properties!

Contaminant molecules will inevitably be adsorbed onto the surface from molecules present within the vacuum chamber itself. The pressure inside the vacuum chamber is directly related to the number of molecules present within the residual gas in the chamber. Subsequently, the pressure within the vacuum chamber is directly related to the number of molecules which strike the surface per unit area per second; the greater the pressure within the vacuum chamber,

the greater the number of molecules striking the surface per unit area per second and the faster the surface will become too contaminated to accurately conduct the experiment. Due to this limitation, the pressure within the chamber needs to be sufficiently low to avoid this unwanted contamination so that the metal surface will remain clean for a timescale comparable to the duration of the experiment. Using the Kinetic theory of ideal gases, it is possible to give an indication of the pressures required to achieve this.

By making the assumption that gases within the chamber behave as ideal gases (the gas particles are in constant random motion and only interact with each other and the walls of the container via elastic collisions) then The Ideal Gas Law can be applied:

$$PV = nRT \tag{2.1}$$

Where P is the pressure (N m^{-2}), V is the volume of the container (m^3), n is the number of moles of gas (mol), R is the ideal gas constant (8.314 J K^{-1} mol^{-1}) and T is the absolute temperature of the gas (K).

In this case we are more interested in actual numbers of molecules rather than number of moles of molecules so the ideal gas law can be rewritten as follows:

$$PV = Nk_BT \tag{2.2}$$

Where k_B is the Boltzmann constant (1.38 x 10^{-23} J K^{-1}) and N is the number of molecules in the gas. Now we are dealing with numbers of molecules,

the number of molecules striking the surface per unit area per unit time can be given by 'impingement rate' [2.1] measured in molecules m^{-2} s^{-1}:

$$\Phi = \frac{\mathcal{N}}{4}\left(\frac{8k_B T}{\pi m}\right)^{\frac{1}{2}}$$

(2.3)

Where m is the molecular mass of the molecule in atomic mass units. The impingement rate gives an indication of molecular flux incident on the surfaces within the chamber and hence it can allow us to determine how quickly a surface will be covered in contaminant molecules if they stick to these surfaces upon colliding with them. In order to accomplish this, we must modify the formula for impingement rate further by using the Ideal Gas Law. By employing this law $\mathcal{N}$, the number density, can be related to pressure P and temperature T as follows:

$$\mathcal{N} = \frac{N}{V} = \frac{P}{k_B T}$$

(2.4)

Substituting this back into the equation for impingement rate (2.3) gives:

$$\Phi = \frac{P}{(2k_B T \pi m)^{\frac{1}{2}}}$$

(2.5)

This equation known as the Hertz-Knudsen equation [2.2] shows that the impingement rate is proportional to the pressure within the container and thus how quickly the surfaces of the container, and crucially the single crystal surface we wish to investigate, will be bombarded by contaminant molecules; lower pressures result in a lower impingement rate and subsequently a lower build of contamination over time. To get an indication of the actual timescale it

will take for these surfaces to become covered in contamination we can consider how long it will take contaminant molecules to form a monolayer on the surface using the following equation:

$$t_m = \frac{\#\ adsorption\ sites/\ m^2}{S\Phi} \tag{2.6}$$

Where t_m is the time taken for a monolayer of contaminant molecules to form, Φ is the impingement rate as defined in equation (2.5) and is S the sticking coefficient of the molecules. The sticking coefficient is a number between 0 and 1 which is related to the probability that a molecule will be adsorbed onto the surface upon collision: a value of 1 indicates that a molecule will always adsorb upon collision and a value of 0 indicates that a molecule will always bounce off the surface upon colliding with it. For the purpose of this calculation we will assume a sticking coefficient of 1, that is to say we will assume every molecule that collides with the surface will stick to it. This is not the case in practice but it will provide a lower limit on how quickly contamination will form upon the surface.

The number of adsorption sites per m^2 for a metal surface such as copper is of the order of 10^{19}. The most prominent residual gases at lower pressures are carbon monoxide (CO) and nitrogen (N_2) which conveniently both have a molecular mass of 28 atomic mass units. Finally, if we assume a temperature of 300 K we can use equation (2.6) to determine the formation time of a monolayer of contaminant molecules at different pressures as follows:

Table 2.1: Build-up of contamination at different pressures at room temperature

Pressure / mbar	Vacuum Type	Impingement rate / molecules m^{-2} s^{-1}	Formation time / s
1000 (atmospheric)	Rough	~ 3 x 10^{27}	~ 3 x 10^{-9}
10	Low	~ 3 x 10^{24}	~ 3 x 10^{-6}
10^{-3}	Medium	~ 3 x 10^{21}	~ 3 x 10^{-3}
10^{-7}	High	~ 3 x 10^{17}	~ 30
10^{-10}	Ultra-High	~ 3 x 10^{14}	~ 30000

From the table it can be seen that at atmospheric pressure the formation time of a layer of contaminant CO / N_2 molecules is only 3 nanoseconds! This means that conducting surface science experiments with any degree of accuracy is unfeasible at higher pressures. Fortunately, as we decrease the pressure, this value also decreases such that at around 10^{-10} mbar pressure the formation time becomes a more manageable 30000s. This timescale is now of the order of hours rather than nanoseconds and provides sufficient amount of time for which a surface can be cleaned and remain clean for the duration of the experiment.

Pressures that lie around the range of 10^{-9} to 10^{-10} mbar are defined as Ultra-High Vacuum (UHV) and achieving these low pressures is a prerequisite to conducting all surface science experiments presented in this thesis. Obtaining pressures within this range is achieved primarily by pumping methods.

2.1.2　　　　**Pumping Systems**

Achieving and maintaining UHV is accomplished using various pumps. To reach the low pressures which these experiments require involves the use of sophisticated pumping systems working in tandem with each other. Different types of pumps function optimally at different pressures and as such we need a suite of different pumps in order to sequentially pump the chamber and lower its pressure until we reach UHV. Despite the numerous advances in pumping technologies, there is no single pump which is able to pump a chamber from atmospheric pressure all the way down to UHV. **Figure 2.1** gives a summary of different pumps used in vacuum systems and also the pressure range at which they function. Pumps highlighted with a red border are those which were used in this project: the rotary mechanical pump, the turbomolecular pump, titanium sublimation pump and the ion sputter pump.

The rotary mechanical pump is a type of roughing pump which can be used at atmospheric pressure and capable of pumping a chamber down to around 10^{-3} mbar. The rotary pump consists of a rotor which moves within a large circular cavity to pump large volumes of material as it rotates [2.4]. In this pressure region, the gases within the chamber act as a viscous fluid as the pressure is high enough that they collide frequently with one another. In this regime, it is possible to pump the gases using a rotary pump; however, as the pressure decreases this assumption becomes less applicable and as such other pumps must be used. At pressures below 10^{-3} mbar, the mean free path of the molecules, that is the average distance travelled without a collision, is comparable to the size of the chamber. This means that molecules no longer frequently collide with each other and instead more frequently collide with the chamber. This regime is called free molecular flow and necessitates different pumping methods in order to further decrease the overall pressure of the chamber.
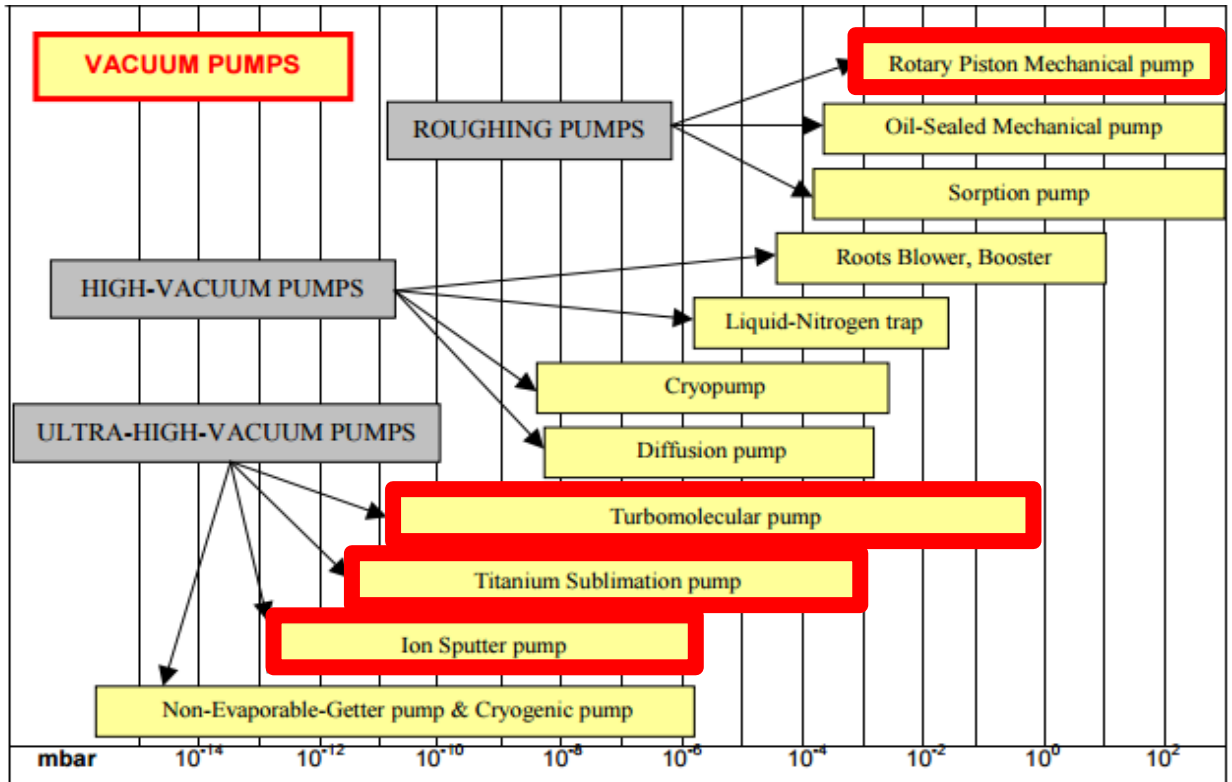
Figure 2.1: A summary of different pumps used to achieve Ultra-High Vacuum and the pressure ranges at which they function. Pumps which are highlighted with a red border are those which have been used for this project. Adapted from [2.3].

The next stage of pumping requires the use of a turbomolecular pump. The turbomolecular pump uses numerous blades in layers which spin at very high velocities and transfer momentum to gas molecules which increases their velocities in a particular desired direction [2.5, 2.6]. The gas molecules proceed to travel deeper within the multi-layered turbomolecular pump until they reach the exhaust where a backing pump removes them from the chamber completely. In practice, rotary and turbomolecular pumps work as a combined system: the rotary pump activates first to initially pump the system to a suitably low pressure at which point the turbomolecular pump is initialised to continue pumping the system down. At this stage, the rotary pump acts as the backing pump for the turbomolecular pump and removes gas molecules from the exhaust. **Figure 2.2** shows the rotary-turbomolecular pump system set up in such a way at the chamber used at the Surface Science Research Centre. The rotary-turbomolecular pump system is able to pump a chamber down to a pressure of around 10^{-9} mbar. At this point the bulk of the gas molecules have been

extracted from the system; however, the composition of the residual gases present at lower pressures is different than the composition of gases at atmospheric pressure and are more difficult to remove using these mechanical pumps. To maintain ultra-high vacuum conditions in this pressure region we employ the use of titanium sublimation pumps and ion sputter pumps.
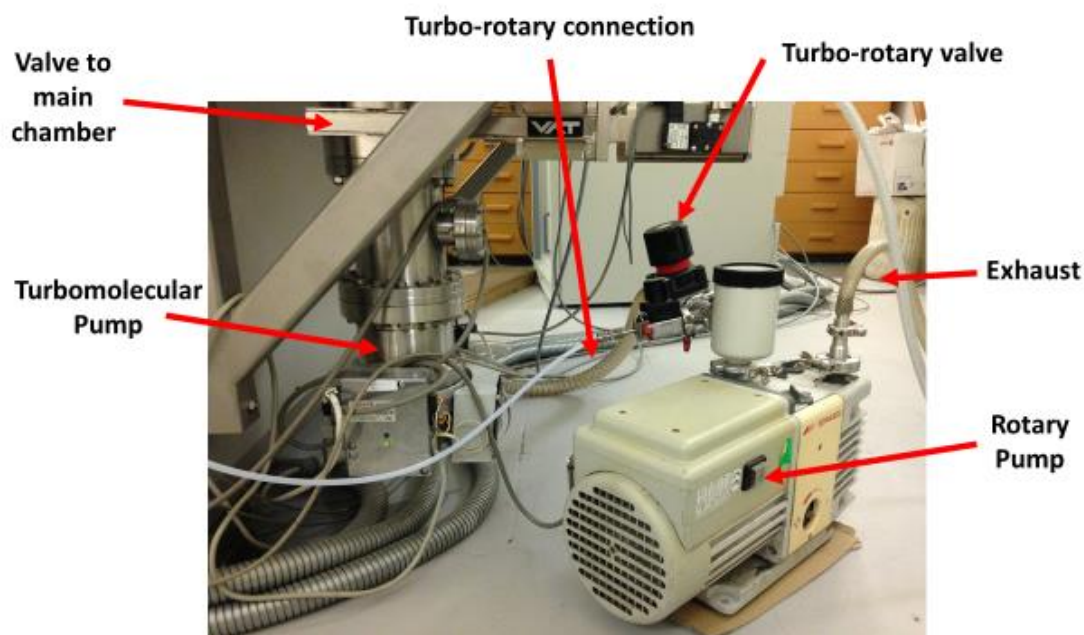

Figure 2.2: The rotary pump and turbomolecular pump tandem setup used at the Surface Science Research Centre. Key features are labelled including valves and connecting pipes.

The titanium sublimation pump (TSP) features a large coil of titanium filament which is heated by passing a current through it. This causes titanium atoms to evaporate from its surface and be ejected into the chamber and coat the surfaces of the chamber with a thin layer of titanium. Titanium atoms are highly reactive and will bind to residual gas molecules as they collide with the titanium surface to form larger structures which will stick to the surface, thus removing the contaminant molecule from the chamber and lowering the pressure. H_2 and H_2O molecules dissociate upon adsorption to the titanium layer: the dissociated H atoms then diffuse throughout the layer whilst the O forms titanium oxides with it. Other residual gas molecules such as CO, N_2 and O_2 all react with the layer to form various compounds which stay embedded in the surface. Whilst effective the TSP is incapable of removing molecules such as

34

noble gases and methane as they simply do not react with the titanium layer and do not become stuck to it.

The last pump used is the ion sputtering pump. The ion pump consists of 2 highly charged cathode plates lying either side of an anode ring. This setup produces an electric field which causes free electrons to rotate and strike with residual gas molecules converting them into positively charged ions. These positively charges ions are then attracted to the negatively charged cathode plates and stick to the plate, removing them from the chamber and lowering the pressure. Much like the rotary and turbomolecular pumps, the TSP and ion pump work well together as the ion pump provides additional surfaces for the titanium from the TSP to form on. The TSP and ion pumps only function optimally in high vacuum conditions as their operation does not actually remove the gas molecules from the chamber but rather capture them in the surface of the walls and charged plates respectively. This means that the pumps are only capable of capturing small, finite numbers of gas molecules and should only be used when the pressure within the chamber is already sufficiently low. Operating these pumps at higher temperatures and pressures quickly causes huge quantities of gas molecules to be adsorbed onto the surfaces and plates and can damage the pumps.

Whilst these pumping methods are effective, they only remove gas molecules which are moving freely within the chamber, they have no influence over gas molecules which are already adsorbed onto the surfaces, particularly water. These molecules are called rest gas molecules and gases such as water are troublesome as they have a high vapour pressure which causes an increase in the pressure of the chamber making it very difficult to achieve UHV conditions. To remove these adsorbed molecules, we heat the entire chamber to temperatures over 100ºC for numerous hours (or even days) as required to allow the molecules to desorb from the surfaces and be pumped out of the chamber. This process is called 'baking' the chamber and is necessary in order to eventually reach UHV conditions once other pumps have been activated.

The bake out itself will run with rotary and turbomolecular pumps running so that the desorbed molecules can be pumped away. Once the chamber has been baked for a sufficiently long time, it then needs time to cool before the other pumps can be utilised without the pressure being too high.

Pressures within the chamber are monitored using a hot-filament ion gauge [2.7]. As the filament is heated, electrons are ejected from it and can collide with gas molecules within the device. This forms gaseous ions which can be focused to a negatively charged collector plate giving rise to a measurable current. The measured current is proportional to the number of molecules present in the ion gauge and is subsequently related to the pressure of the chamber. The ion gauge functions best in the medium to ultra-high vacuum regions (10^{-4} - 10^{-11} mbar); at higher pressures the filament is easily destroyed and electrons will cease to be produced.

2.1.3   Crystal Surfaces

Investigating interactions between surfaces and molecules requires a well-defined surface: we need to fully understand the structure of the surface before we can begin to explore how it interacts with molecules adsorbed onto it. Metal single crystals offer excellent candidate substrates as they are well understood and have ordered structures with well-defined crystal unit cells. It is possible to define planes within these crystal unit cells using Miller Indices which take the form (*hkl*) where *h*, *k* and *l* are integers which denote the reciprocal values at which the plane intersects with the x,y and z axes of the crystal unit cell respectively. For example, if (*hkl*) are (110) this would correspond to a plane which intersects the x axis at x = 1, the y axis at y = 1 and parallel to the z axis. **Figure 2.3** shows the orientation of the x, y ,z coordinate system with respect to a simple cubic crystal structure (atoms lying at each vertex of the cubic unit cell). The figure also shows the orientation of the (110) plane and the positions at which is intersects the x and y axes.
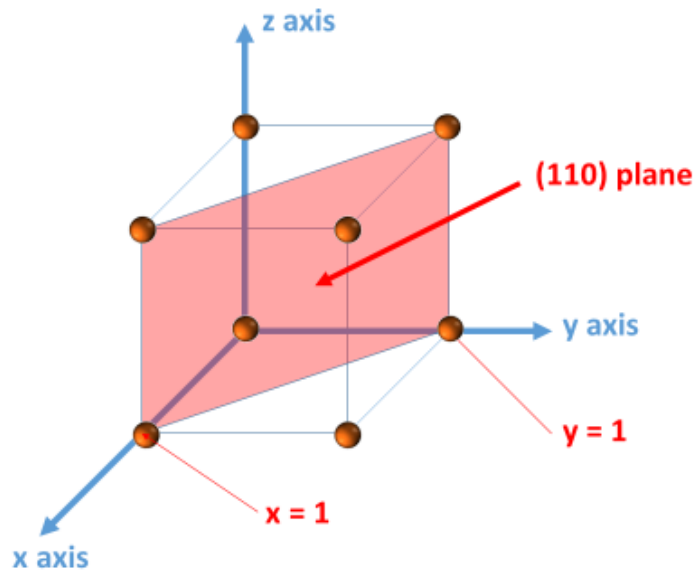
36

Figure 2.3: The x, y, z coordinate system for a simple cubic crystal structure shown by blue vectors in the x, y and z directions. Example atoms (orange spheres) lie at the vertex of the cubic unit cell. The (110) plane is shown in red, intersecting the x axis at x = 1 and y axis at y = 1.

In practice, we can produce a variety of 2-dimensional crystal surfaces from the metal single crystals by 'cleaving' the crystal along a plane which corresponds to a set of one of these particular Miller Indices. The resulting structure of these 2-dimensional surfaces is then dependent on the Miller Indices of this plane and original crystal structure of the metal. The surfaces which will be used in this project are metal single crystals, namely copper. Copper crystals have a face-centred cubic structure (fcc): copper atoms lie at each of the vertices of the crystallographic unit cell and also at the centre of each face on the unit cell. The surface used will be Cu(110) which denotes a cut through the copper crystal corresponding to the (110) plane. This produces a surface with 2-fold symmetry: a close-packed row of copper atoms along the $[\bar{1}10]$ direction and a row in which the copper atoms lie further apart along the $[001]$ direction. **Figure 2.4** shows the orientation of the (110) plane for the fcc copper unit cell and the 2-dimensional surface structure which results from cleaving the crystal along this plane.
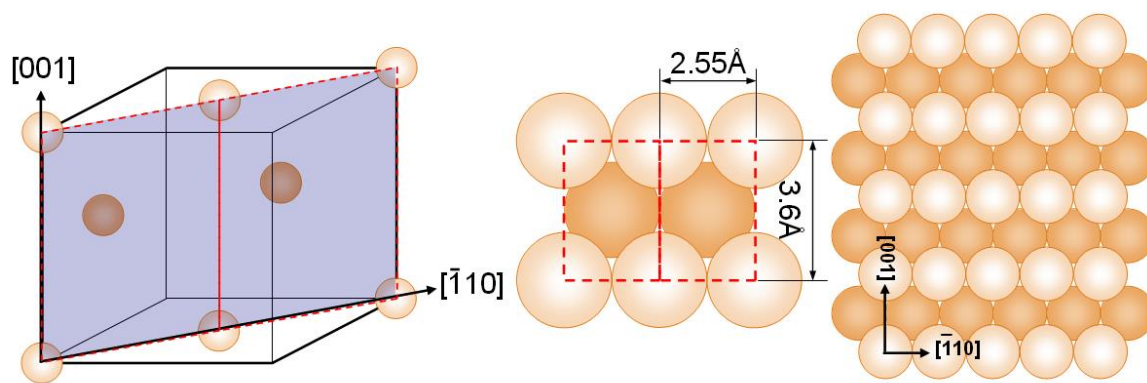
Figure 2.4: The copper fcc unit cell with orange copper atoms shown and (110) plane in blue. The resulting 2-dimensional copper surface structure is shown with distances between copper atoms along the $[\bar{1}10]$ and $[001]$ directions. Adapted from [2.8].

2.1.4   Surface Cleaning and Sample Preparation

In order to investigate the interactions between the metal surface and the adsorbate molecules, we need to have a well-defined, clean surface. Over time, contamination will build up on the surface of the metal crystal and as such it will need to be routinely cleaned before conducting any experiment. The method to do this is by sputtering the metal surface with noble gas ions (Ar^+ in this case). Nobles gases are used because they are inert and do not interact strongly with the metal surface or any contamination present. The charged particles are accelerated towards the surface at high velocities and physically knock contaminant substances off the surface. This process removes contamination but also roughens the ordered exposed surface and leaves remnant noble gas particles in the surface itself. To rectify these issues, the metal crystal needs to be annealed which involves passing a current through a filament underneath the metal crystal to heat it up to high temperatures. This allows the metal atoms on the surface of the crystal to diffuse more readily and eventually reorder back to the original surface crystallography and also desorbing any embedded noble gas atoms left behind after the sputtering process. **Figure 2.5** shows schematics of the sputtering and annealing steps and the final clean surface crystal structure. These sputtering and annealing steps are usually

performed numerous times (sputtering and then subsequent annealing) until the surface is sufficiently clean, ready to conduct experiments. The cleanliness of the surface can be checked using STM.
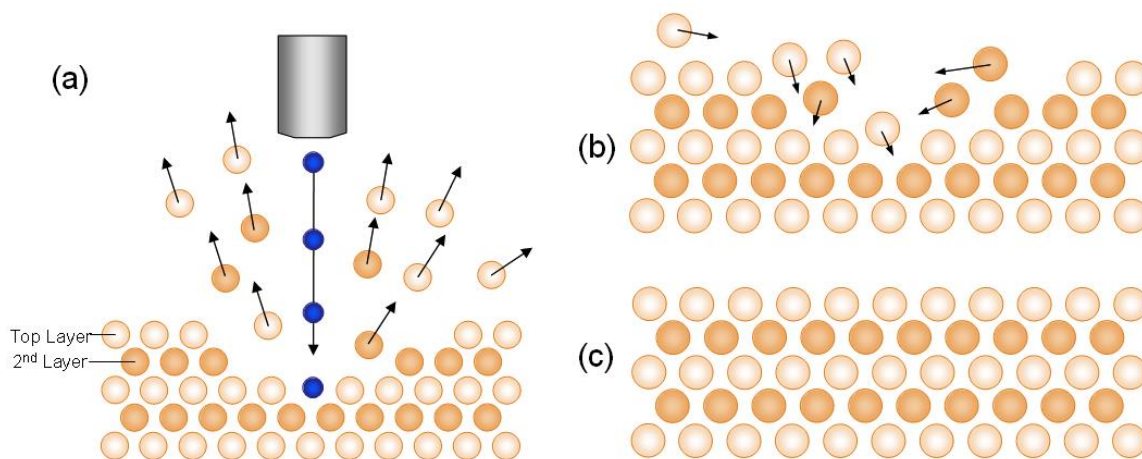

Figure 2.5: a) Sputtering with Ar$^+$ ions to remove contamination from the surface. b) Annealing causes atoms in the roughened surface to rearrange to form an ordered surface structure as shown in c). Adapted from [2.8].

Once the surface is sufficiently clean and pressures lie within the UHV range, to ensure that the surface remains clean for the duration of the experiment, we can begin to deposit molecules onto the surface and investigate how they react with it. This is accomplished using a Knudsen cell, as shown in **figure 2.6**. The Knudsen cell consists of a glass capillary which is filled with a small quantity of the solid molecular material wrapped with a metal wire to create a heating coil around it. A small current can then be passed through the metal wire to heat up the sample causing molecules to evaporate out of the cell in the direction the cell is facing. The Knudsen cell, also known as a doser, is usually orientated to be facing the crystal surface so that molecules can be deposited directly onto it. The orientation of the doser with respect to the crystal surface is something which must be considered as dosing times may differ depending on the distance between them meaning that dosing conditions may need to be modified in order to produce similar sample coverages for different experimental setups. This is particularly relevant when recreating specific sam-

ple structures which have been previously created at the Surface Science Research at the University of Liverpool once we are at the Diamond Light Source using a different UHV chamber and dosing arrangement.
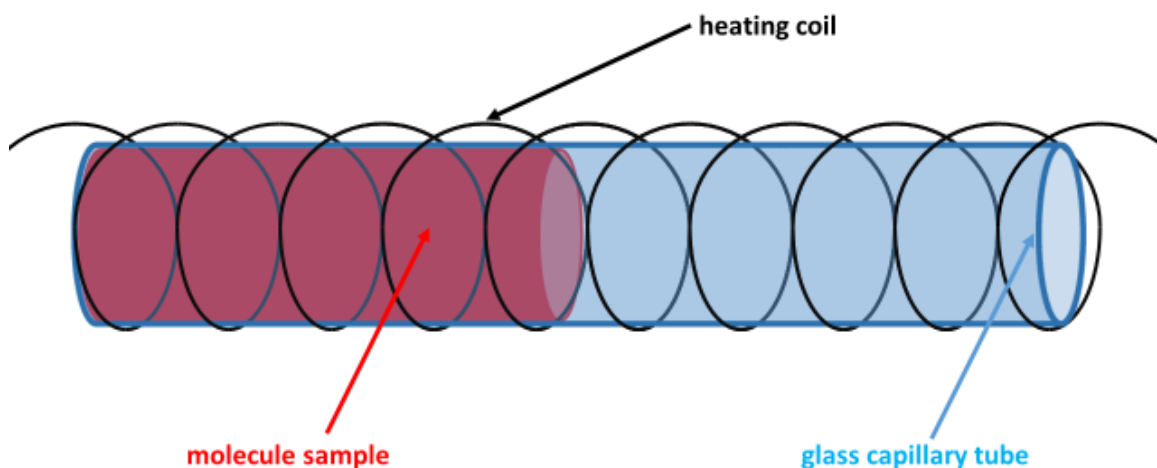

Figure 2.6: Schematic of a Knudsen cell: molecular material (red) inside a glass capillary tube (blue), with a metal heating coil (black) wrapped around it to allow the material to be heated and deposited onto the metal surface.

Before the doser can be used it must be cleared of any contamination which will inevitably be mixed in with the candidate molecules when it is exposed to air as it is being made. This is done using a process called 'degasing'. This involves passing a current through the filament which surrounds the doser to heat up the material to temperatures high enough to allow molecules to begin to evaporate. In our case, we are using large organic porphyrin molecules which evaporate at relatively high temperatures, this means that any contaminant material in the doser is likely to be smaller molecules which evaporate are lower temperatures. We can heat up the doser to a temperature lower than the temperature required to evaporate the porphyrin molecules so that all contaminant material will be evaporated from the doser, and be pumped away, and what we are left with will be just the molecules we are interested in.

Employing these rigorous cleaning steps of the metal surface and the molecular doser and keeping pressures within the UHV region throughout the duration of the experiments, we can be sure that the intended molecules are

interacting with the intended surface structures without significant contamination present and thus can be confident about the results.

2.2   Scanning Tunnelling Microscopy

2.2.1 Historical Background

The principal method used for sample characterisation in this project is Scanning Tunnelling Microscopy for its ability to precisely determine the molecule-surface structures prior to any magnetic investigation. The Scanning Tunnelling Microscope (STM) was developed by Gerd Binnig and Heinrich Rohrer in 1982 [2.9] and exploited the use of quantum mechanical tunnelling of electrons through vacuum [2.10] to enable unprecedented image resolution at the atomic scale. Their continued work on STM and its applications [2.11-2.15] earned them the Nobel Prize in 1986, acknowledging the significant impact that the STM instrument made upon the understanding and investigation of interactions at the nanoscale even within a few years of its conception. Their work built upon previous iterations of other Scanning Probe Microscopies (SPM) particularly an instrument known as the Topografiner.

The Topografiner was developed by Russel Young *et al* in 1972 [2.16] as a non-contact Scanning Probe Microscopy. It consisted of a metal tip lying close to a sample running under field emission [2.17] such that the current between the tip and sample could be used as a feedback mechanism to maintain a constant vertical tip-sample separation during scanning. The Topografiner measured a small tunnelling current which was produced by scattered electrons from the surface based on the Fowler-Nordheim equation. The Fowler-Nordheim defines the process by which the current is measured based upon the escape probability of an electron tunnelling out of the sample. This current could be amplified by an electron multiplier to produce a measurable current which could be used to produce a line by line representation of the

sample structure and was able to produce the first ever scanning probe image. Unfortunately, image resolution was poor partly due to the instrument being fixed to the chamber making it difficult to isolate it from vibrations which would contribute noise to the measured images and also due to the small tunnelling current which occurred from the scattered electrons. Nonetheless, the Topografiner was a triumph for a number of reasons: it was a non-contact method and so did not damage the sample which was being scanned (or the tip itself!) and the imaging method used electrons rather than light meaning that lenses and complicated geometrical setups were not required. Young proposed that the resolution could be improved dramatically by making use of quantum mechanical tunnelling from the tip to sample rather than from escape probability of electrons tunnelling out of the sample as in the Fowler-Nordheim regime, this main adaptation along with improved vibration isolation lead to the creation of the STM. The STM operates using a tip and sample as with the Topografiner but measures the tunnelling current directly caused by electrons tunnelling between the sample and the tip.

2.2.2 Operation

Modern STMs are capable of resolving structures at the atomic length scale (10^{-10} m) and as such are able to directly image atoms and molecules on surfaces [2.18, 2.19]. This makes the STM an invaluable tool for understanding interactions between molecules and surfaces as their orientations with respect to each other can be determined very accurately. The high resolution of the STM is a consequence of how the measured tunnelling current is dependent on the separation between the tip and the sample. The tunnelling probability of an electron decays exponentially with distance between the tip and sample such that small changes in this distance lead to large changes in the measured tunnelling currents. This enables the STM to be extremely sensitive to local changes in sample height such as when scanning over a molecule on the surface. The STM also doesn't require a light source or an electron source as electrons simply tunnel from the tip itself.

A typical STM set up utilises a tungsten tip brought into close proximity with a sample. A voltage bias can then be applied across the sample and tip to allow electrons to tunnel across the gap between them. Tungsten tips are made from tungsten wires which are chemically etched to produce ultra-sharp tips (in the ideal case the tip will have a single atom at its tip where electrons tunnel into thus improving the resolution of the device). The sample itself must be conducting as electrons need to be able to move through the material in order to eventually tunnel across the tip-sample gap; an insulating sample would restrict movement of electrons and as such make it impossible for electrons to produce a measurable tunnelling current. The height of the tip with respect to the sample is controlled using a piezoelectric motor which changes in size along the z-direction in response to an applied electric field. This means that the height of the tip can be manipulated electronically which allows it to approach the sample until a tunnelling current can be measured. Once a tunneling current is measurable, a feedback system prevents the tip from extending any further preventing it from crashing into the sample and potentially damaging the tip. **Figure 2.7** shows the tip and sample set up along with the core electronic components which allow the STM to produce an image.
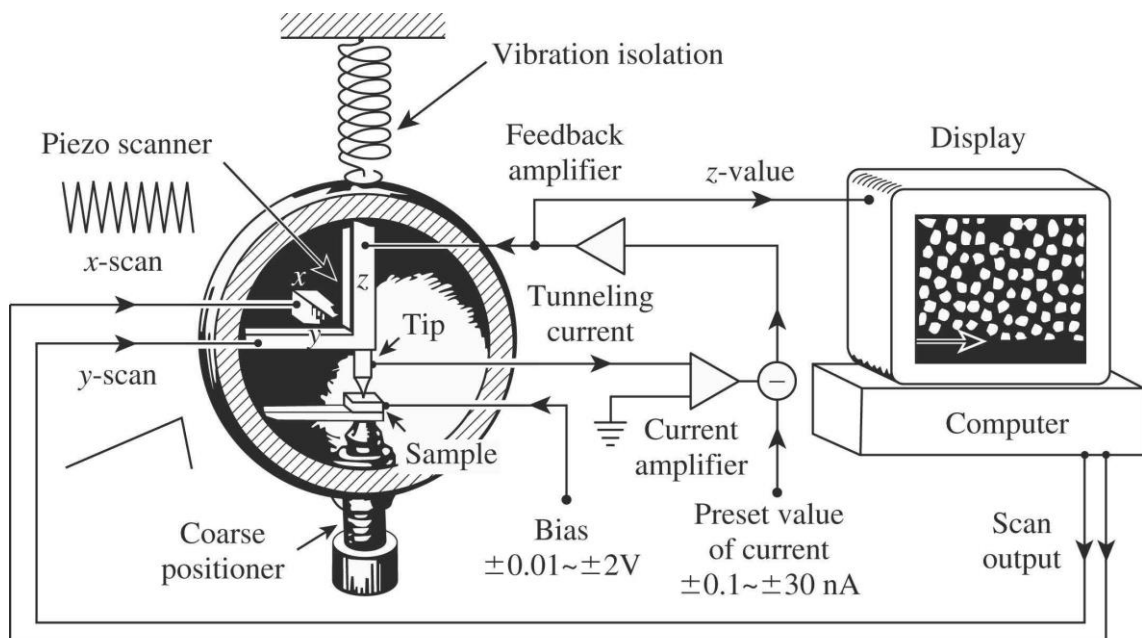

Figure 2.7: A typical set up of an STM within a UHV chamber. The figure shows the tip controlled by piezo scanner in the z direction for tip-sample separation and xy directions for lateral position. The arrangement of the electronic components of the STM are also shown which result in an image on screen. Image adapted from [2.20].

Once the tip and sample are sufficiently close to each other to allow for the quantum mechanical tunnelling of electrons across the gap, a bias voltage is applied across the tip and sample. Using a positive bias voltage across the tip and sample causes electrons to tunnel from filled quantum states in the tip to vacant states within the sample. Conversely, applying a negative voltage causes electrons to tunnel from filled states in the sample to vacant states in the tip. This allows STM to probe the nature of vacant or occupied states within the samples by applying a positive or negative voltage respectively.

Once a tunnelling current can be measured, additional piezoelectric motors manipulate the tip position with respect to the sample in the xy directions. This lateral manipulation allows the tip to scan across the sample to build up an image in a line by line fashion. The end result is a 2-dimensional map of the local density of states of the sample. **Figure 2.8** shows a schematic of how the STM performs a single line scan across an example sample.
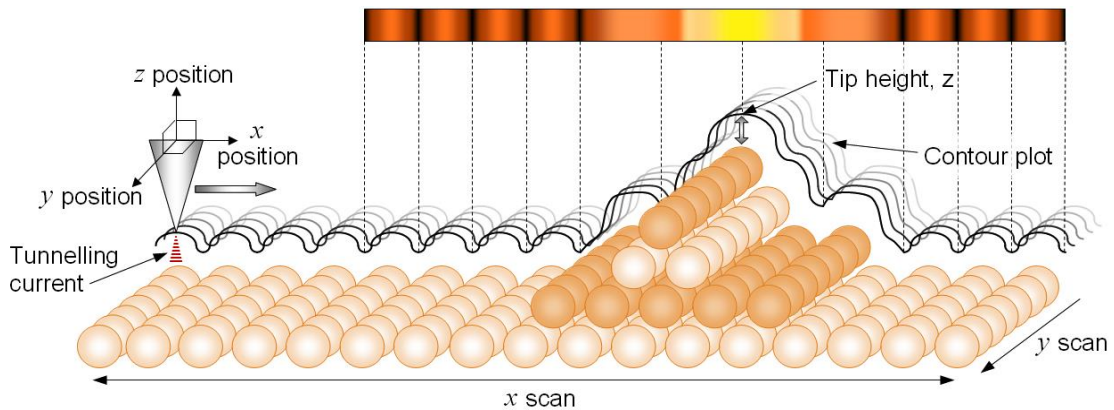
Figure 2.8: Schematic of an STM scanning a single line across a sample. The grey tip maintains a fixed position in y whilst scanning across the x direction. The position of the tip with respect to the sample, z direction, changes as it travels across the sample. The resulting image for the line is shown: atoms on the surface appear orange whilst atoms within the larger structure appear as bright yellow. Adapted from [2.8].

There are 2 main methods of measurement using an STM: constant height mode and constant current mode. Scanning in constant height mode

fixes the tip at a set vertical position in the z direction with respect to the sample. The subsequent tunnelling current is then measured as the tip scans the xy plane of the sample. The method is useful as it allows images to be generated very quickly as the height of the tip does not need to be changed during the production of the image. However, this method is only suitable for surfaces which are relatively flat and uniform throughout. This is because the tip maintains a constant height and can potentially crash into large adsorbates or defects on the surface.

In constant current mode, a feedback loop is setup so that the STM maintains a constant tunnelling current between the tip and the sample by modifying its position in the z direction. The tip scans the xy plane as before but in this case of the tip approaches an atom or molecule on the surface the tunnelling current will change and the feedback system will change the position of the tip in the z direction accordingly. Recording the position of the tip during the scans builds a 2-dimensional image which represents the topography of the sample. In this project, constant current mode will be used almost exclusively as the molecules and structures are large and thus require the STM tip to move in the z direction to avoid it crashing into the sample.

2.2.3 Tunnelling Theory

Understanding the process of quantum mechanical tunnelling can by aided by using the 1-dimensional quantum model. Tunnelling is the process by which electrons with a particular energy E are able to travel between the STM tip and the metal surface across a vacuum. The vacuum can be thought of as a potential barrier U which electrons need to be able to overcome to effectively travel from the STM tip to the metal surface (or vice versa). The following derivation will help to illustrate how electrons are able to penetrate this potential barrier even if their energy E is less than that of the potential barrier U. The derivation can be simplified by only considering 1-dimension

which, in this case, will be defined as the z direction representing the axis along the STM tip and perpendicular to the metal surface.

In the classical regime, the total energy of a classical free electron E travelling within a classical potential U in 1-dimension (in this case the defined z direction) can be defined by:

$$E = \frac{p_z{}^2}{2m_e} + U(z)$$

(2.7)

Where p_z is the momentum of the electron in the z direction (measured in kg m s^{-1}), m_e is the mass of an electron (9.11 x 10^{-31} kg) and $U(z)$ describes the potential as a function of position in the z direction. The STM tip and metal surface are interacting at the atomic scale and as such quantum mechanical effects take precedence as the classical approach no longer holds. Within the quantum mechanical regime, the total energy of an electron E travelling in the z direction within a potential U can be defined more accurately using the time-independent Schrödinger equation given as follows:

$$E\psi(z) = -\frac{\hbar^2}{2m_e}\frac{d^2}{dz^2}\psi(z) + U(z)\psi(z)$$

(2.8)

Where $\hbar$ is the reduced Planck's constant defined as Planck's constant h (6.63 x 10^{-34} J s) divided by 2π and $\psi(z)$ is the wavefunction of the electron travelling in the z direction. This equation can be solved for the 1-dimensional case giving the following solutions:

$$\psi(z) = \psi_0 e^{-ikz}$$

(2.9)

$$\psi(z) = \psi_0 e^{+ikz}$$

(2.10)

Where *k* is the wave number defined by:

$$k = \frac{\sqrt{2m\big(E - U(z)\big)}}{\hbar}$$

(2.11)

These solutions describe electron wavefunctions for unbound electrons travelling in the positive *z* direction (solution 2.9) and the negative *z* direction (solution 2.10) for an electron with energy *E* which is greater than the potential barrier *U*. These solutions are analogous to observed phenomena in the classical regime for a free electron travelling in the positive or negative *z* directions. Unlike the classical regime, there exists another solution for the time-independent Schrödinger equation for the case when the energy of the electron *E* is less than the potential barrier *U*:

$$\psi(z) = \psi_0 e^{-\kappa z}$$

(2.12)

Where in this instance κ is defined as follows:

$$\kappa = \frac{\sqrt{2m(U(z) - E)}}{\hbar}$$

(2.13)

In the classical regime there is no physical interpretation for the case when the electron energy *E* is less than the potential barrier *U* because, in this case, equation (2.7) would only hold true if the kinetic energy of the electron was negative! Subsequently, a classical particle with energy *E* will have 0 probability of penetrating a potential barrier which has an energy *U* which is greater than *E*. In the quantum mechanical regime this is not the case and equation (2.12) shows the possible solution to the Schrödinger equation for when the energy of the particle *E* is lower than the energy of a potential barrier *U*. This

solution can be attributed to the phenomenon of quantum mechanical tunnelling and represents a finite probability that a quantum mechanical particle with energy E can in fact penetrate a potential barrier of energy U and appear on the other side of it even when E is less than U! A schematic of this situation is shown in **figure 2.9** to illustrate the appearance of the wavefunction of the electron during tunnelling.
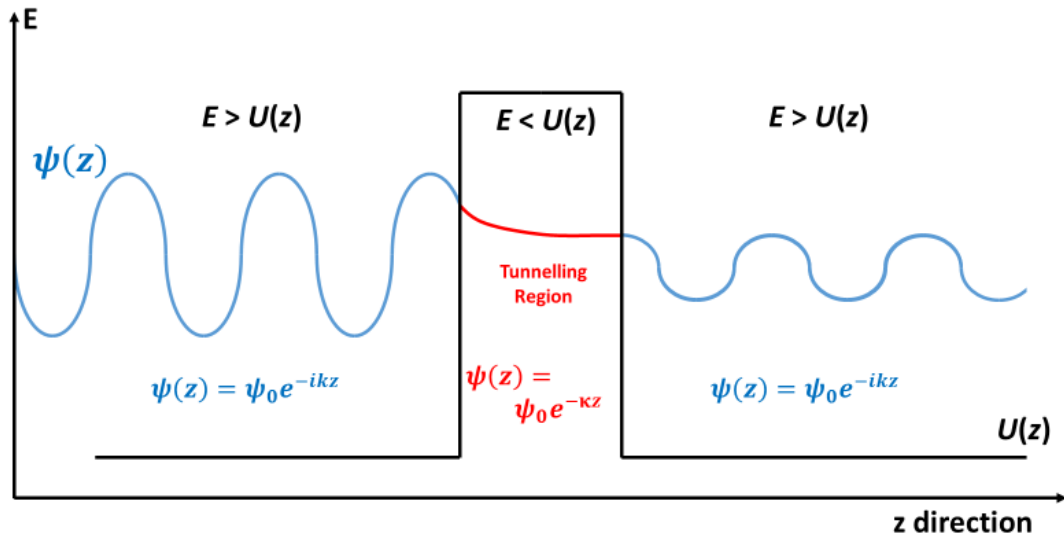

Figure 2.9: Schematic showing the shape of the wavefunction of an electron as it penetrates a barrier with potential U. The blue waves show the sinusoidal-like behaviour corresponding to the solutions of the wavefunction (equation 2.8) when the total electron energy E is greater than the potential U. In this case the wavefunction is travelling in the positive z direction. The red line shows exponentially decaying form of the wavefunction (solution 2.12) when the total electron energy E is less than the potential U.

Figure 2.9 shows an example wavefunction of an electron travelling in the positive z direction through a square potential barrier. The square potential barrier can be thought of as the vacuum region within the STM setup which the electrons are tunnelling across. The red line within the barrier shows how the electron wavefunction looks, in accordance with equation (2.12). The unbound regions either side of the potential barrier show how the blue electron wavefunction looks within the STM tip and the metal surface.

The probability of finding an electron at a particular point in this system is proportional to the square of the amplitude of the wavefunction $|\psi(z)|^2$ such

that the wavefunction at each point in the system gives an indication of how likely an electron is to be found at that particular point. Within the barrier, the wavefunction of the electron takes the form of an exponential decay function such that the amplitude of the wavefunction diminishes across the width of the barrier. If the amplitude of the wavefunction is non-zero when it reaches the end of the barrier then the electron wavefunction returns to sinusoidal form (similar to the shape of the wavefunction before the electron entered the potential barrier) albeit with a significantly reduced amplitude, highlighting that the electron is less likely to be found on the opposite side of the potential barrier.

The probability of finding an electron which has successfully tunnelled through this potential barrier is critically dependent on the width of the potential barrier: equation (2.12) shows the dependence of the wavefunction on z, highlighting how it decays exponentially with increasing values of z such that very small changes in z will result in large changes in the resulting wavefunction. The width of the potential barrier is analogous to the STM tip and metal surface separation *ie* the 'width' of the vacuum between them. This means that the probability of an electron successfully tunnelling across the gap, and yielding a measurable tunnelling current, is very sensitive to small changes in the size of this gap. This is the key characteristic of an STM which enables it to be sensitive enough to resolve features at the atomic length scale.

2.2.4   Density of states

The simple 1-dimensional quantum model of the STM system gives a useful insight into how electrons are able to tunnel across the vacuum gap and give rise to a measurable tunnelling current; however, it does not include any considerations of available energy states within the tip and surface. For an electron to successfully tunnel across the vacuum gap from the tip to the surface there must be vacant energy states or orbitals within the surface for the electron to tunnel into. If the energy states within the surface are fully occupied, then no tunnelling will occur and the tunneling current will be 0. To extend the

model to incorporate these considerations we can call upon density of states theory to give an indication of the nature of the available energy states of the electrons within each part of the STM system. This allows us to show how electrons are able to occupy different states within the STM tip and metal surface and under which conditions they are able to travel between them and thus give rise to a measurable tunneling current.

Figure 2.10 gives a schematic representation of the STM setup and the electron energy states. **Figure 2.10** a) shows the case where no bias voltage has been applied across the tip and surface. Without an applied bias voltage, electrons fully occupy energy states up to the Fermi level such that all electron energy states within the tip and sample are occupied. Since there are no available electron energy states within the surface, electrons from the tip are unable to successfully tunnel across the vacuum gap as they have no vacant electron energy states which they are able to occupy within the surface.

In order to enable electrons to be able to tunnel between the tip and surface we must apply a bias voltage *V*. Once a bias voltage is applied, occupied electron energy states within the tip and surface will shift in energy with respect to each other giving rise to a set of vacant electron energy states which lie below the Fermi level. The resulting energy states are shown in **Figure 2.10** b) where now occupied electron energy states within the surface have shifted down in energy by *eV*, related to the applied bias voltage *V*. This shifting of electron energy states gives rise to vacant electron energy states which electrons from the tip are able to tunnel into. In this case the potential barrier is the work function φ and corresponds to the minimum amount of energy required to remove an electron from the tip into free space. The work function of the tip can be thought of as the vacuum potential barrier.
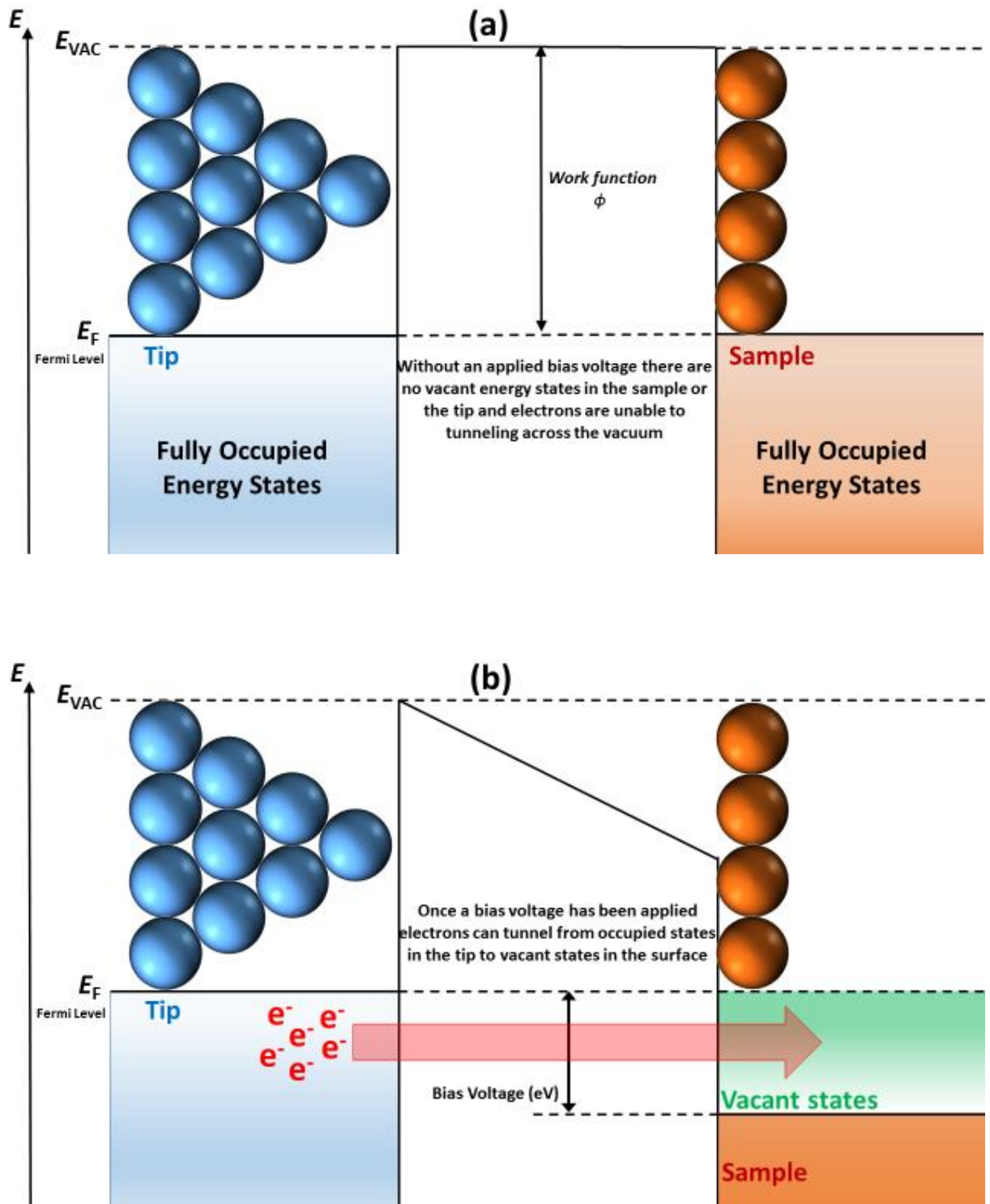
(a)

E_{VAC}

Work function
ϕ

E_F
Fermi Level

Tip

Without an applied bias voltage there are no vacant energy states in the sample or the tip and electrons are unable to tunneling across the vacuum

Sample

Fully Occupied Energy States

Fully Occupied Energy States

(b)

E_{VAC}

E_F
Fermi Level

Tip

Once a bias voltage has been applied electrons can tunnel from occupied states in the tip to vacant states in the surface

e^- e^-
e^- e^- e^-
e^- e^-

Bias Voltage (eV)

Vacant states

Sample

Figure 2.10: Schematic showing the density of states of the STM system. a) When no bias voltage is applied, electron energy states within the surface (orange) and tip (blue) are fully occupied up to the Fermi level E_F and thus no tunnelling occurs across the vacuum gap. b) When a bias voltage V is applied across the tip and surface, the occupied electron energy states within the surface (orange) shift to lower energy values leading to a set of vacant energy states (green) which can now be occupied by electrons tunnelling from filled energy states within the tip (blue).

By considering the local density of states at surface and the probability that an electron can tunnel across the vacuum gap and into these states, it is possible to derive an approximation for the measured tunneling current [2.21]. The local density of states of the surface ρ_s for a particular distance z in 1-dimension at an energy E is related to the electron wavefunction by:

$$\rho_s(z, E) = \lim_{\epsilon \to 0} \frac{1}{\epsilon} \sum_{E_n = E - \epsilon}^{E} |\psi_n(z)|^2 \qquad (2.14)$$

From the solution to the 1-dimensional model derived in the previous section (equation 2.12) we can express the probability P_n of finding an electron at the surface, that has tunnelled across a barrier of width W (equivalent to the tip-surface separation distance) from the point $z = 0$ as:

$$P_n \propto |\psi_n(W)|^2 = \left|\psi_n(0)e^{-kW}\right|^2 = |\psi_n(0)|^2 e^{-2kW} \qquad (2.15)$$

Where k is defined as follows:

$$k = \frac{\sqrt{2m\phi}}{\hbar} \qquad (2.16)$$

Where ϕ is the work function of the metal surface. Since each tunnelling event contributes to the measured tunneling current, it is possible to relate this tunnelling probability expression to the measured tunneling current. This is achieved by considering all of the tunnelling events which can occur from the tip to the electrons energy states of the surface within the region which corresponds to the vacant set of electron energy states. From **Figure 2.10** b) this energy region can be determined as the range between E_F and $E_F - eV$.

Thus by using equation 2.14 and summing all contributions to the total probability of tunnelling across this energy region we obtain an expression for the measured tunnelling current as:

$$I \propto \int \sum_n |\psi_n(0)|^2 \delta(E - E_n)\, dE \qquad (2.17)$$

By using the expression for local density of states of the surface, equation 2.14, gives:

$$I \propto e^{-2k'W} \int_{E_F=eV}^{E_F} \rho_S(0, E_F)\, dE \qquad (2.18)$$

This expression now incorporates the contribution from considering the vacant energy states within the surface which allow quantum mechanical tunnelling to occur. It shows how the tunnelling current depends on applied bias voltage V, local density of states of the surface ρ_s close to the Fermi energy level E_F and the tip-surface separation distance W. It is important to note again that the tunnelling current decays heavily with tip-surface separation distance W and also the work function ϕ as there are terms within the exponent. This dependence is what gives the STM its characteristic high vertical resolution in the z direction.

2.2.5   Experimental Set Up

Investigation and characterisation of the magnetic molecules and metal substrate systems took place primarily at the Surface Science Research Centre (SSRC) at the University of Liverpool. The SSRC is equipped with a range of surface science instrumentation allowing for the full characterisation of molecular systems adsorbed on surfaces. Here, candidate magnetic molecules

were deposited onto the Cu(110) surface under various conditions and the resulting interactions between the molecule and surface were examined. Once potential systems had been fully characterised and understood at the SSRC then they were reproduced at the Diamond Light Source (DLS) during allotted beamtime to explore their magnetic behaviour. The systems were then prepared at the peripheral Surfaces and Interfaces Laboratory (SIL) and then subjected to X-Ray Absorption experiments using synchrotron radiation. It was critical to the success of the project that these systems could be reliably reproduced a number of times so that the systems which had been grown and investigated at the SSRC were identical to those which were used in the X-Ray experiments at the DLS.

At the DLS, the I06 beamline was used to conduct X-Ray Absorption Spectroscopy (XAS) measurements, specifically X-ray Magnetic Circular Dichroism (XMCD) and X-Ray Magnetic Linear Dichroism (XMLD), in order to fully elucidate the magnetic behaviour of the central metal ion within the organic molecular framework on the surface. X-Ray Absorption techniques and the experimental setup of the I06 beamline will be discussed in further detail in **Section 2.3**.

To ensure a high degree of reproducibility of the magnetic systems, Cu(110) single crystal surfaces were purchased from the Surface Preparation Laboratory in the Netherlands and were used both for the initial characterisation experiments at the SSRC and also for the subsequent synchrotron experiments at the DLS. By using the same crystals at both the SSRC and DLC we can be more confident that we can successfully grow identical systems at both facilities. For this project the Cu(110) surface was the only single crystal surface used as the focus of the project was to investigate the extent at which changing the molecular architecture of the organic macrocycles within the molecules affects the magnetic behaviour of the central metal.

The Cu(110) crystals were aligned to a very high degree and polished to achieve a smooth surface. The crystals were cut in a 'top-hat' shape with a 9mm diameter base and a 7mm diameter polished top, leaving a small gap which was used to mount the crystals onto Omicron sample plates, as shown in **Figure 2.11**, by spot welding tantalum strips. This gap enables the crystals to be easily remounted as necessary when transferring the crystals to the different UHV chambers at the SSRC and DLS. Two separate crystals were used during the synchrotron experiments so that one could be deposited with the magnetic molecules and characterised SIL at the DLS, whilst another could be subjected to X-Ray investigation on the actual beamline. This setup allowed for the maximum amount of data acquisition during the limited amount of beamtime available at the synchrotron.
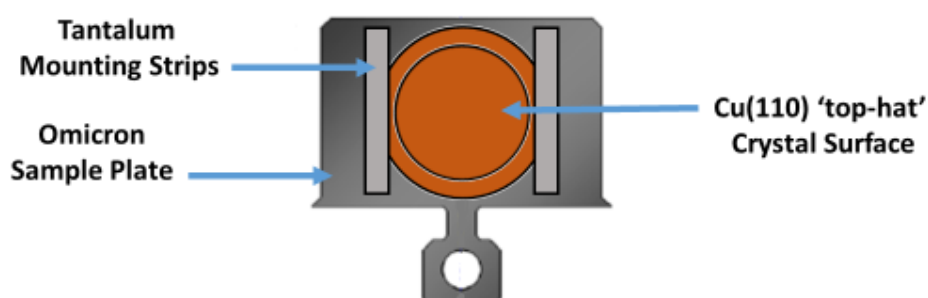

Figure 2.11: Schematic of the Cu(110) crystal surface used for this project. The schematic details the 'top-hat' shaped Cu(110) crystal mounted with thin tantalum strips to a stainless steel Omicron sample plate, for use in the Omicron VT STM system.

The main UHV system used for the characterisation of the magnetic materials was equipped with an Omicron Variable Temperature Scanning Tunnelling Microscope (Omicron VT STM). Whilst capable of conducting STM experiments at low temperatures, the VT STM was used exclusively for room temperature measurements for this particular project. The chamber includes a combined pumping system consisting of a rotary-backed Balzers TPU300 turbomolecular pump, Varian ion pumps and Vacuum Generators titanium sublimation pumps which reliably achieve an operating pressure of 2×10^{-10} mbar, or lower, during STM measurements.
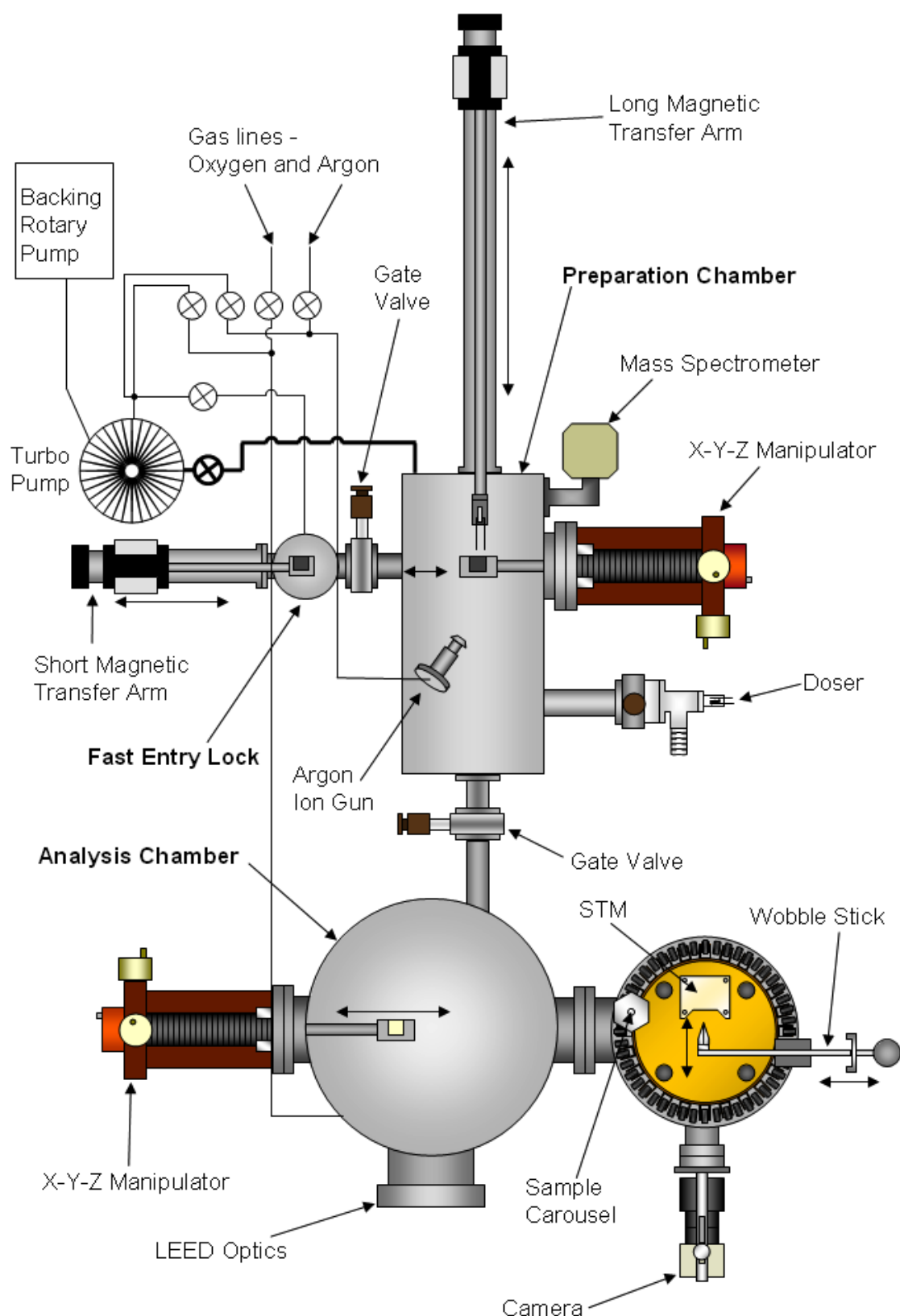
Figure 2.12: Schematic diagram of the UHV chamber at the SSRC at the UoL. The diagram shows the view of the chamber from above with a preparation chamber at the top side of the diagram where cleaning and deposition takes place and an analysis chamber at the bottom side where the STM experiments take place. The STM (Omi-cron VT STM) is shown at the bottom right of the diagram.

Figure 2.12 shows a schematic view of the setup from above of the UHV chamber at the SSRC with components labelled. The UHV chamber consists of two parts: a preparation chamber (shown on the top side of the schematic) and an analysis chamber (shown on the bottom side of the schematic). The preparation chamber is used for all aspects of cleaning the metal surfaces and deposition of the candidate molecules to produce a molecule/metal sample which can then be examined using the STM in the analysis chamber. The two chambers are separated using a gate valve (shown in the centre of the schematic) and movement of the sample between the two chambers is achieved using a magnetic transfer arm. In each of the two chambers is an X-Y-Z manipulator to give precise control of the x, y, and z positions of the sample so it can be reoriented as desired (*eg* facing the ion gun for sputtering or facing the Knudsen cell for molecular deposition). **Figure 2.13** shows a labelled photograph of the UHV chamber and surrounding equipment during operation from a different angle to that shown in the schematic 2.12.
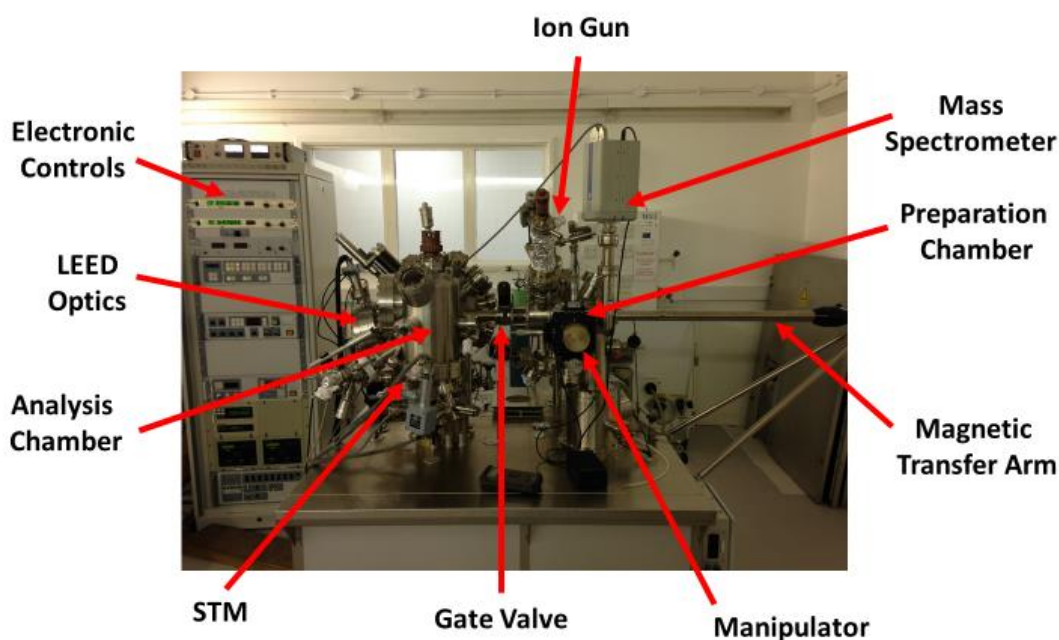

Figure 2.13: Photograph of the UHV chamber at the SSRC at the UoL. Key components are labelled including characterisation apparatus (mass spectrometer, LEED optics, STM) and magnetic transfer arms and manipulators which are used to move the sample around the chamber.

Cu(110) crystals were cleaned using sputtering and annealing cycles until an atomically clean surface was achieved, ready for deposition of molecules. For sputtering, argon gas was fed into the chamber via a gas line in the preparation chamber and used in conjunction with an ion gun to produce the Ar^+ ions to bombard the surface. The sputtering procedures were conducted at a pressure of 2×10^{-5} mbar, 500V acceleration voltage on the ion gun giving a 5μA drain current on the sample for 30 minutes. The sample was then annealed to 600K for 30 minutes to allow the surface to reconstruct. 3 sputtering then annealing cycles was usually sufficient to achieve a suitably clean surfaces. The cleanliness of the surface was checked using STM and subsequent cleaning was undertaken if necessary.

Once surfaces were clean and allowed to cool to room temperature, molecules could then be deposited onto them and the resulting structures investigated using STM. This was done using vapour deposition of molecules onto the Cu(110) surfaces using a Knudsen cell filled with molecular material. The temperature of the vapour deposition could be controlled by changing the current passing through the coil within the Knudsen cell. The resulting molecular organisation and coverage levels was then studied using STM.

The gas lines were also used to inject oxygen gas into the system in order to allow for the STM to be properly calibrated. This can be done by exposing a clean Cu(110) to the oxygen gas which causes a 2x1 O-Cu(110) reconstruction to be formed on the surface [2.22-2.24]. This reconstructed surface is well-known and understood and thus using previously measured distances which have been verified for this reconstruction, the STM can be calibrated to match these distances and allow for any new distance measurements to be made on new systems to be more accurate.

The UHV chamber at the SIL at the DLS was also equipped with an Omicron VT STM and featured a largely similar setup to that used at the

SSRC. This was highly advantageous as it meant that the preparation conditions for the magnetic materials could be replicated to a high degree of accuracy and as such any structure which had been prepared at the SSRC could be reliably reproduced at the DLS ready for investigation on the beamline.

Samples were once again characterised using STM to check that they were identical to those which had been produced back at the SSRC to ensure that the desired structures were being investigated. Once suitable samples had been prepared they were transferred from the SIL lab to the I06 superconducting magnet to conduct the XMCD measurements. This was facilitated by using a portable UHV suitcase which could attach to the SIL to obtain the sample and then transfer it for insertion into the superconducting magnet on the beamline. The UHV suitcase housed a baby chamber to store the prepared sample and an adjacent ion pump to ensure that UHV conditions were maintained throughout the transfer process. This enabled the sample to be transferred from the SIL to the beamline without ever breaking UHV conditions, thus ensuring that the prepared samples do not get contaminated.

Once XAS measurements had been completed, the transfer process was reversed and the sample returned to the SIL. The sample was then transferred back into the STM to verify that the X-rays had not caused any significant damage to the molecules during exposure to ensure the validity of any measurements which were taken on the beamline.

2.3 X-Ray Theory and Methods

2.3.1 Synchrotron Radiation

X-Ray based techniques are well suited to exploring the magnetic and electronic properties of these molecular systems. However; measuring remnant magnetic behaviour of the molecular spintronic systems poses a challenge experimentally as the quantities of magnetic material present are very low; in the case of this project sub-monolayer quantities of molecules were used. Furthermore, within this molecular layer only the metal core ions are of interest to magnetic investigation which further dilutes the quantity of material of actual magnetic interest. Due to this constraint, experiments require the use synchrotron-based X-Ray sources, which are the only sources of X-Rays which can provide high enough photon flux to allow for these experimental techniques to be sensitive enough to detect even small magnetic moments from the small quantities of magnetic material present in the system. **Figure 2.14** shows how advances in synchrotron technology have developed over time to enable these experiments to even become feasible.
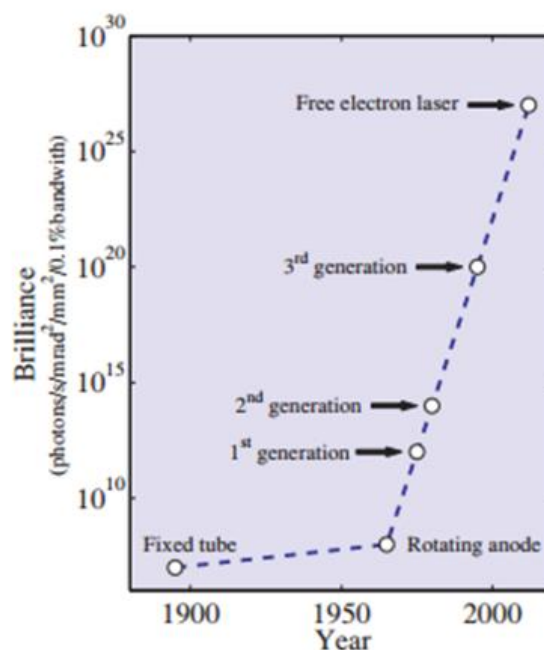

Figure 2.14: The development of synchrotron sources of the last century showing the rapid increase in brilliance (photon flux) which has occurred to allow for this research. Image taken from [2.25].

Synchrotron radiation is produced by accelerating electrons to near relativistic velocities within a particle accelerator [2.26]. Electrons are initially produced using an electron gun which consists of a metal filament which is heated, by passing a current through it, to high enough temperatures that electrons begin to be emitted from the surface. These electrons are then accelerated through a linear accelerator by using surrounding magnets which produce very high magnetic fields. The electrons then enter a booster synchrotron ring (which is situated within the larger main ring of the synchrotron) and continue to be accelerated by external magnets until their velocity is close to that of speed of light. Once the electrons have sufficient velocity (>99% the speed of light) they are then injected into the main storage ring of the synchrotron where they continue to travel around the ring. **Figure 2.15** shows a schematic diagram of a typical 3rd generation synchrotron light source and the layout of the Diamond Light Source (DLS) used in this project.
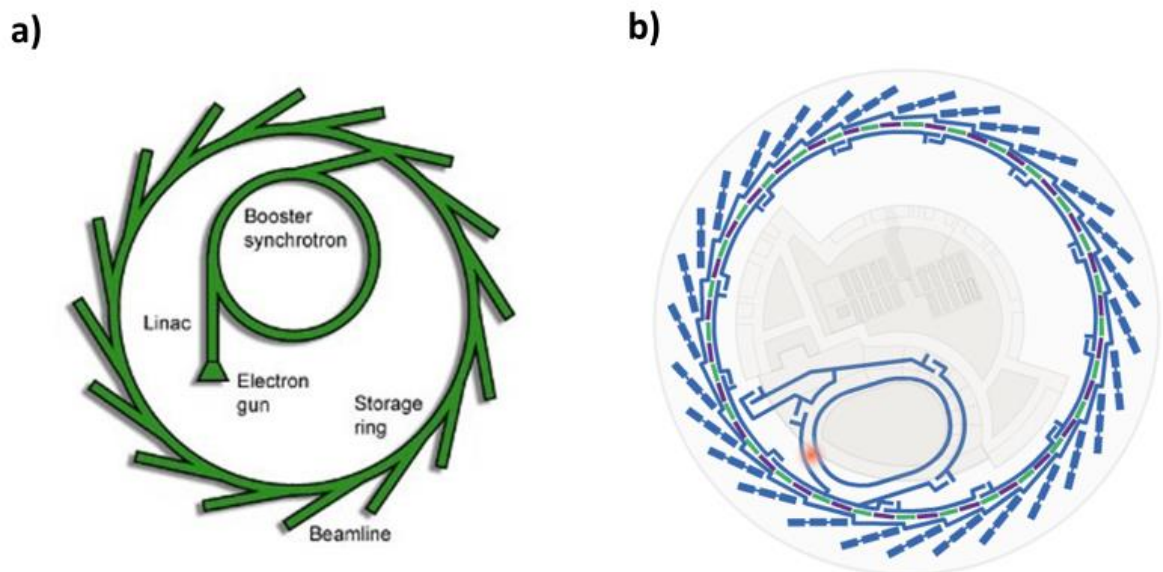

Figure 2.15: Synchrotron Layouts for a) A typical 3rd generation synchrotron and b) the Diamond Light Source. Images taken from [2.27].

Insertion devices, such as bending magnets and undulators, then use high magnetic fields to cause the electrons to generate synchrotron radiation for the experimental end-stations which lie tangentially to the ring called beamlines where the light is focused using a range of optics. Undulators consist of

multiple arrays of magnetic material with alternating magnetic fields which manipulate the path of the electrons as they travel through them. The alternating magnetic fields within the undulator cause synchrotron radiation produced by the electrons to be amplified as a function of n, where n is the number of magnetic units within the undulator. The relative position of the magnetic arrays can also be changed with respect to each other to further influence the path of electrons which can cause the synchrotron radiation to be produced to become polarised in desired ways. This is particularly important for X-Ray magnetic circular dichroism which utilises circularly polarised X-Rays to probe the magnetic behaviour of materials.

2.3.2   X-Ray Magnetic Circular Dichroism

To determine the behaviour of the magnetically active sites in these systems, synchrotron-based X-Ray techniques were employed extensively using the I06 beamline at the DLS specialised for nanoscience experiments. The systems were studied using X-Ray Magnetic Circular Dichroism (XMCD) which is the only probe sensitive enough to determine the surface magnetism of sub-monolayer amounts of material deposited on a metal surface. XMCD is an application of X-Ray Absorption Spectroscopy (XAS) using polarised X-Rays. XAS is a core-level spectroscopy which probes the valence electronic states within atoms by exciting core level electrons within the atom to valence electronic states by an energy equal to the energy of the incident X-Rays. The resulting XAS spectrum gives an indication of the electronic environment of the atom within the material. XAS is an element specific technique as these electronic transitions have fixed energy values for different elements and as such the energy of the incident X-Rays can be tuned using a monochromator on the beamline to produce X-Rays of specific energies which can then be used to probe the desired element within the materials under investigation.

For transition metals, XAS scans are typically made across the L_3 and L_2 absorption edges which correspond to electronic transitions from core $2p$

orbital states to valence $3d$ orbital states; the *3d* states being most intimately involved in the magnetic properties of transition metals. The L_3 absorption edge corresponds to electronic transitions from the occupied *$2p_{3/2}$* states to valent *3d* states and the L_2 absorption edge corresponds to electronic transitions from the occupied *$2p_{1/2}$* states also to valent *3d* states as shown in **figure 2.16a**. The L_3 absorption edge intensity is double that of the L_2 absorption edge as the core *$2p_{3/2}$* states involved in the L_3 transition are doubly occupied (4 electrons) compared to the *$2p_{1/2}$* states involved in the L_2 transition (2 electrons).

XMCD measurements are produced by conducting XAS scans across these L_3 and L_2 edges using right-handed (positive helicity) and left-handed (negative helicity) circularly polarised light to probe these magnetic properties of elements within materials. When the light has become circularly polarised, the photons within the beam carry a unit of angular momentum which is either parallel or antiparallel to the direction of the beam depending on whether the light is positive circularly polarised or negative circularly polarised respectively. Angular momentum must be conserved throughout the absorption process which imposes new restrictions on the absorption mechanism thus making the overall process spin-dependent. This absorption mechanism can be explained using a two-step process [2.30]. Firstly, the spin-polarised photons in the circularly polarised light beam are absorbed by electrons in the core *2p* states. The angular momentum from the photon must be imparted onto the excited electron to conserve the overall angular momentum of the interaction. This produces excited spin-polarised electrons. The *2p* states can then be treated as a source of spin-polarised electrons. These spin-polarised electrons can then be absorbed by the valent *3d* states. If these valent *3d* states have unequal populations of valent spin-up and spin-down states then they act as a

detector of spin as spin-up electrons will be more preferentially absorbed into vacant spin-up *3d* states.

Magnetic atoms within materials show a preferential absorption for one handedness of circularly polarised light versus the other based upon the splitting of these valence *3d* spin states. When the incident polarised light imparts its angular momentum onto excited electrons, different proportions of spin-up and spin-down electrons are produced based upon whether the incident light has positive helicity or negative helicity as shown in **figure 2.16b**. When the *2p* states absorb light with positive helicity, 63.5% spin-up electrons are produced at the L_3 edge and 25% spin-up electrons at the L_2 edge. When the *2p* states absorb light with negative helicity, 37.5% spin-up electrons are produced at the L_3 edge and 75% spin-up electrons at the L_2 edge. The relative populations of spin-polarised electrons produced upon the absorption of a spin-polarised photon is different depending on whether the light has positive or negative helicity yet the relative population of the valent spin-split *3d* states remains the same. This means that taking the difference between a positive helicity absorption spectrum and a negative helicity absorption spectrum produces a non-zero signal for magnetic materials with a net spin [2.28]; this is the XMCD spectrum and is proportional to the total magnetic moment of that particular element (see **Figure 2.16**).

The resulting XMCD peaks at the L_2 and L_3 absorption edges relate to the spin-orbit coupling terms of the *2p* states in the metal: $l + s$ for the L_3 edge and $l - s$ for the L_2 edge. This usually results in a dichroic signal with positive and negative features for the vast majority magnetic materials. XMCD has been utilised extensively in recent studies showing that it is indeed a suitable technique to study these molecular magnet systems and has become a key factor in enabling research into molecular spintronics [2.30].
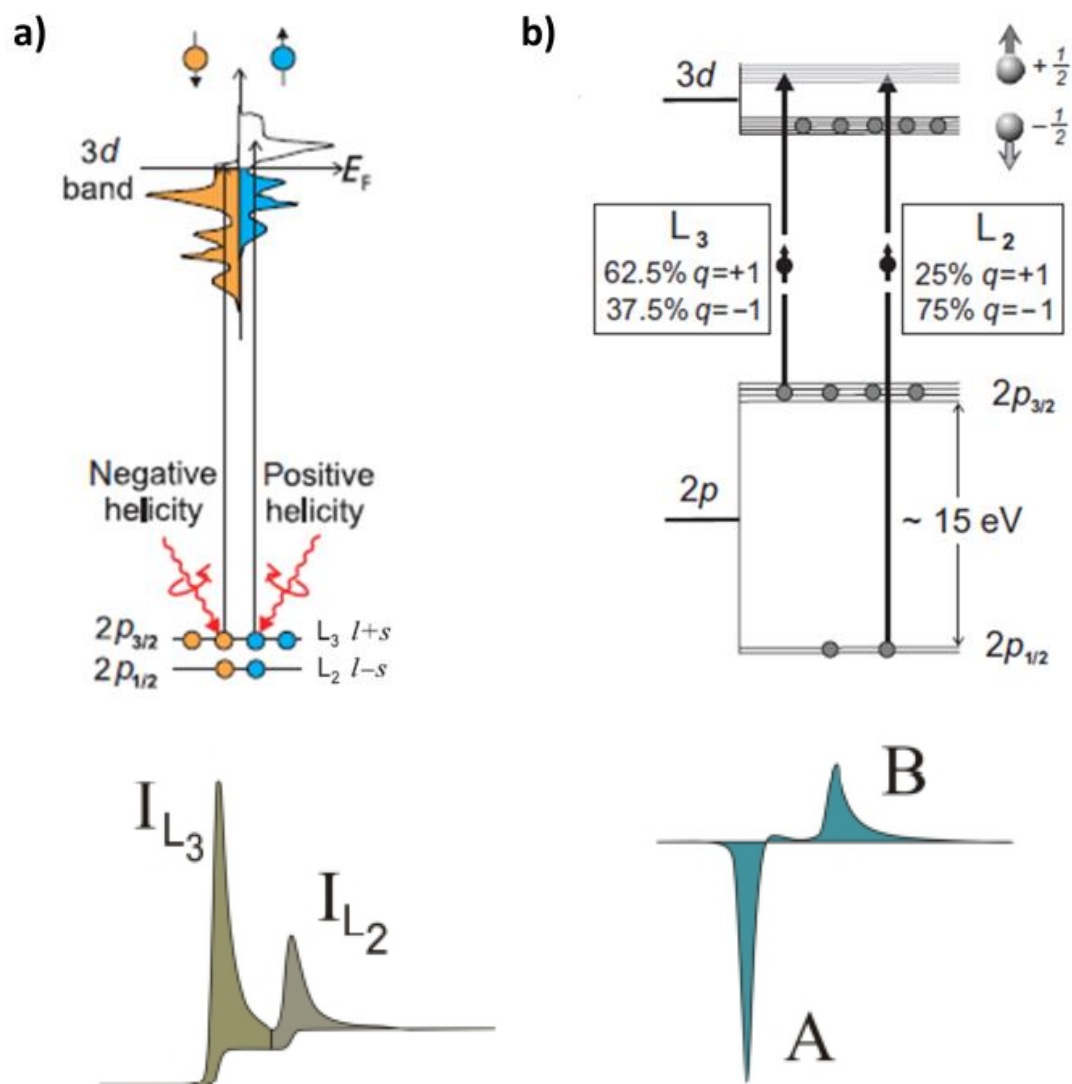
Figure 2.16: a) Energy level diagram for a generic X-Ray absorption process for a 3d metal showing the electronic transitions from the core *2p* states to valent *3d* states. A typical associated XAS spectrum shown below highlighting the relative intensities of the L_2 and L_3 peaks. **b)** Energy level diagram showing the X-Ray absorption process and relative spin-polarised electrons populations produced for positive circularly polarised light (q=+1) and negative circularly polarised light (q=-1) for a typical transition metal. Taking the difference between the positive circular light absorption spectrum and the negative circular light absorption spectrum produces a typical XMCD signal shown below with characteristic negative (A) and positive (B) features. Diagrams adapted from [2.30].

One of the main advantages of XMCD over other techniques is its element-specificity: the energy of the incident X-Rays can be tuned to the absorption edges of the magnetically active component of materials, for example Co

in this project, to exclusively determine the magnetic properties of that specific element. This is a huge advantage over other experimental techniques which are only capable of measuring the overall magnetisation of a material as XMCD can determine precisely the origin of the magnetic behaviour within a material. XMCD is also a very flexible technique as specialist XMCD beamlines, such as the I06 beamline at the DLS, are usually equipped to conduct a range of various measurements to complement these magnetic experiments. These include the capabilities to conduct angular dependent XAS and XMCD; temperature dependent XMCD and, by varying the strength of an external magnetic field, magnetisation measurements. By employing this set of measurements, it is possible to gain great insight into all aspects of the magnetic behaviour of a system.

XMCD is a particularly powerful tool in that it is the only experimental technique which can deconvolute the spin and orbital contributions to the total magnetic moment of the element in question unlike other experimental techniques which are only capable of measuring a total effective magnetic moment. This enables the explicit determination of both the spin magnetic moment and the orbital magnetic moment of the species via application of theoretical XMCD sum rules devised by Thole *et al.* [2.31-2.34]. These sum rules were later verified experimentally by Chen *et al.* for bulk Co and Fe [2.35] and have since been used extensively in all aspects of research using XMCD. This aspect of XMCD is particularly useful for low-dimensional systems such as molecular spintronics on surfaces as being able to calculate individual spin and orbital moments of an element allows for a deeper understanding into other magnetic phenomena such as magnetic anisotropy which is largely dominated by the size of the orbital magnetic moment. In bulk ferromagnetic materials such as Co, Fe and Ni, the orbital magnetic moment is quenched and much smaller than the spin magnetic moment of the ions and consequently there is no magnetic anisotropy. However, in molecular materials this is not the case and as such the orbital moment has a more significant contribution to the overall magnetic behaviour of the material often leading to magnetic anisotropy [2.29].

The specific sum rules for the calculation of the orbital moment m_{orb} and spin moment m_{spin} are as follows:-

$$m_{orb} = -\frac{4 \int_{L_3+L_2} (\mu_+ - \mu_-)dE}{3 \int_{L_3+L_2} (\mu_+ + \mu_-)dE} (10 - n_{3d})$$

(2.19)

$$m_{spin} = -\frac{6 \int_{L_3} (\mu_+ - \mu_-)dE - 4 \int_{L_3+L_2} (\mu_+ - \mu_-)dE}{\int_{L_3+L_2} (\mu_+ + \mu_-)dE}$$

$$* (10 - n_{3d}) \left(1 + \frac{7\langle T_z \rangle}{2\langle S_z \rangle} \right)^{-1}$$

(2.20)

Where μ_+ is the XAS measured with positive circularly polarised light, μ_- is the XAS measured with negative circularly polarised light and n_{3d} is the number of d electrons of the metal. The T_z/ S_z term is related to an anisotropy in the spin moment contribution due to distorted orbitals such as when metals are bonded to ligands as in organometallics. This term is negligible in bulk magnetic metals but must be considered for low-dimensional systems where it can have a larger contribution.

2.3.3 X-Ray Linear Dichroism

Along with circularly polarised light, the I06 beamline is capable of producing linearly polarised light at any azimuthal angle with respect to the sam-

ple. By taking the difference between two XAS spectra measured with horizontally linearly polarised light and vertically linearly polarised light, it is possible to determine anisotropies in the electronic charge distributions around a particular atom. This technique is known as X-Ray Linear Dichroism. These measurements can be used to expose the nature of valence molecular orbitals around particular ions within the molecules.

XLD is especially useful for probing the electronic environment around specific atoms within molecules [2.36]. These measurements can also be conducted under the presence of an external magnetic field to determine if the electronic environment of a specific magnetic element changes when a magnetic field is applied. In the case for porphyrins, XLD can be used to elucidate the bonding structure between the Co metal centre, the surrounding N atoms and the Cu substrate.

The XAS and the XLD spectra can also be fitted using multiplet calculations to produce a suggested ligand field environment around the central Co ion which can be used to help understand the magnetic behaviour of the Co. Multiplet calculations attempt to simulate the spectral line shapes of the L_3 and L_2 edges and attribute them to specific electronic transitions in the metal. These can then be compared with experimental XAS spectral line shapes in order to elucidate which of the electronic states in the metal are contributing to the measured spectra.

2.3.4 X-Ray Data Acquisition

During the beamline experiments, once a suitable sample has been prepared it can be transferred, using a UHV suitcase, from the peripheral lab at the DLS to the superconducting magnet on the I06 beamline where the XMCD measurements can begin, as described in **Section 2.2.5**.

Once inside the magnet the incident photon beam needs to be positioned so that it illuminates the centre of the sample. This is achieved by performing XAS scans at the Cu L_3 absorption edge (at 931eV) to locate the position of the sample with respect to the beam. The vertical position of the beam with respect to the sample can then be changed by using a motor to manipulate the vertical position of the sample. The horizontal position of the beam with respect to the sample can be changed by using a mirror to deflect the beam along the horizontal axis so that it lies in the centre of the sample.

Once the beam was centred on the sample, it was subject to an external magnetic field of the range +6T to -6T using the superconducting magnet. The sample was then cooled to a target temperature of 1.5K using liquid helium. The low-temperature used removes thermal magnetic fluctuations of the electron spins and encourages them to align thus maximising any measurable magnetic behaviour. XMCD measurements were then conducted using XAS scans across the Co L_3 and L_2 edges corresponding to the energy range of $765 - 815eV$. This was achieved by changing the energy of the incident photon beam using a monochromator on the beamline which can sweep through this energy range and measure the resulting drain current on the sample. The measured drain current on the sample was normalised against the drain current of a mirror on the beamline caused by the incident photon flux upon it. This step normalises the XAS signal against the photon flux to give a normalised XAS signal which is independent of the magnitude of incident photon flux and accounts for any variations in it during the experiment. The normalised drain current on the sample was then plotted as a function of incident photon energy to produce an XAS curve with characteristic peaks at the Co L_3 and L_2 edges.

To produce the XMCD spectra, XAS measurements were taken using circularly polarised light which is right-handed (positive helicity) and left-handed (negative helicity). An XMCD spectrum is then the result of the difference between a positive helicity XAS spectrum and a negative helicity XAS

spectrum as detailed in **Section 2.3.2**. The photon beam was circularly polarised using an undulator on the beamline which can manipulate the path of synchrotron electrons to produce the desired photon polarisation. Typically, the polarisation of the photon beam was switched from positive helicity to negative helicity between each individual XAS scan during data acquisition. The reason for this was so that the background contributions to the XAS spectrum were as similar as possible between adjacent positive and negative helicity scans. This was important because when the background contributions to each positive helicity and negative helicity XAS scan are similar, it ensures that the overall background contribution to the XMCD spectrum, when taking the difference between them, cancels out giving a better XMCD measurement.

These 'pairs' of positive helicity and negative helicity XAS scans were then performed in a batch of 10-20 depending on the quality of the data, for each of the desired external magnetic field directions and sample orientations with respect to the incident photon beam. Each pair of XAS scans and their resulting XMCD would be manually inspected to ensure that there was good alignment between the positive and negative helicity XAS scans and that the resulting overall background contribution to the XMCD was small. The L_3 and L_2 peaks from each pair of XAS scans and subsequent XMCD signal were also inspected to confirm that the origin of the L_3 and L_2 XMCD peaks were a result of differences in absorption intensity at the L_3 and L_2 peaks between positive and negative helicity and not a result of any experimental artefacts arising from poor alignment between the scans. These inspected XAS pairs would produce a set of reliable XMCD measurements which could then be compared and averaged as necessary to produce a final single XMCD curve which is shown in the following results chapters.

Magnetisation dependent measurements were performed in a similar fashion to the bulk XMCD measurements using different external magnetic fields strengths. At each desired external magnetic field strength, a positive helicity XAS scan and a negative helicity XAS scan was taken producing a

single XMCD spectrum for that particular magnetic field strength. The external magnetic field strength was then changed in steps of 0.5T and the process repeated from +6T to -6T and then back from -6T to +6T for a complete magnetic loop which would reveal whether any magnetic hysteresis effects are present. The resulting magnetisation curves would then be plotted as the peak XMCD L_3 value as a function of external magnetic field strength.

2.4 Surface Science Theory References

[2.1]   P. Atkins & J. de Paula. *Atkins' Physical Chemistry. 10th Edition.* Oxford University Press p. 792-793 (2014).

[2.2]   K. Kolasinski. *Surface Science: Foundations of Catalysis and Nanoscience. Third Edition.* Wiley. p. 203. (2012).

[2.3]   N. Marquardt. *Introduction to the Principles of Vacuum Physics.* (1999).

[2.4]   L. J. Brillson. *Surfaces and Interfaces of Electronic Materials.* Wiley. p 70. (2010).

[2.5]   J. O'Hanlon. *A User's Guide to Vacuum Technology. John Wiley & Sons.* p 385. (2005).

[2.6]   K. Marton. *Vacuum Physics and Technology. Academic Press.* p 247. (1980).

[2.7]   P. Redhead. *New Hot-Filament Ionization Gauge with Low Residual Current.* J. Vac. Sci. Technol. 3, 173 (1966).

[2.8]   P. J. Donovan. *Adsorption and Self-assembly of Cobalt(II)-Tetraphenyl porphyrin on Cu(110).* PhD thesis, University of Liverpool (2009).

[2.9]   G. Binnig; H. Rohrer. *Surface Studies by Scanning Tunneling Micros- copy.* Physical Review Letters. 49, 57-61 (1982).

[2.10] G. Binnig; H. Rohrer. *Tunneling Through a Controllable Vacuum Gap.* Applied Physics Letters. 40, 178-180. (1982).

[2.11] G. Binnig; H. Rohrer. *Scanning Tunneling Microscopy.* Helvetica Phys- ica Acta. 55, 726-735. (1982).

[2.12] G. Binnig; H. Rohrer. *Scanning Tunneling Microscopy.* Surface Sci- ence. 126, 236-244. (1983).

[2.13] G. Binnig; H. Rohrer. *(111) Facets as the Origin of Reconstructed Au(110) Surfaces.* Surface Science Letters. 131, 379-384. (1983).

[2.14] G. Binnig; H. Rohrer. *Scanning Tunneling Microscopy.* Physica B. 127, 37-45. (1984).

[2.15] G. Binnig; H. Rohrer. *The Scanning Tunneling Microscope.* Scientific American. 253, 50-56. (1985).

[2.16] R. Young. *The Topografiner: An Instrument for Measuring Surface Mi- crotopography.* Rev. Sci. Instrum. 43, 999 (1972)

[2.17] R. Young. *Field Emission Ultramicrometer.* Rev. Sci. Instrum. 37. 275 (1966)

[2.18] C. Bai. *Scanning Tunneling Microscopy and its applications.* Springer. p 1-7. (2000)

[2.19] G. Binnig; H. Rohrer. *Scanning Tunneling Microscopy.* Ibm Journal of Research and Development. 44, 279-293. (2000)

[2.20] C. J. Chen. *Introduction to Scanning Tunneling Microscopy.* 2nd Edition. Oxford University Press. p 1. (2007)

[2.21] J. Tersoff; D. R. Hamann. *Theory and Application for the Scanning Tun- neling Microscope.* Physical Review Letters. 50, 1998-2001. (1983).

[2.22] F. Jensen. *Surface Reconstruction of Cu(110) induced by oxygen chemisorption.* Physical Review B. 41, 10233-10236. (1990).

[2.23] D. J. Coulman. *Novel Mechanism for the Formation of Chemisorption Phases: The (2x1)O-Cu(110) "Added Row" Reconstruction.* Physical Review Letters. 64, 1761-1764. (1990).

[2.24] H. Durr. *Added-Row Growth of the (2x1)O-Cu(110) Reconstruction.* Physical Review B. 43, 1802-1804. (1991).

[2.25] Als-Nielsen, J. *Elements of Modern X-ray Physics 2nd Edition.* Wiley. (2011).

[2.26] Elder, F *et al. Radiation from Electrons in a Synchrotron.* Phys. Rev. 71, 829 (1947).

[2.27] The Diamond Light Source Website http://www.diamond.ac.uk/Home/About/How-Diamond-Works.html

[2.28] Schutz, G *et al. Absorption of circularly polarized X rays in Iron.* Phys. Rev. Let. 58, 737. (1987)

[2.29] Stöhr, J. *Exploring the microscopic origin of magnetic anisotropies with X-ray magnetic circular dichroism (XMCD) spectroscopy.* J. Magnetism and Magnetic Materials, 200, 470-497 (1999).

[2.30] Stöhr, J & Siegmann, H. *Magnetism: From Fundametnals to Nanoscale Dynamics.* Springer Series in Solid-State Sciences. (2006).

[2.31] Thole, B. *et. al. X-Ray Circular Dichroism as a Probe of Orbital Magnetisation.* Phys. Rev. Lett. 68, 12 (1992).

[2.32] Carra, P. *et. al. X-Ray Circlar Dichroism and Local Magnetic Fields.* Phys. Rev. Lett. 70,5 (1993).

[2.33] Thole, B & O'Brien, W. *Orbital and spin sum rules in x-ray magnetic circular dichroism.* Phys. Rev. B. 50, 17 (1994).

[2.34] W. L. O'Brien & B. P. Tonner. *Orbital and Spin Sum Rules in X-Ray Magnetic Circular Dichroism.* Phys. Rev. B. 50, 12672. (1994).

[2.35] Chen, C. *et. al. Experimental Confirmation of the X-Ray Magnetic Circular Dichroism Sum Rules for Iron and Cobalt.* Phys. Rev. Lett. 75, 1 (1995).

[2.36] van der Laan, G & Thole, B. *Strong magnetic X-ray dichroism in 2p absorption spectra of 3d transition-metal ions.* Phys. Rev. B. 43, 13401. (1991).

3 Cobalt Tetraphenyl Porphyrin on Cu(110)

3.1 Phase 1 CoTPP/Cu(110) Structure

The first proposed system for study in this project was the cobalt-tetra-phenyl porphyrin molecule (CoTPP) deposited on the Cu(110) surface. This system was studied extensively by Phil Donovan at the University of Liverpool [3.1], giving a full exposition of the structural phases which the CoTPP molecule forms when deposited onto Cu(110). The CoTPP molecule consists of a base porphyrin molecule functionalised with 4 phenyl rings around the organic porphine core and a magnetic Co metal atom in the centre. The CoTPP molecule was found to self-assemble into a range of ordered structures on Cu(110) known as Phase 1, Phase 2 and Phase 3 [3.2].

The Phase 1 structure of CoTPP on Cu(110), shown in **figure 3.1**, is formed when CoTPP molecules self-assemble on the Cu(110) surface via intermolecular interactions between the phenyl groups attached the porphine core and a strong interaction between the porphine core itself with the Cu surface. The tendency of the porphine core, which houses the Co atom, to bond to the Cu surface and lie in a flat position causes distortions in the organic macrocycle of the molecule via the twisting of the phenyl rings. This twisting distortion leads to an interaction between the phenyl rings on adjacent CoTPP molecules. The self-assembled CoTPP islands which form are shown to have chiral confirmations on the Cu(110) surface.

Phase 1 was the most commonly observed and most well-understood structure of CoTPP on Cu(110) and as such was chosen as the initial candidate sysem for X-Ray investigation at the synchrotron. Additionally, this system already contains a transition metal centre, Co, which has the propensity for magnetic behaviour within this system making it an ideal first choice to be examined. To reinforce this choice, other similar Co porphyrin systems on Cu

surfaces have also been suggested to remain magnetically active upon adsorption by studying their active Kondo states [3.3]. With XMCD measurements at the DLS, these potential magnetic properties were able to be fully explored.
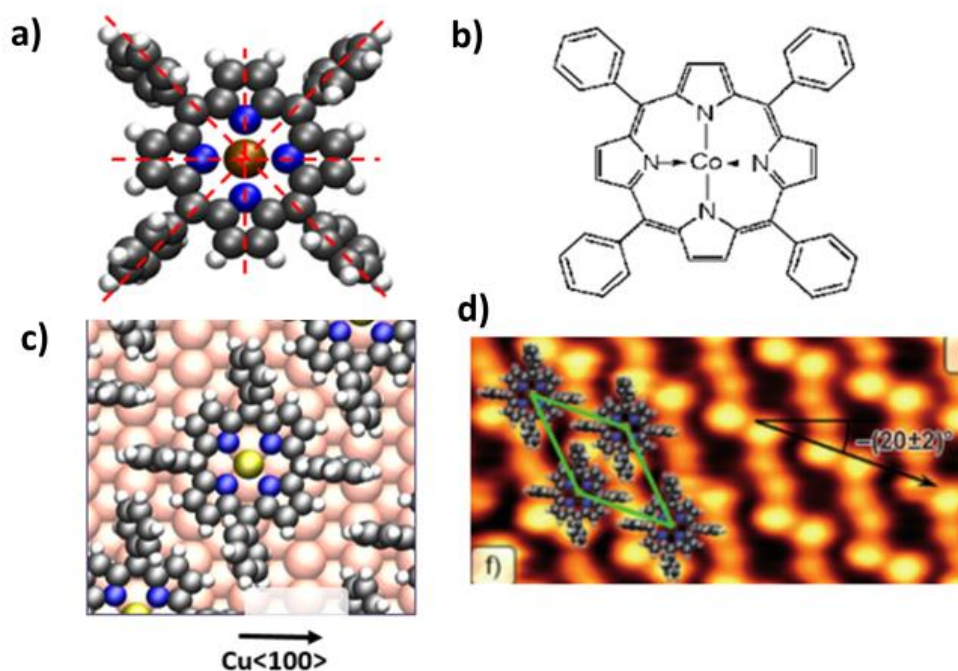

Figure 3.1: The CoTPP molecule and Phase 1 Structure on Cu(110): a) Model of the CoTPP molecule with brown Co atom shown in the centre b) Chemical structure of CoTPP c) Model of CoTPP molecule on Cu(110) in Phase 1 structure showing twisting of phenyl rings d) STM image of CoTPP Phase 1 structure on Cu(110) with superimposed molecular model. Images adapted from [3.2].

3.2 Experimental Results

3.2.1 STM Results of CoTPP/Cu(110)

The first stage of this project was to reproduce Phase 1 of the CoTPP system on Cu(110) using the conditions developed by Donovan at the SSRC. To do this, small quantities of the CoTPP, purchased from Sigma-Aldrich, were packed into a glass capillary and attached to a Knudsen cell. The filament was then attached to a feed-through and coupled to the UHV chamber. Monolayers of CoTPP were prepared by in-situ vacuum sublimation. This was done by passing a small current through the filament which heats the material causing molecules to sublime onto the surface. The dosing conditions used were 1.4A of current corresponding to around 150-165°C. These dosing conditions are within the so-called low flux regime which leads to a slow domain growth of the CoTPP islands [3.1, 3.2]. Using this low flux regime was particularly important for this project as it provides additional control over the amount of molecular material on the surface. This is important during the X-Ray stage of the investigation as it is critical that only sub-monolayer coverages of CoTPP are present. If the coverage of CoTPP exceeds that of a single monolayer then the CoTPP will begin to stack on top of the 1st layer. These additional layers no longer directly interact with the Cu(110) surface and as such molecules in this layer contain Co environments which could be different to those in the 1st layer which would interfere with the X-Ray investigation as it would no longer be explicitly clear whether any remnant magnetisation of the Co measured is due to Co environments within the 1st layer of the sample or of Co environments within additional multilayers.

In this initial experiment, suitable samples of CoTPP on Cu(110) were successfully prepared and characterised at the SSRC to verify that Phase 1 CoTPP/Cu(110) samples could be prepared using Donovan's regimen. The same Knudsen cell with the CoTPP material inside used at the SSRC was then sealed and transferred to the peripheral SIL lab at the DLS as well as the

77

Cu(110) crystals used. Using the same Knudsen cell and Cu(110) crystals which Phase 1 CoTPP/Cu(110) had already successfully been prepared with at the SSRC increases the reliability of reproducing the same desired structure at the DLS during the allocated beamtime by using the same dosing conditions.

The Phase 1 CoTPP/Cu(110) samples were then prepared at the DLS during the synchrotron experiments. The Knudsen cell was attached to the Omicron system and the crystals mounted and inserted. The Cu(110) surface was prepared by the usual Ar^+ ion sputtering and then annealing to 700K for multiple cycles until clean. The surface was then checked with STM to ensure that no contamination was present. When deposited onto the clean Cu(110) surface, using the same dosing conditions from the SSRC, STM revealed that the CoTPP molecules self-assemble to form the same chiral 2-dimensional islands at sub-monolayer coverages as expected. These structures were found to be identical to those which had prepared earlier demonstrating that they could be easily reproduced. **Figure 3.2**, shows the verification of the Phase 1 CoTPP structure with STM images taken at the DLS and comparisons of them with STM images of the same structure from the previous study [3.1].
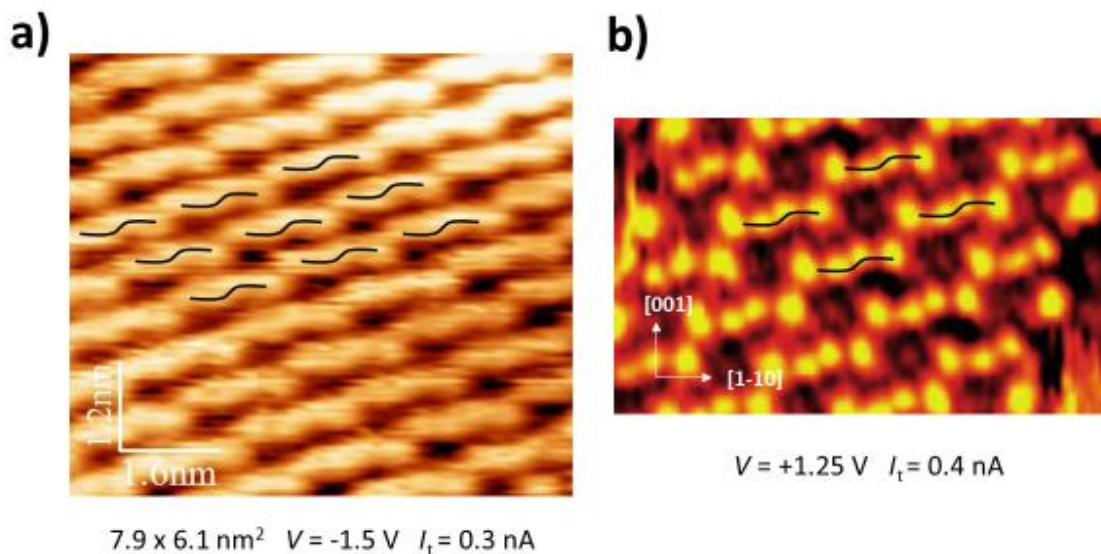
Figure 3.2: STM images of the Phase 1 CoTPP structure a) STM image (I_t = 0.3nA, V_t = -1.5V) taken at the DLS showing the s-like characteristic motif associated with the Phase 1 self-assembled structure b) comparison STM image (I_t = 0.4nA, V_t = 1.25V) from [3.2] showing the same s-like motif.

Once suitable Phase 1 CoTPP/Cu(110) samples had been produced they were transferred to the beamline and attached to the superconducting magnet ready for the X-Ray experiments. This transfer process of the sample from the peripheral UHV lab to the magnet on the beamline pioneered the use of a vacuum suitcase which allowed the sample to be transferred without ever breaking UHV conditions. The pressure was monitored during the transfer procedure and shown to not exceed 5×10^{-10} mbar throughout, ensuring that the sample remained sufficiently robust and clean before entering the magnet.

After the XMCD measurements had been conducted, the samples were also transferred back into the peripheral UHV lab for additional post-beam analysis. STM images taken at this stage showed that the nature of the Phase 1 CoTPP molecular layer had survived the transfer procedure and was not damaged during exposure to the X-Rays on the beamline. This meant that the CoTPP molecules remained intact even after exposure to the high-intensity light as expected from stable porphyrin molecules. Importantly,

post-beam STM analysis also revealed that contamination levels had been kept sufficiently low throughout the whole experimental process.

Figure 3.3 shows a large scale STM image of the exact sample which was used to obtain the following XMCD results. The STM image shows that the Phase 1 of CoTPP is the dominant structure present at ~0.5 monolayer coverage. Additional isolated CoTPP molecules were also observed to be present in this sample which was undesired; however, the quantities of these isolated CoTPP molecules were very low and furthermore these isolated molecules continue to diffuse across the Cu(110) and over time attach to the larger self-assembled Phase 1 islands. This meant that during the time taken for the sample to be transferred to the magnet the presence of these isolated CoTPP molecules would decrease further and their potential contributions to the XMCD measurements could be neglected. Similarly, extremely small quantities of second layer material and the Phase 2 structure could be observed but in such small amounts compared to the number of CoTPP molecules present in the main Phase 1 structure that they could also be safely ignored. Large scale STM images were taken at multiple points across the prepared sample to give a representation of the entire surface. This was to ensure that the Phase 1 structure was indeed the dominant phase observed and not just localised to a small area which could be observed in a single STM image area.
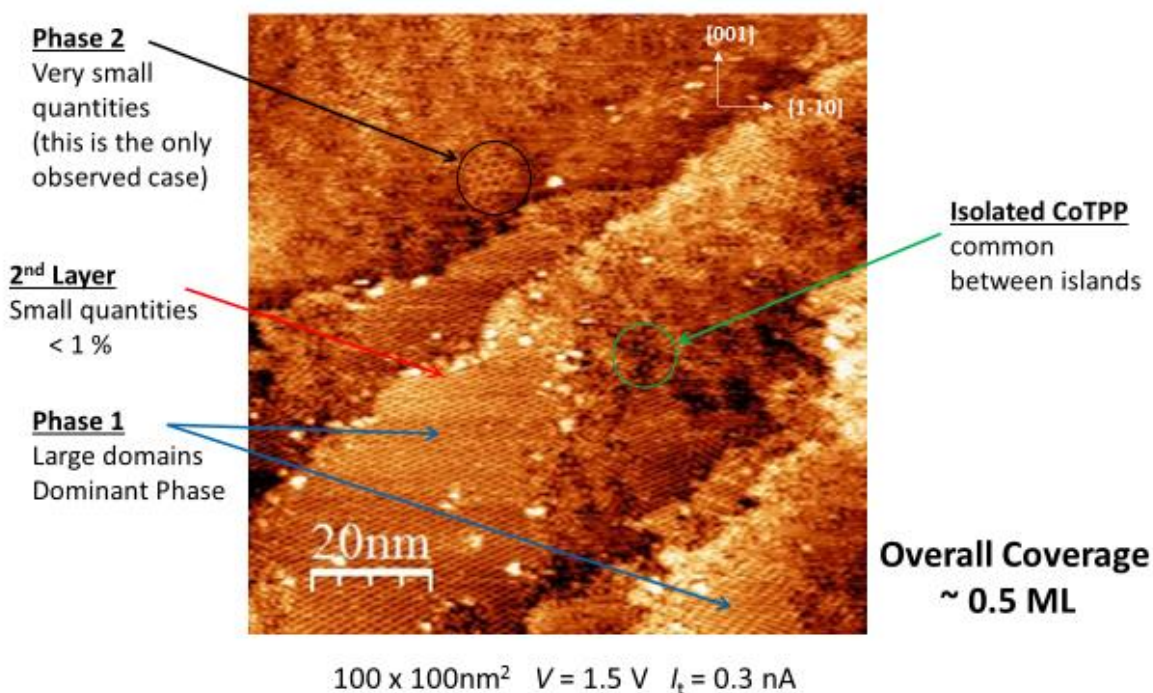
Figure 3.3: Annotated STM image of the Phase 1 CoTPP sample used for XMCD measurements (I_t = 0.3nA, V_t = -1.5V). The image shows an example area of the sample showing ~0.5 monolayer coverage of Phase 1 as well as minute quantities of isolated CoTPP, Phase 2 CoTPP and second layer CoTPP.

3.2.2   X-Ray Results of Co

3.2.2.1   XAS and XMCD Results

XAS spectra were collected using total electron yield by measuring a drain current from the sample. The absorption process causes electrons to fill the newly unoccupied states within atoms from where the excited electron originated causing a cascade of electrons through the sample which gives rise to a measurable drain current. The XAS signal was normalised against incident photon flux by measuring the drain current across one of the slits in the beamline optics hutch.

XAS spectra were collected from 765 to 820 eV corresponding to the energy region across the L_2 and L_3 absorption edges of Co: the magnetically active site in the CoTPP molecule [3.4]. The energy range of the incident light was controlled using a monochromator. XAS measurements were taken with positive (right-handed) and negative (right-handed) circular light polarisation which could be controlled by shifting the relative positions of the magnet arrays within the undulator to giving a >99% degree of polarisation. XMCD signals were then calculated by taking the difference between the absorption spectra measured with positive circular light and the absorption spectra measured with negative circular light. The I06 beamline at the DLS is equipped to perform various measurements of interest including angular dependent XAS, XMCD and XLD; temperature dependent XMCD and magnetic field dependent measurements [3.5]. All of these techniques were utilised to provide a full exposition of the magnetic behaviour of the Co ion held within the molecular ring of the CoTPP molecule adsorbed on the Cu(110) surface.

XMCD data was taken at normal ($\theta = 0°$) and grazing ($\theta = 60°$) light incidences, where θ is the angle between the incident light and the surface normal, at high external magnetic fields of up to ±6T, where +6T corresponds to a magnetic field vector parallel to that of the incident light and -6T antiparallel to the incident light. The XMCD measurements were conducted at target low temperatures of 1.5K to increase the magnetic ordering in the sample and maximise the size of any XMCD effects observed.

The XMCD signals from the Phase 1 CoTPP sample showed peaks at both the L_2 and L_3 absorption edges of Co for normal light incidence with respect to the sample (see **figure 3.4**). This indicated that the Co centre is magnetically active even upon adsorption to the Cu(110) substrate at low temperatures and high magnetic fields. The XMCD of Co shows a predominantly negative peak at the L_3 edge and a positive peak at the L_2 edge typical of XMCD spectra of 3d transition metals [3.6]. Fine structure is also observed within the L_3 and L_2 peaks unlike the single broad peaks observed in XMCD of bulk Co

[3.7]. This is due to the more localised states of the electrons in Co embedded within the CoTPP complex compared to the more delocalised states in the bulk solid state of Co [3.7].
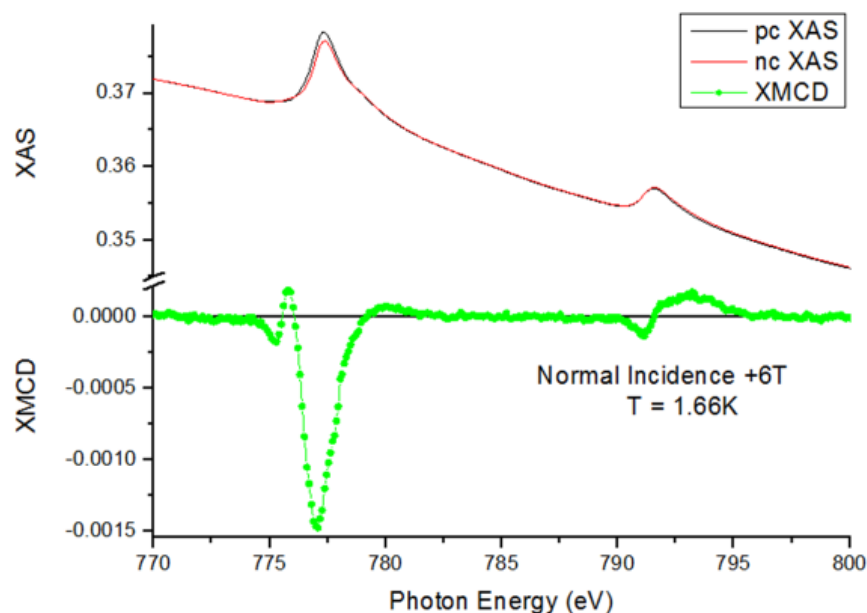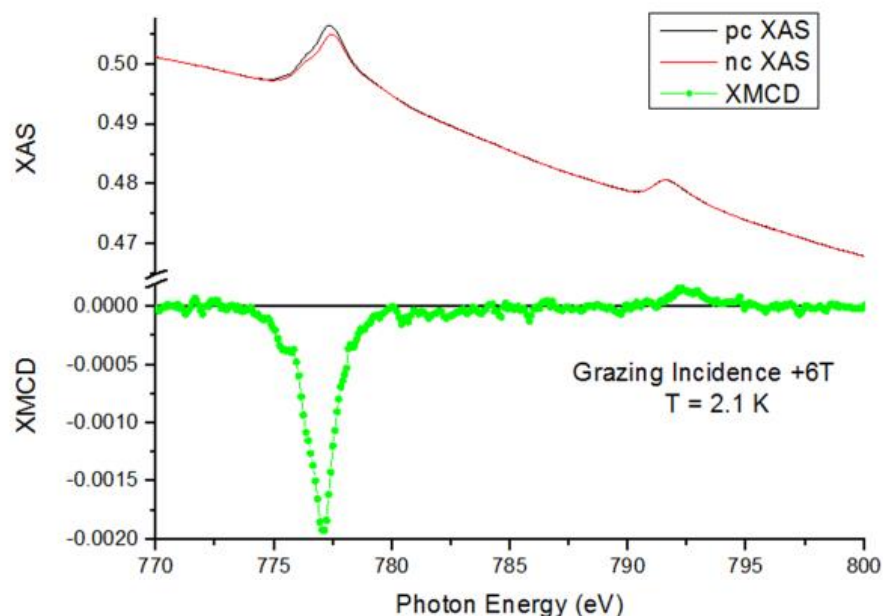

Figure 3.4: Normal Incidence ($\theta = 0°$) XAS spectra of CoTPP taken across the Co absorption range taken at 1.66K with +6T external magnetic field for positive circular (black) and negative circular (red) light polarisation at normal incidence. The resulting XMCD (green) shows peaks at both the L_2 and L_3 absorption edges indicating a magnetic response to the external magnetic field.

A simple check that the XMCD spectrum observed is indeed due to a magnetic effect is to reverse the magnetic field and measure the corresponding XMCD. Reversing the magnetic field direction should reverse the sign of the XMCD signal as the spins now align with the magnetic field in the opposite direction as previous [3.6]. This was conducted for Co at normal incidence, as shown in **figure 3.5**, producing identical XMCD spectra of opposite signs for opposite magnetic fields as expected, verifying that it is indeed a magnetic effect. The fine structure within the L_3 and L_2 peaks also switches sign upon switching the magnetic field direction illustrating that these are also contributions to the overall magnetic behaviour of the Co ion.
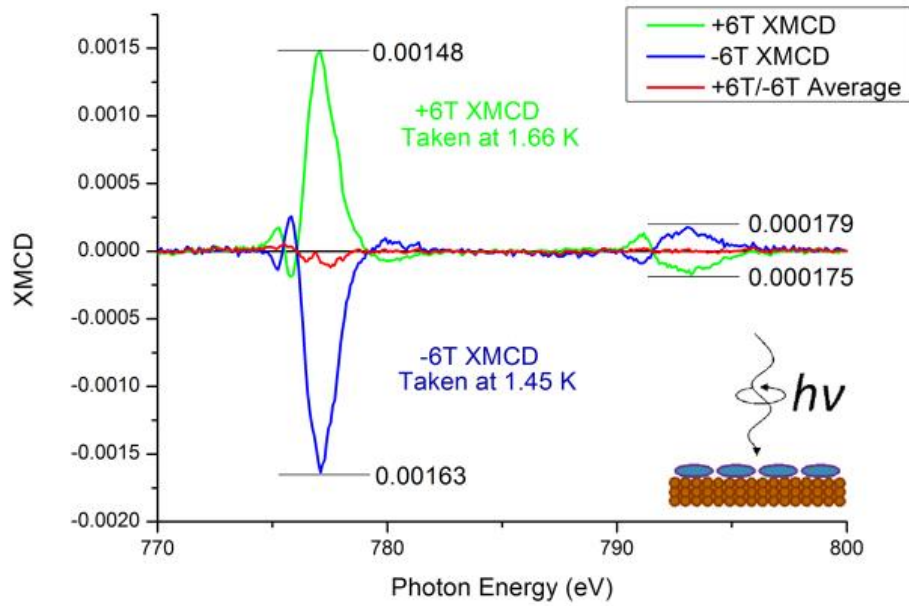
Figure 3.5: Normal Incidence (θ = 0°) comparison of XMCD spectra of Co taken at 1.66K with +6T (green) applied magnetic field and at 1.45K and -6T (blue). The average of the two curves (red) to give an indication of the degree of mismatch between the two.

To gain further insight into the behaviour of this magnetic moment on the Co ion, XMCD measurements were conducted at grazing incidence (θ = 60°) to investigate whether any magnetic anisotropy exists. By rotating the sample whilst it is in the magnet, XMCD can probe the in-plane magnetic behaviour of the Co. This can then be compared with the XMCD measured at normal incidence to give an indication as to whether there is any difference between the magnetic moment on the Co normal to the surface (normal incidence) and the magnetic moment of the Co in the plane of the surface (grazing incidence).

Figure 3.5: Grazing Incidence ($\theta = 60°$) XAS spectra of CoTPP taken across the Co absorption range taken at 2.1K with +6T external magnetic field for positive circular (black) and negative circular (red) light polarisation. The resulting XMCD (green) shows peaks at both the L_2 and L_3 absorption edges indicating a magnetic response to the external magnetic field.
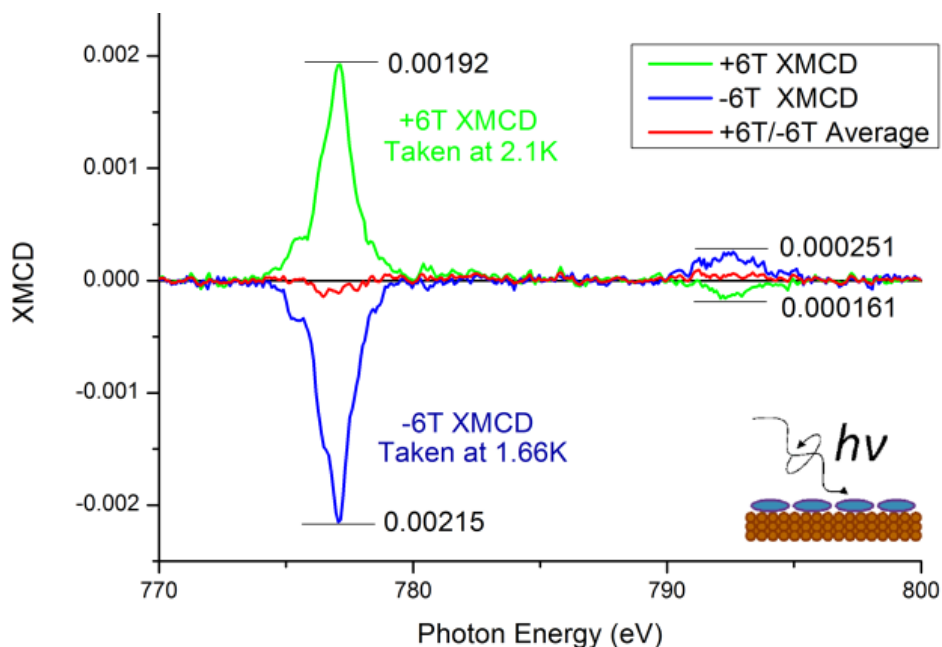
Figure 3.6: Grazing Incidence ($\theta = 60°$) comparison of XMCD spectra of Co taken at 2.1K with +6T (green) applied magnetic field and at 1.66K and -6T (blue). The average of the two curves (red) to give an indication of the degree of mismatch between the two

.

Figure 3.5 shows the XMCD signal Co measured at grazing incidence ($\theta = 60°$). As with the normal incidence XMCD signal, the grazing incidence XMCD signal showed peaks at both the L_2 and L_3 absorption edges of Co. These XMCD peaks at grazing incidence now show a fully negative peak at the L_3 edge and a fully positive peak at the L_2 edge, differing from the XMCD line shape observed at normal incidence. To more comprehensively compare the XMCD signals at each incidence and determine whether any magnetic anisotropy does exist for Co within CoTPP, sum rule analysis was conducted (shown in **Section 3.2.2.5**). This provides a quantitative measurement of the size of the spin and orbital magnetic moments responsible for the XMCD at each incidence allowing any differences between the two to be revealed.

3.2.2.2   Magnetic Field Dependence

To determine the type of magnetic behaviour exhibited by the Co ion within CoTPP, magnetic field dependent measurements were taken. These measurements investigate how the magnetic moment on the Co centre responds to changes in the external magnetic field. This was achieved by changing the magnetic field strength, typically from +6T to -6T and back again, and measuring the corresponding change in the size of the XMCD. The field was changed in 0.5T steps and short XAS scans taken across the L_3 Co edge (from 772-782 eV) at each step to observe how the size of the XMCD at the L_3 edge changes. This was conducted at both normal (**Figure 3.7**) and grazing (**Figure 3.8**) incidences with the comparison shown in **figure 3.9**. The values plotted correspond to the maximum size of the L_3 XMCD peak typically at 777 eV.
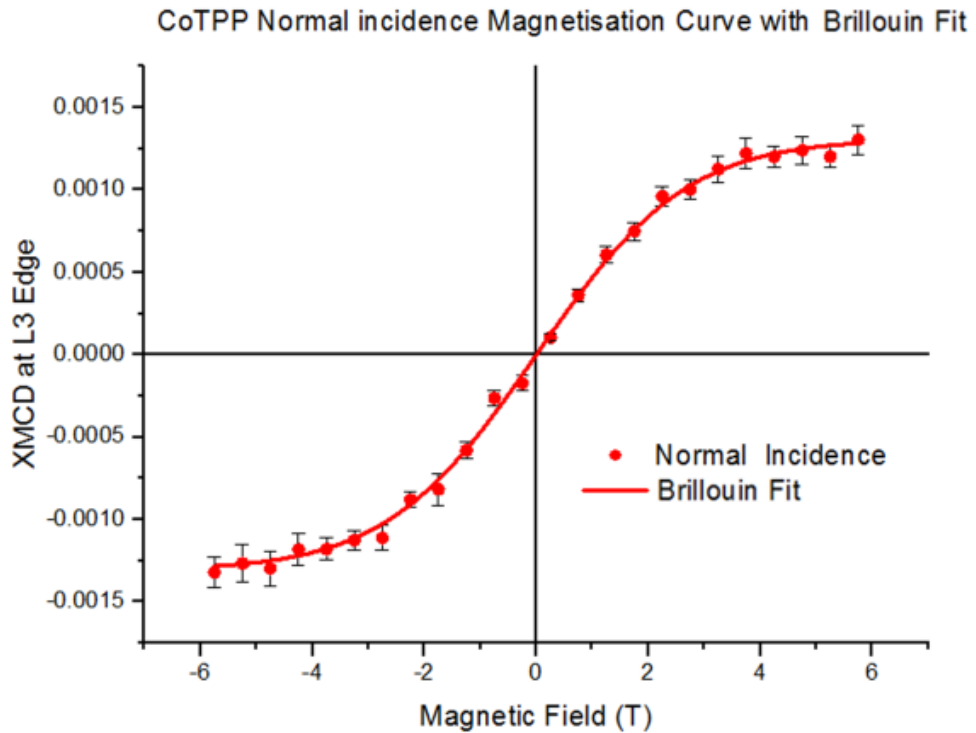
Figure 3.7: Normal Incidence ($\theta = 0°$) magnetisation curve of Co taken at 1.5K. The plot shows the size of the XMCD at the L_3 edge with changes in external magnetic field strength.
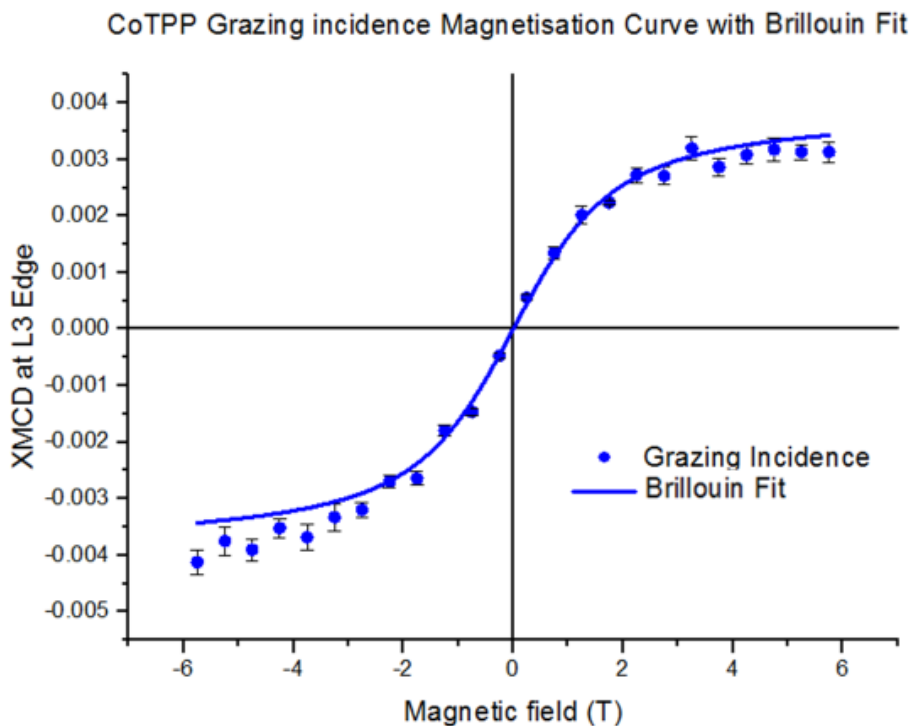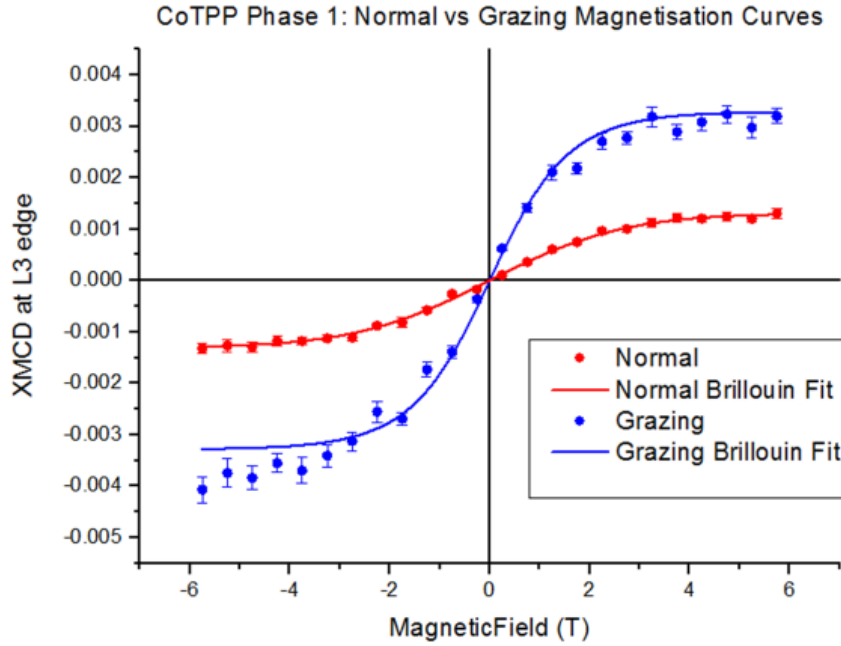

Figure 3.8: Grazing Incidence ($\theta = 60°$) magnetisation curve of Co taken at 1.5K. The plot shows the size of the XMCD at the L_3 edge with changes in external magnetic field strength.

Figure 3.9: Normal Incidence (θ = 0°, red) and grazing (incidence θ = 60°, blue) magnetisation curve of Co taken at 1.5K. The plot shows the size of the XMCD at the L_3 edge with changes in external magnetic field strength.

The curves were fitted to a Brillouin function to give an indication of the type of magnetic behaviour observed:

$$B_J(x) = \frac{2J+1}{2J}\coth\left(\frac{2J+1}{2J}x\right) - \frac{1}{2J}\coth\left(\frac{1}{2J}x\right) \tag{3.1}$$

Where *B* is the applied external magnetic field and *J* is related to the total angular momentum quantum number of the microscopic magnetic moments of the Co ion [3.8, 3.9]. The close fitting of these curves to the measured experimental data illustrate that the spins of the Co ions within the CoTPP molecules behave as an ideal paramagnet.

These magnetisation curves reveal a paramagnetic response of the magnetisation of the Co centre to the applied external field for both normal and also grazing sample orientations. The XMCD measured is proportional to the

magnitude and sign of the external magnetic field applied as expected of a paramagnetic material. There is saturation in the size of the XMCD signal of Co at around +4T/-4T external magnetic field strengths. There is no indication of any hysteresis behaviour on the Co as the XMCD signal is 0 when no magnetic field is applied. This indicates that there is no long range magnetic coupling between the Co centres of neighbouring molecules which is reasonable considering the large separation between the Co centres within the molecules.

The magnetic response of the Co is much greater at grazing incidence compared to that of normal incidence, highlighting that there is an easy-axis of magnetisation in the plane of the sample. This is evidenced by the steeper slope through the origin of the curve for grazing incidence as well as a greater maximum XMCD value at saturation. This gives rise to an anisotropy in the magnetic moment of the Co centre with a dominant contribution lying in the plane of the surface. This is further explored with sum rule analysis in **Section 3.2.2.5.**

3.2.2.3   Temperature Dependence

Along with standard angle-dependent XMCD scans, temperature dependent measurements were also taken to determine whether this magnetic behaviour was still active at higher temperatures. The magnitude of the Co L_3 XMCD peak at 777 eV was monitored as the temperature of the sample increased from 1.5K. **Figure 3.10** shows a decrease in the size of the L_3 XMCD Co peak as the temperature is increased, which approximately follows a Curie type of relationship for paramagnetic systems: as the temperature decreases there are fewer thermal fluctuations in the spins and they become more ordered and aligned in the direction of the external magnetic field leading to a larger magnetisation and thus a larger measured XMCD signal.
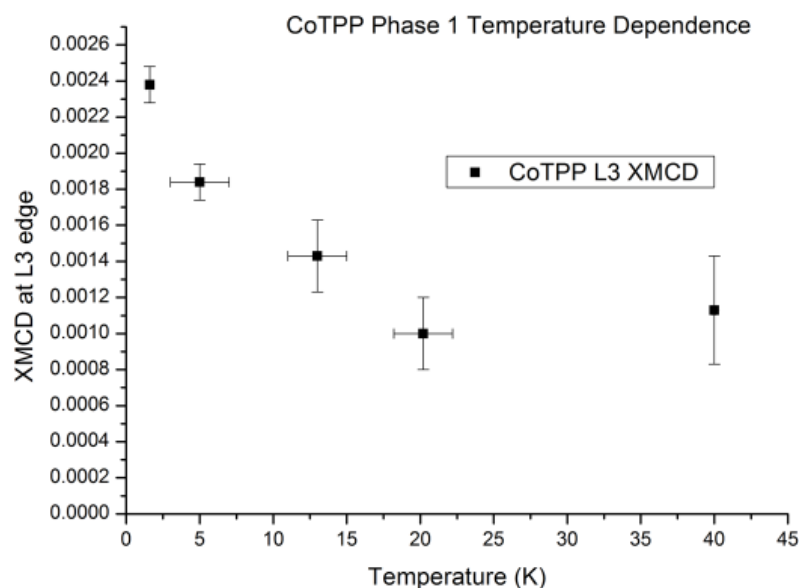
Figure 3.10: Temperature dependent XMCD measurements of the Co taken at normal incidence ($\theta = 0°$) and +6T external magnetic field. The XMCD signal strength decreases with increasing temperature.

3.2.2.4 X-Ray Linear Dichroism

As well as conducting XAS measurements using circularly polarised light to determine the XMCD spectra of the Co centres, XAS using linearly polarised light was conducted to probe the orientation of the valence orbital states involved in the absorption process. The XLD spectra were taken by measuring the difference between XAS spectra measured with horizontally polarised light and vertically polarised light. This was conducted at both normal (**Figure 3.11**) and grazing (**Figure 3.12**) incidences, under a small magnetic field of +0.1T to improve the quality of the measured spectra. There is small misalignment between the linear and vertical XAS spectra due to a change in the background absorption contribution as the photon energy increases. This has been corrected using a background linear subtraction on the resulting XLD spectrum.

90
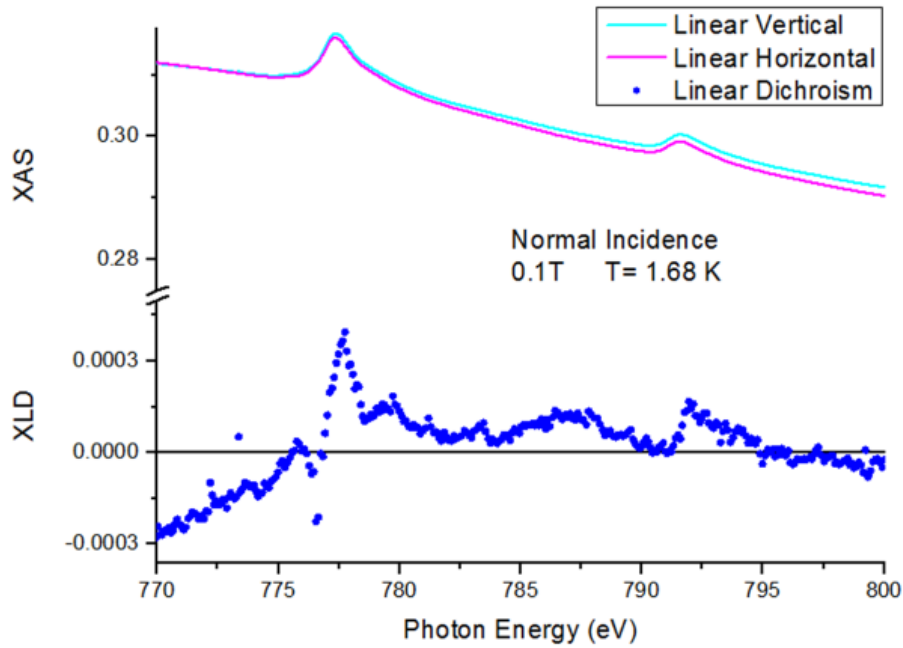
Figure 3.11: Normal Incidence (θ = 0°) XAS spectra of CoTPP taken across the Co absorption range taken at 1.66K with +0.1T external magnetic field for horizontal (pink) and vertical (cyan) linear light polarisation. The resulting XLD (blue) is almost 0 and much smaller than the measured XAS themselves.
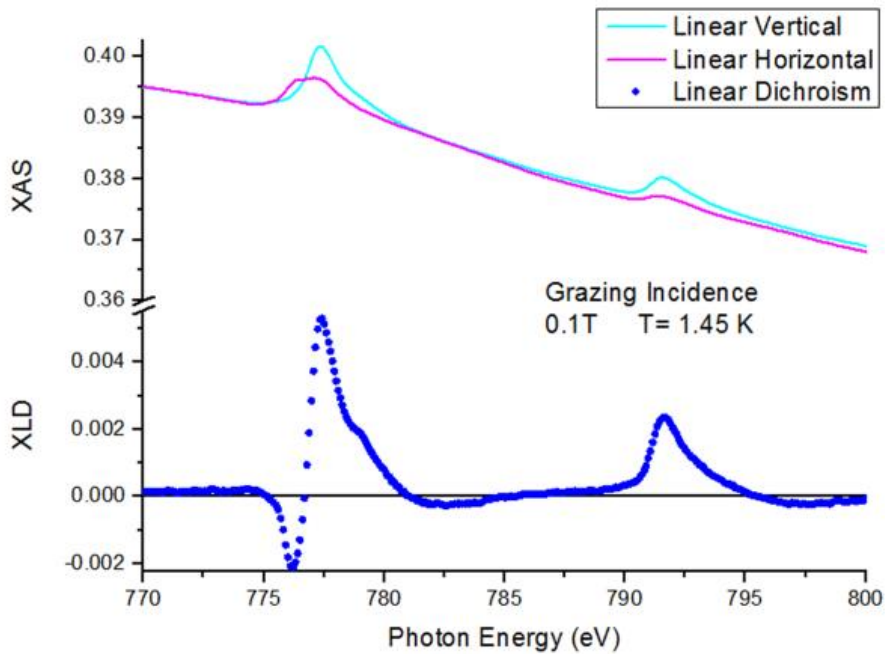

Figure 3.11: Grazing Incidence (θ = 60°) XAS spectra of CoTPP taken across the Co absorption range taken at 1.45K with +0.1T external magnetic field for horizontal (pink) and vertical (cyan) linear light polarisation. The resulting XLD (blue) shows a large difference highlight that valence orbital states lie in plane of the surface.

The normal incidence XLD spectra reveal no significant change in the absorption between horizontally or vertically polarised spectra. At grazing incidence there is a much larger XLD suggesting that valence orbitals involved in the absorption lie in plane of the surface. It is important to note that this is not sufficient evidence to conclude that all in plane orbitals are responsible for the magnetic behaviour of the Co centre observed, as only partially spin filled orbital states provide a net magnetic moment. Fully unoccupied orbital states contribute to the size of the measured XAS absorption signal but do not contribute to the XMCD signal. Further consideration using Density Functional Theory calculations provides a more complete basis to determine which orbital states are responsible for the magnetic behaviour of the Co centre which is observed (discussed in **Section 3.3**).

3.2.2.5 Sum Rule Analysis

The XMCD measurements of the Co centre within the CoTPP molecule revealed that a finite magnetic moment was present on the Co and that a magnetic anisotropy existed between normal and grazing incidences. To gain a deeper understanding into these results, sum rule analysis was conducted to calculate the explicit spin m_{spin} and orbital m_{orb} moments of the Co centre at both normal and grazing incidences (equations 3.2 and 3.3). This was achieved using the sum rules outlined in **Section 2.3.2** with an additional cos θ factor to account for the different angles of the incident light with respect to the surface normal [3.7].

$$m_{orb} = -\frac{4 \int_{L_3+L_2}(\mu_+ - \mu_-)dE}{3 \int_{L_3+L_2}(\mu_+ + \mu_-)dE} \frac{(10 - n_{3d})}{cos\theta} \qquad (3.2)$$

$$m_{spin} = -\frac{6\int_{L_3}(\mu_+ - \mu_-)dE - 4\int_{L_3+L_2}(\mu_+ - \mu_-)dE}{\int_{L_3+L_2}(\mu_+ + \mu_-)dE}$$
$$* \frac{(10 - n_{3d})}{cos\theta}\left(1 + \frac{7\langle T_z \rangle}{2\langle S_z \rangle}\right)^{-1} \qquad (3.3)$$

Values were calculated for these moments by taking integral values across the appropriate peaks in the XAS and XMCD spectra. A background subtraction was conducted on the total XAS spectra (the sum of the positive and negative circularly polarised spectra) and integral values taken across the entire energy region. The n_{3d} is the occupancy of the electronic d-states of the Co ion in the molecule. In the gas phase of CoTPP the Co ion exists as Co^{2+} corresponding to a d^7 state; however charge transfer between the Co ion and the Cu atoms in the Cu(110) surface leads to a change in this value. Density Functional Theory calculations (see **Section 3.3**) reveal that the Co picks up $0.087e^-$ of charge from the Cu surface which gives a value of n_{3d} of 7.087 which was used for these sum rule calculations.

The magnetic spin moment m_{spin} sum rule includes a contribution from T_z which is the intra-atomic magnetic dipole moment [3.10, 3.11]. This term can be largely ignored for bulk systems of transition metals [3.7] but is more significant in low-dimensional systems such as molecules on surfaces [3.12]. The value cannot be determined explicitly from the XMCD measurements alone and as such the spin moment sum rule can be approximated to give a value m^*_s for the effective spin moment which includes this contribution from T_z and the contribution from the isotropic spin moment m_{spin} [3.12].

At normal incidence the sum rule calculations yield $m^*_s = 0.23 \pm 0.03$ μ_B and $m_{orb} = 0.10 \pm 0.02$ μ_B. At grazing incidence the sum rule calculations yield $m^*_s = 0.42 \pm 0.06$ μ_B and $m_{orb} = 0.22 \pm 0.03$ μ_B. Compared to the values of

m_{spin} and m_{spin} (1.98 and 0.086 respectively) of bulk Co measured using XMCD and sum rules calculations [3.7], the value of m_{spin} for Co in the CoTPP molecule is much smaller whereas the value for m_{orb} is larger as expected due to the orbital moment quenching in bulk ferromagnetic materials.

The XMCD spectra and magnetisation curves there is a greater total magnetic moment present at grazing incidence which gives rise to the in plane magnetic anisotropy. The easy axis of magnetisation at grazing incidence can be attributed to the larger value in the orbital moment m_{orb} compared with the value of m_{orb} at normal incidence. These calculated magnetic moments reveal that the Co centre of the CoTPP molecule remains substantially magnetic upon adsorption to the non-magnetic Cu(110).

3.3 Density Functional Theory Results of CoTPP/Cu(110)

To elucidate the origins of the magnetic behaviour of the Co ions within the Phase 1 CoTPP/Cu(110) system, density functional theory calculations were performed. These were conducted by John Sharp as part of Prof Mats Persson's group at the University of Liverpool using a DFT+U approach. **Figure 3.12**, shows the results of these calculations. The U term is related to a value of the Coulombic repulsion within the *d* orbitals and is self-consistently determined.
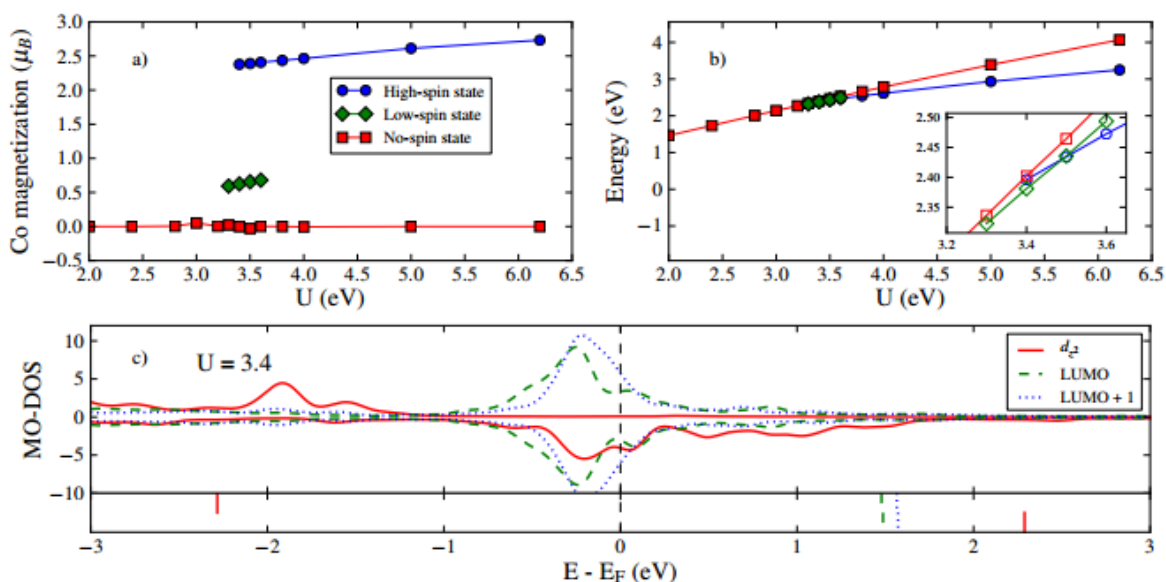
Figure 3.12: DFT results of CoTPP on Cu(110) showing a) Predicted values of Co total magnetic moments and spin states b) Stabilisation energies as a function of U parameter used in the calculations and c) Projected density of states of the partially filled d_z^2 orbital states which lie around the Fermi level E_F.

It was found that the calculated value of the total magnetic moment on Co was very sensitive to the value of the U parameter used as seen in the variation of possible spin states in **figure 3.12a**. The DFT results revealed the presence of a low-spin Co state using a U value of 3.4eV, consistent with the electronic ground states of the gas phase CoTPP low-spin state and other studies of Co porphyrins on Cu [3.3]. In this low spin state the total magnetic moment of the Co ion is calculated at 0.63 μ_B which is comparable to the value

of the total magnetic moment ($m^*_s + m_{orb}$) of 0.64 μ_B calculated with sum rules which shows a high degree of agreement.

The d_z^2 orbital states are shown in the molecular density of states map in **figure 3.12c**. These d_z^2 orbital states are partially filled and spin split thus responsible for the magnetic behaviour of the Co ion observed in the XMCD results. The d_z^2 orbital states have the greatest overlap with the orbital states of the Cu surface which causes the strong interaction between them leading to charge transfer. Compared with the gas phase CoTPP, the d_z^2 orbital states pick up 0.087e$^-$ charge from interactions with the Cu surface. The degree of charge transfer between the Co ion and Cu surface directly influences the extent to which the d_z^2 orbital states are filled and subsequently the magnetic properties of the Co. This degree of charge transfer between the Co ion and the surface is much smaller than in other studies of Co complexes on metal surfaces (0.5e$^-$ charge transfer for CoTPPBr on Cu(110) [3.3] and 0.39e$^-$ charge for CoPc on Au(111) [3.12]) and explains why the Co of CoTPP was more magnetic than other systems. This means that the magnetic properties of these systems are highly dependent on their interactions with the surface. This reflects the sensitivity between molecule-substrate interaction and the resulting magnetic properties.

With the DFT results indicating that the origin of the magnetic behaviour of the Co ion results from partially filled d_z^2 orbital states, the magnetic anisotropy observed in the XMCD measurements can also be explained. The XMCD results and sum rule calculations showed a greater magnetic moment in the plane of the surface compared to out of plane. This is consistent with partially filled d_z^2 orbital states as these states lie out of plane of the surface between the Co ion and the Cu surface. This means that the orbital moments generated by electrons within these d_z^2 states are perpendicular to it or in the plane of the surface in agreement with the experimental results

3.4 Conclusions

In this initial experiment into molecular spintronics, suitable samples of Phase 1 CoTPP on Cu(110) were successfully prepared and characterised and their magnetic properties measured using XMCD. The XMCD measurements indicated that the Co centre of the CoTPP molecule exhibits significant magnetic behaviour when complexed to an organic porphine macrocycle and adsorbed onto the Cu(110) surface. Sum rule calculations revealed that there is an unusually large orbital moment contribution to the total magnetic moment. The total magnetic moment is also anisotropic with a greater contribution in the plane of the surface. Magnetisation dependent curves showed that the Co is paramagnetic in this environment, unlike bulk ferromagnetic Co, with saturation in magnetisation at +4T/-4T. One notable result was that the XMCD effect was still present at temperatures up to 220K, albeit significantly diminished. This could potentially mean that materials of this ilk are still magnetically active at around room temperature, reinforcing their viability for applications in spintronic devices.

The most significant result in this experiment was simply the verification that the Co centre does indeed retain some magnetic functionality when adsorbed on a non-magnetic substrate supported by DFT calculations. The other results are encouraging as it supports the possibility of using these magnetic molecular systems as materials in spintronic devices. To further this investigation, the molecular architecture of the CoTPP molecule was altered in order to explore whether structural changes in the system affect the magnetic behaviour of the Co centre. This is exactly what was done in the next stage of the project by synthesising cobalt di-phenyl porphyrin: a modified version of CoTPP which forms 1-dimensional chain structures on Cu(110).

3.5 Cobalt Tetraphenyl Porphyrin on Cu(110) References

[3.1]   P. Donovan *et al. Unexpected Deformations Induced by Surface Inter-action and Chiral Self-Assembly of Co(II)-Tetraphenyl-porphyrin ad-sorbed on Cu(110).* Chem. Eur. J. 16, 38, 11641-11652. (2010).

[3.2]   P. Donovan. *Adsorption and Self-assembly of Cobalt(II)-Tetraphenyl porphyrin on Cu(110).* PhD thesis, University of Liverpool (2009).

[3.3]   U. Perera, *et al. Spatially Extended Kondo State In Magnetic Mole-cules Induced by Interfacial Charge Transfer.* Phys. Rev. Lett. 105, 106601 (2010).

[3.4]   J. Bearden, A. Burr. *Reevaluation of X-Ray Atomic Energy Levels.* Rev. Mod. Phys. 39, 125 (1967).

[3.5]   Diamond Light Source I06 beamline specifications: http://www.dia-mond.ac.uk/Beamlines/Surfaces-and-Interfaces/I06.html

[3.6]   Stöhr, J & Siegmann, H. *Magnetism: From Fundametnals to Na-noscale Dynamics.* Springer Series in Solid-State Sciences. (2006).

[3.7]   Chen, C. *et. al. Experimental Confirmation of the X-Ray Magnetic Cir-cular Dichroism Sum Rules for Iron and Cobalt.* Phys. Rev. Lett. 75, 1 (1995).

[3.8]   C. Kittel. *Introduction to Solid State Physics.* 8th Edition. Wiley. p 303-304 (2005).

[3.9]   J. Takacs. *Approximations for Brillouin and its reverse functions.* Brit. J. Appl. Phys. 18, 1415-1417 (1967).

[3.10] A. Scheybal *et al. Induced Magnetic Ordering in a Molecular Mono-layer. Chem. Phys. Lett.* 411, 214-220. (2005).

[3.11] Stöhr, J. *X-ray magnetic circular dichroism spectroscopy of transition metal thin films.* J. Electron. Spectrosc. 75, 253 (1995).

[3.12] Stepanow, S. *et al. Mixed-valence behaviour and strong correlation effects of metal phthalocyanines adsorbed on metals. Phys. Rev. B.* 83, 220401 (2011).

4 Cobalt Diphenyl Porphyrin on Cu(110)

4.1 1-Dimensional Molecule Chains on Surfaces

The experiments on CoTPP/Cu(110) system proved to be successful showing that a magnetic moment of the Co centre remained present even when adsorbed on the Cu(110) surface. To continue this investigation, other porphyrin systems were chosen which exhibit different structural behaviour on the Cu(110) surface. The aim was to investigate whether structural differences in the porphyrin systems can influence the magnetic properties of the Co centre.

One ideal candidate for this next investigation was the diphenyl porphyrin system (DPP) on Cu(110) which had been studied at the University of Liverpool [4.1, 4.2]. These molecules were shown to form 1-dimensional molecular chain-like structures along the [001] direction on the Cu(110) surface on heating to around 550K. This annealing process causes a scission of C-H bonds on the porphyrin macrocycle, liberating H from C atoms from the ring. Cu atoms from the surface then rise up to form C-Cu-C bonds as shown in **figure 4.1**. This organometallic bond, mediated by Cu, joins DPP molecules together through the C atoms in their organic macrocycle, causing the molecules to assemble into 1-dimensional chain structures along a preferred [001] direction which can be clearly imaged using STM. These chain-like nanowires are well-defined and can be up to 20 molecules in length, extending over several nanometres. The DPP molecule also scavenges Cu atoms from the surface to fill the centre of porphine core.

To investigate the potential magnetic properties of such a system, the DPP molecule was functionalised with a Co central ion to enable direct comparisons with the Phase 1 CoTPP system on Cu(110). The new CoDPP molecule was synthesised by David Amabilino's group at the Institute of Material

Science of Barcelona. The CoDPP molecules were then deposited onto Cu(110) to determine whether the same 1-dimensional structures could be created for this new magnetic variant of DPP. If so, this new structure could be studied with XMCD experiments to investigate whether the change in structure leads to any change in magnetic behaviour of Co compared to that of the Phase 1 CoTPP structure. Furthermore, the 1-dimensional chain structures of DPP molecules are always formed along the [001] direction which means that it is possible to investigate how whether this 1-dimensional structural anisotropy of the system has any influence on the magnetic properties of the Co ions. This is of particular interest as 1-dimensional molecular structures which exhibit anisotropic magnetic properties would have many applications to molecular spintronics.
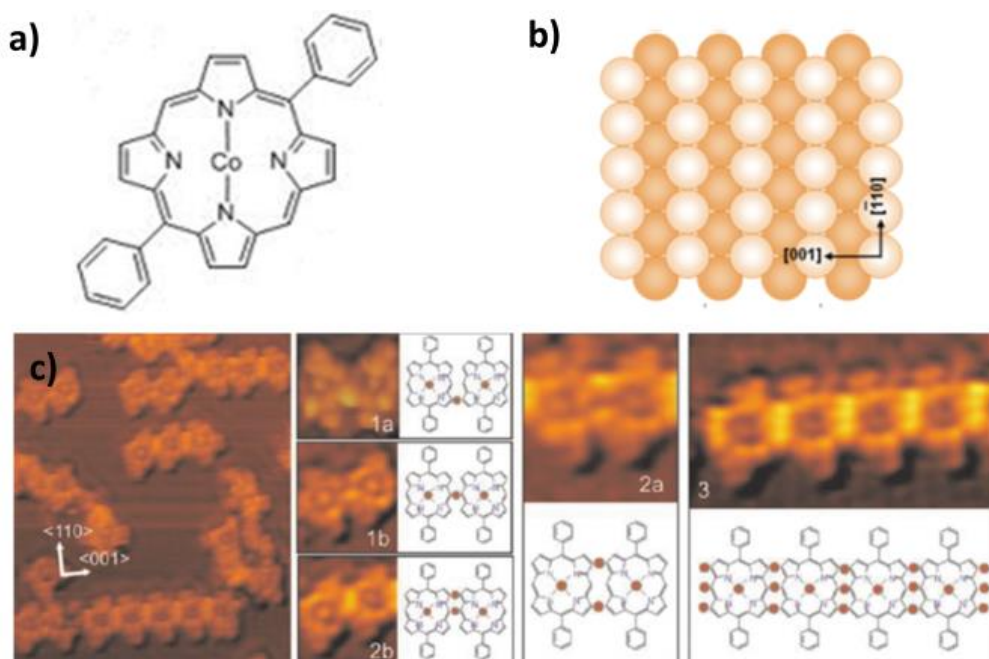
Figure 4.1: 1-dimensional structures on Cu(110) a) The chemical structure of the CoDPP molecule b) Cu(110) surface, preferred growth of the chains on this surface occurs along the [001] direction c) STM images and molecule schematics of the base DPP (initially without any central metal ion) revealing the bonding mechanism between the Cu atoms in the surface and the organic porphine macrocycle. Image adapted from [4.1].

4.2 Experimental Results

4.2.1 STM Results of CoDPP/Cu(110)

The first stage of this experiment was to verify that the 1-dimensional molecular chains observed for DPP could still be created for the new CoDPP molecule. This was investigated using STM at the SSRC. The CoDPP molecules were prepared using a Kundsen cell as described with the CoTPP molecules in **Chapter 3.** Dosing conditions used were similar to CoTPP: 1.4A current and around 150-165ºC. After initial deposition of the CoDPP onto the Cu(110) surface, no molecules could be observed by STM. This was concluded to be due to the high mobility of the molecules on the surface, which move faster than the scanning speed of the STM tip and as a consequence are unable to be resolved at room temperature.

Upon annealing to approximately 550K molecules begin to link together and become visible with STM (see **Figure 4.2**). The CoDPP molecules are shown to link together along the [001] as was observed with the DPP molecule on Cu(110). Even at higher coverages the CoDPP molecular chains remained robust. No isolated CoDPP molecules were observed even after the annealing step although there was evidence of diffusion perpendicular to the molecular chains which could be attributed to CoDPP molecules which are mobile on the surface at room temperature. These cases are rare and as such it is assumed that the majority of the molecules present on the surface are formed into the molecular chains after annealing.
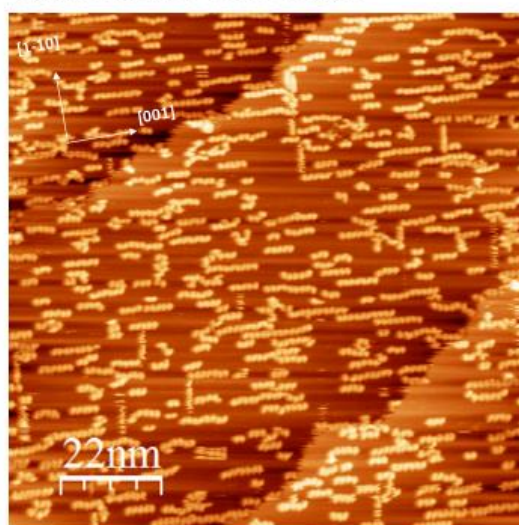
110 x 110nm² V = -1.2 V I_t = 0.5 nA
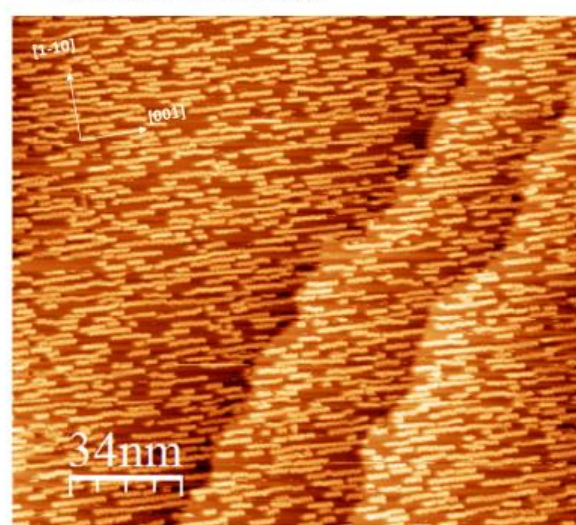
170 x 150nm² V = -1 V I_t = 0.1 nA

Figure 4.2: STM images of the linked CoDPP molecular chain structure formed along the [001] direction on Cu(110) taken at the SSRC after annealing at 550K a) Medium Coverage (110 x 110nm², I_t = 0.5nA, V_t = -1.2V) b) High coverage (170 x 150nm², I_t = 0.4nA, V_t = 1.25V).

One interesting feature of the system is that even after dosing large quantities of the CoDPP molecules onto the Cu(110) surface (greater than a single monolayer of material), well-formed molecule chains are still formed after the annealing step as shown in **figure 4.3**. This means that any second layer material which is present on the surface after the initial deposition is desorbed during the process of annealing to form the molecular chains. This makes it easy to produce large complete coverages of the CoDPP molecular chains without the need for precise dosing conditions. This is advantageous for industrial applications of the system as the chain structure can be easily reproduced on a large scale across the surface. Additionally, for this investigation in particular, being able to produce a homogenous structure across the whole surface means that the largest possible amount of molecular material is present on the surface. This is advantageous during the X-Ray measurements as the quantity of Co on the surface is maximised allowing for the largest possible XAS and potential XMCD signals to be measured. The desorption of second layer material also ensures that there are no Co environments which are non-interacting with the surface which would interfere with the desired XAS

results from the Co environments which are directly interacting with the surface.
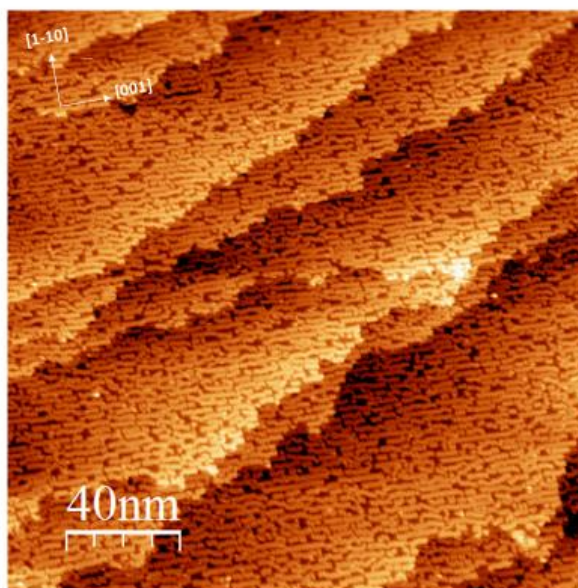
200 x 200nm² $V = -1.2$ V $I_t = 0.25$ nA

Figure 4.3: STM image of high coverage of linked CoDPP in the molecular chain structure along the [001] direction on Cu(110) for a overdose of material greater than a single monolayer. Image shown post-annealing at 550K (200 x 200nm², $I_t = 0.3$nA, $V_t = -1.5$V). No visible second layer molecules are observed

For the original DPP structure, it was observed that after the annealing stage, Cu metal atoms from the surface rise up and fill the empty porphine core. This is visible in STM images which show the presence of these Cu atoms in the centre of the molecule. For the CoDPP system, STM images showed large bright spots in the centre of the molecules attributed to the Co ions highlighting that the Co ion remains complexed to the porphyrin after the annealing process (**figure 4.4**). Bridging Cu atoms between the molecules are also visible.
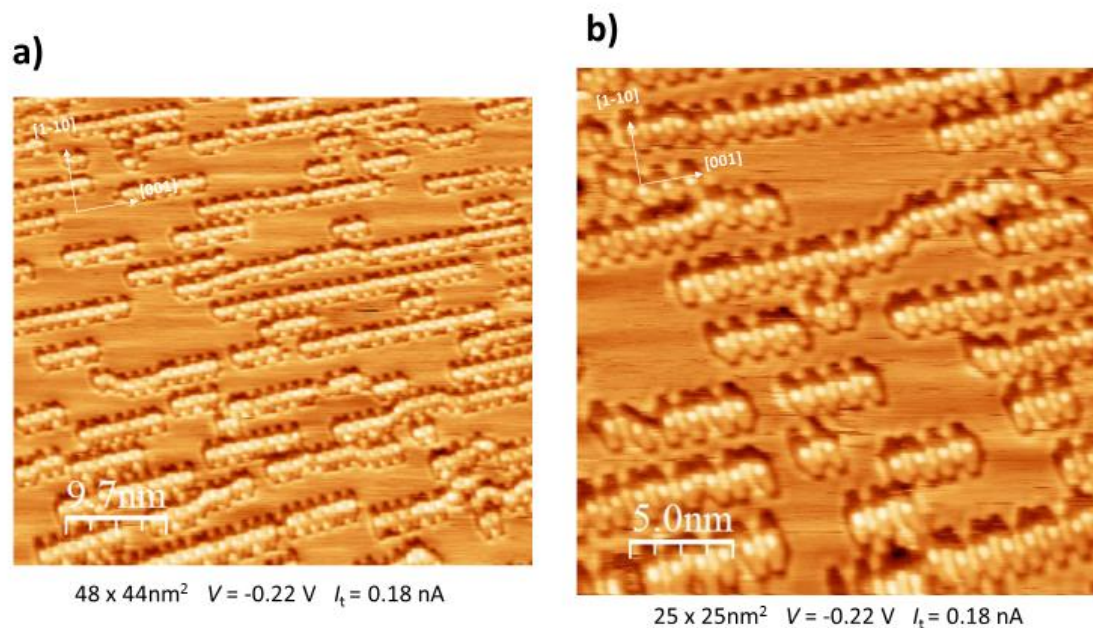
Figure 3.4: STM images of the linked CoDPP molecular chain structure showing features of individual molecules including central Co ions and linking Cu bridges a) STM image conditions: 48 x 44nm^2, I_t = 0.18nA, V_t = -0.22V b) 25 x 25nm^2, I_t = 0.18nA, V_t = -0.22V.

The CoDPP molecule was found to successfully produce the identical molecular chain structures to those previously obviously for the base DPP. The STM studies revealed that the CoDPP molecular chains were highly ordered and could be produced at high coverages with little distortion to the overall structure of the chain. The 1-dimensional nature of this system makes it an ideal candidate for probing whether the structural anisotropy of the system has any influence over magnetic anisotropy of the Co ions within it. To do this, the system was again reproduced at the DLS for XMCD studies to investigate these magnetic properties.

4.2.2 Orientation of CoDPP Structures

This CoDPP molecular chain system was reproduced at the DLS to investigate the magnetic behaviour of the Co centre using XMCD. For this investigation, angular dependent XMCD was the principal measurement used to determine whether the structural anisotropy of 1-dimensional CoDPP molecular chains induces any anisotropic effect in the magnetisation of the Co centre. In order to probe this potential anisotropic effect due to the molecular chain directions, XMCD measurements would need to be taken of the molecular chains in different orientations and then compared with each other to elucidate whether there is any indeed change in magnetic behaviour. A maximal anisotropic effect, if any, would be evident by the comparison of grazing incidence XMCD measurements of molecular chains which are perpendicular with respect to each other. Ideally, this would be achieved by performing the grazing incidence XMCD measurements for one particular orientation of molecular chains and then rotating the sample by 90° and performing the same measurements again thus allowing a comparison to be made using a single sample.

Unfortunately, in this investigation the orientation of the sample is fixed once inside the superconducting magnet and therefore it was not possible to rotate the sample during the XMCD measurements. This meant that different samples had to be prepared which were comprised of chains in the two different orientations. These two systems were termed 'horizontal chains' for molecular chains which have been grown horizontally with respect to the incoming X-Ray beam and 'vertical chains' for molecular chains which have been grown vertically with respect to the incoming X-Ray beam. The grazing incidence XMCD measurements of these two separate systems could then be compared to determine whether the orientation of the CoDPP molecular chains has any influence on the magnetic anisotropy of the Co centre.

To create each of these desired samples, Cu(110) crystals had to be physically mounted along certain known crystallographic directions to alter the orientation of chain growth with respect to the incoming X-Rays once on the beamline. This was achieved using Low-Energy Electron Diffraction (LEED) on a clean Cu(110) to find the orientation of the crystallographic axes. Crystals were then removed and realigned by eye to the desired orientation to within ±5⁰ and remounted onto the sample plates. This was done to produce two aligned Cu(110) crystals: one with [001] direction vertical (with respect to the sample position once inside the magnet on the beamline) and one with [1-10] direction vertical; the chains would grow either vertically or horizontally on each of these two crystals. **Figure 3.5** shows the resulting LEED images after the Cu(110) had been aligned along desired crystallographic axes along with schematics showing the positioning of the sample plate and subsequently the orientation of the molecular chains once the sample is in the beamline.
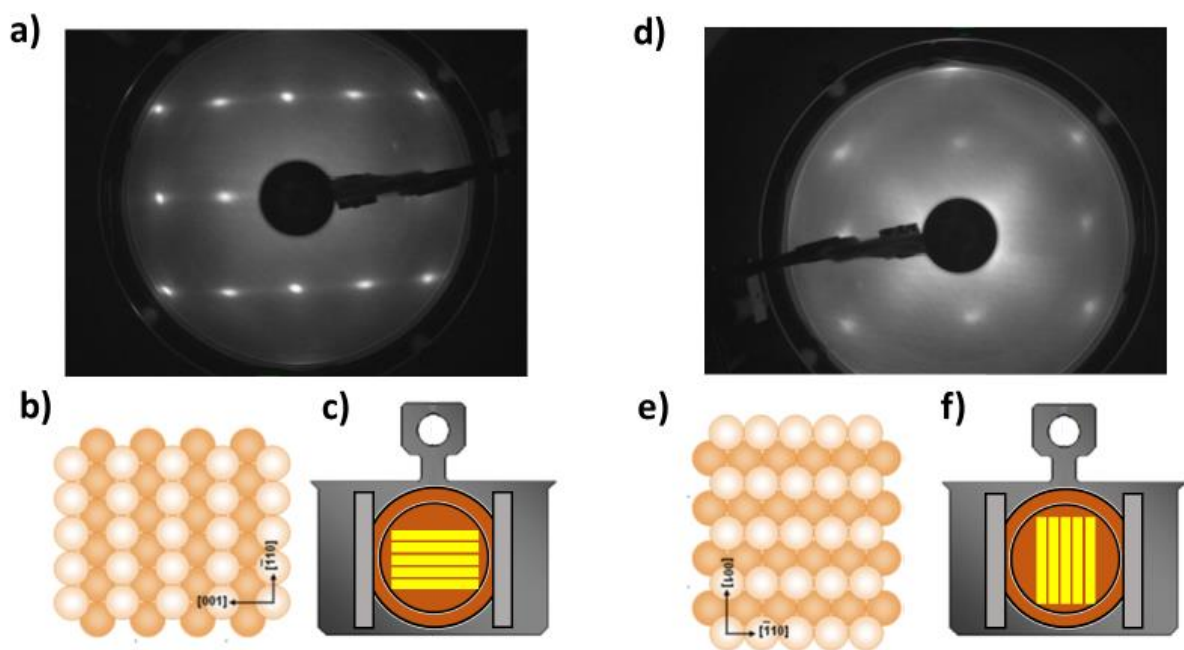
Figure 4.5: Orientation of Cu(110) for desired CoDPP molecular chain growth: a) LEED image taken at 65eV showing [001] direction horizontal b) Associated Cu(110) orientation and c) Sample position inside the magnet with horizontal chains directional growth (yellow) d) LEED image at 78eV showing [001] direction vertical e) associated Cu(110) orientation and f) Sample position showing vertical chain directional growth (yellow).

CoDPP molecules were then deposited on each of these crystals and annealed to produce the linked CoDPP molecular chains as observed during previous experiments. **Figure 4.6** shows images of the samples grown with horizontal and vertical chains for each of these orientated crystals. These two samples were then measured using XMCD on the beamline.
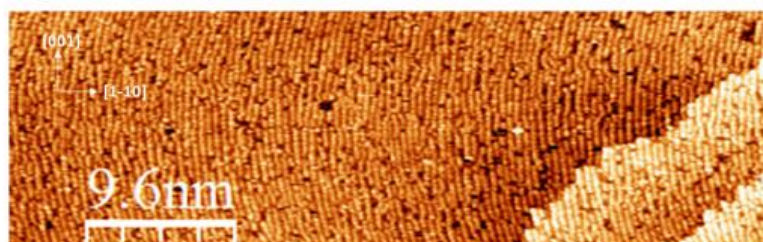
a) Horizontal Chains
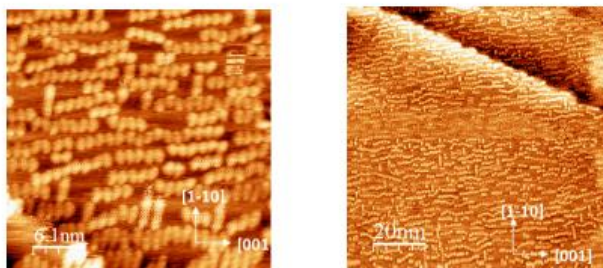
b) Vertical Chains

Figure 4.6: STM images of the linked CoDPP molecular chain system taken at the DLS during beamtime for a) Horizontal chain growth (Left 30 x 30nm^2, $I_t = 1$nA, $V_t = -1.2$V and right 48 x 44nm^2, $I_t = 1$nA, $V_t = -1.2$V) and b) Vertical Chain growth (48 x 15nm^2, $I_t = 0.8$nA, $V_t = -1.5$V).

Post-beam analysis of the CoDPP chain samples, performed as explain in **Section 3.2.1**, showed that the molecular chains could still be observed even after exposure to X-Rays, highlighting that the 1-dimensional structure remains robust throughout the experiment.

4.2.3 X-Ray Results of Co in CoDPP

XMCD measurements were taken to compare the two samples: the 'horizontal chains' system and the 'vertical chains' system. It is important to note that at normal light incidence, with the external magnetic field direction perpendicular to the surface, the two sample arrangements are expected to produce equivalent XAS and subsequent XMCD spectra. This is because at normal incidence the direction of the external magnetic field and hence the magnetisation of the Co is normal to the surface, rendering any XMCD measurement independent of the direction of the chains. Any anisotropy in the magnetic behaviour of the Co centre based on the structural orientation of the chains can only be revealed when measuring the XMCD at grazing incidence. In this arrangement, XMCD measurements now probe the magnetic behaviour of the Co centre along the direction of the chains for the horizontal orientation or perpendicular to the direction of the chains for the vertical orientation. By comparing the grazing incidence XMCD measurements between the two vertically and horizontally aligned samples it will be possible to elucidate whether any magnetic anisotropy exists based upon the structural anisotropy of the chain systems.

XAS measurements were once again taken with positive (right-handed) and negative (right-handed) circular light polarisation, XMCD signals were then calculated by taking the difference between the two. As mentioned the crucial measurement in this experiment was the angular dependent XMCD, particularly at large angles, as comparison of these measurements for the horizontally and vertically aligned samples would reveal whether any anisotropy exists: the crux of this experiment.

4.2.3.1 Horizontal Chain System

The following results are for the case of a single monolayer of linked CoDPP molecular chains aligned horizontally with respect to the incident light. XAS spectra were again collected in the 765 to 820 eV energy range across the L_2 and L_3 absorption edges of Co at normal ($\theta = 0°$) and grazing ($\theta = 60°$) light incidence for both +6T and -6T magnetic fields at a target temperature of 1.5K.

The XMCD signals for the horizontal CoDPP sample shows very small peaks at both the L_2 and L_3 absorption edges of Co for normal light incidence with respect to the sample (see **figure 4.7**). This indicates that the Co centre remains magnetically active upon adsorption to the Cu(110) substrate and when coordinated into molecular chains; however, the magnetic moment is quenched, even at low temperatures and high magnetic fields. The magnitude of the XMCD is significantly smaller than that measured for Co in the Phase 1 CoTPP structure on Cu(110): the XMCD signals at the L_3 edge of Co in CoTPP is around 3 times larger than that of Co in the CoDPP system.
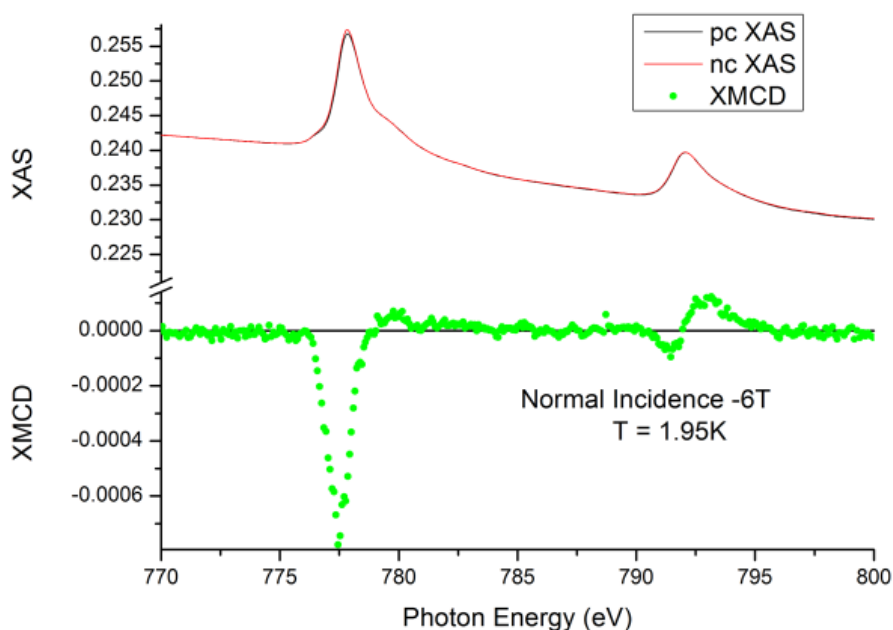

Figure 4.7: Normal Incidence ($\theta = 0°$) XAS spectra of CoDPP taken across the Co absorption range taken at 1.95K with -6T external magnetic field for positive circular

(black) and negative circular (red) light polarisation at normal incidence. The resulting small XMCD (green) shows peaks at both the L_2 and L_3 absorption edges indicates a weak magnetic response to the external magnetic field.

Once again the magnetic field was reversed and the resulting XMCD was shown to also flip sign (**figure 4.8**).
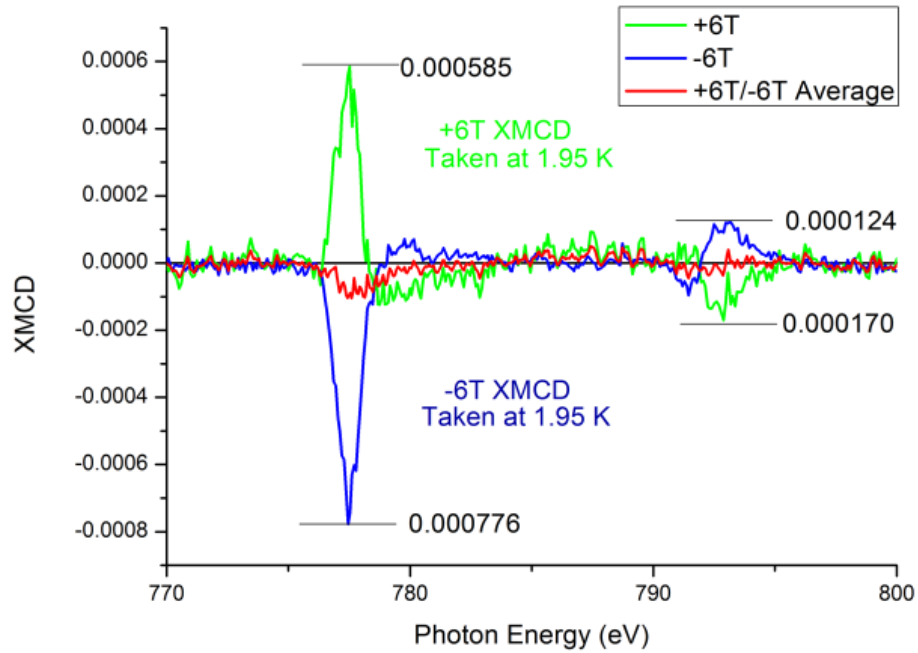

Figure 4.8: Normal Incidence ($\theta = 0°$) comparison of XMCD spectra of Co taken at 1.95K with +6T (green) applied magnetic field and -6T (blue). The average of the two curves (red) to give an indication of the degree of mismatch between the two.

Whilst the XMCD signal could be replicated with similar features for the reverse magnetic field, the effect is very weak with a significant amount of noise in the signal.

XMCD measurements were then conducted at grazing incidence ($\theta = 60°$) for the horizontal chains (**figure 4.9**) for -6T and +6T with their comparisons shown (**figure 4.10**). The XMCD signal is much broader and noisier with an XMCD peak only resolvable at the L_3 edge.
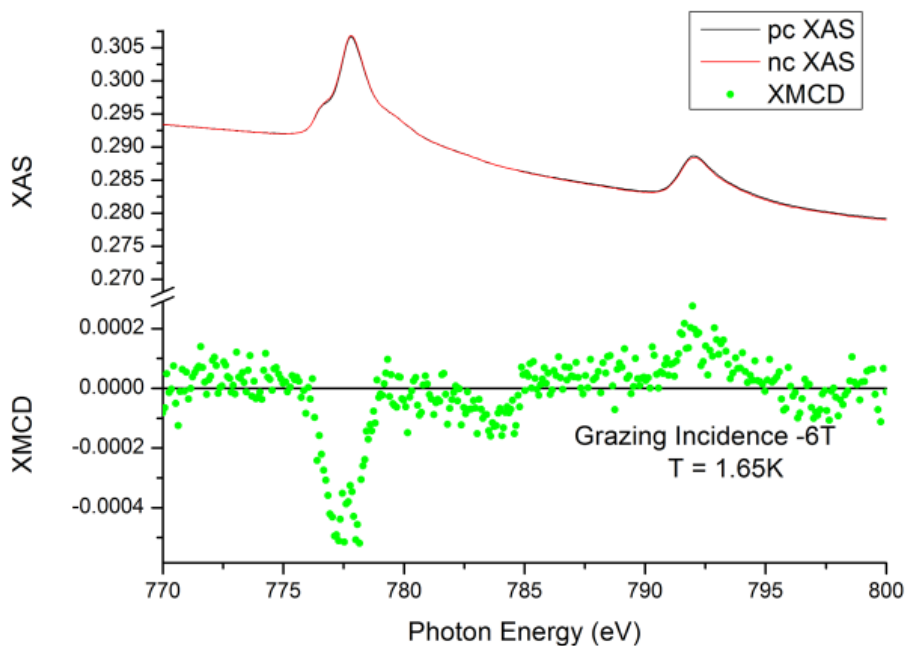
Figure 4.9: Grazing Incidence (θ = 60°) XAS spectra of CoDPP taken across the Co absorption range taken at 1.65K with -6T external magnetic field for positive circular (black) and negative circular (red) light polarisation. The resulting XMCD (green) shows some activity at the L_3 edge.
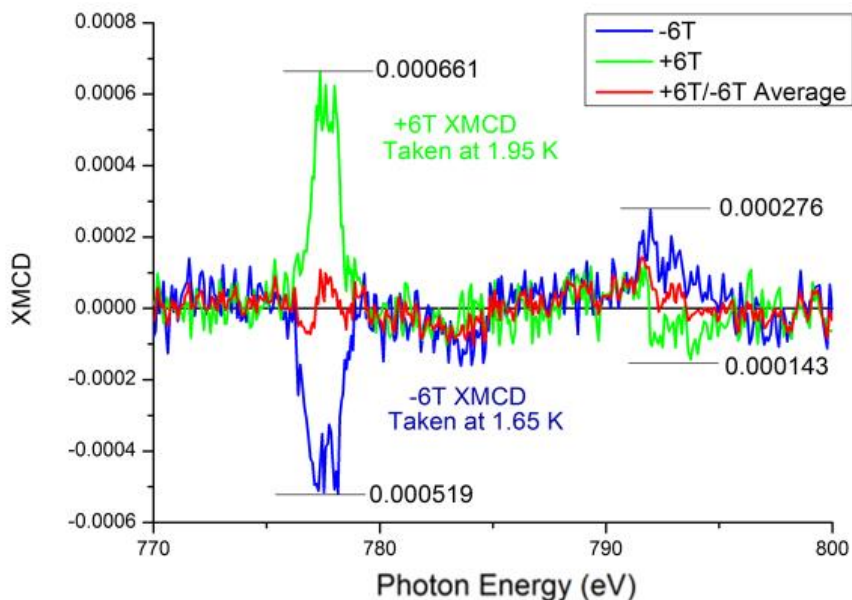

Figure 4.10: Grazing Incidence (θ = 60°) comparison of XMCD spectra of Co taken with +6T (green) applied magnetic field and -6T (blue). The average of the two curves (red) gives an indication of the degree of mismatch between the two.

Magnetisation-dependent measurements were performed for Co within the horizontal chains although due to the small size of the XMCD signal these produced very large errors (**figure 4.11**). The measurements plotted are the size of XMCD signal at the L_3 peak (at 778eV) divided by XAS background at the pre-edge (at 775eV). This was done to allow for the XMCD measurement to be normalised against the molecular surface coverage so that it could be more easily compared to the vertical chain sample even if molecular surface coverages were slightly different. The Co shows a paramagnetic response to the external magnetic field similar to the Phase 1 CoTPP system. Whilst there appears to be a larger magnetic moment out of plane rather than in plane, the XMCD effect itself is so small compared to the inherent noise with very large fluctuations for grazing incidence measurements, that it is difficult to explicitly state that this is the case.
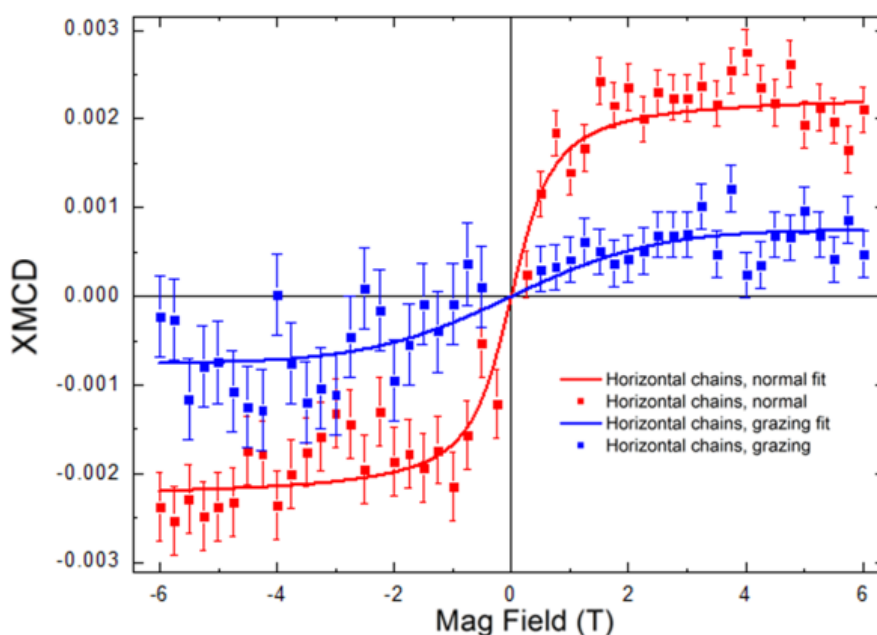

Figure 4.11: Normal Incidence ($\theta = 0°$, red) and Grazing Incidence ($\theta = 0°$, blue) magnetisation curves of Co taken at 1.5K. The plot shows the size of the XMCD at the L_3 edge (at 778eV) with changes in external magnetic field strength normalised against the XAS pre-edge (at 775eV).

There is again no indication of any hysteresis behaviour on the Co and no evidence of any long range magnetic coupling between Co centres.

4.2.3.2 Vertical Chain System

An identical set of XMCD measurements were performed for the 'vertical chain' system. The XMCD signals for the vertical CoDPP sample showed very small peaks at both the L_2 and L_3 absorption edges of Co for normal light incidence with respect to the sample (see **figure 4.12**).
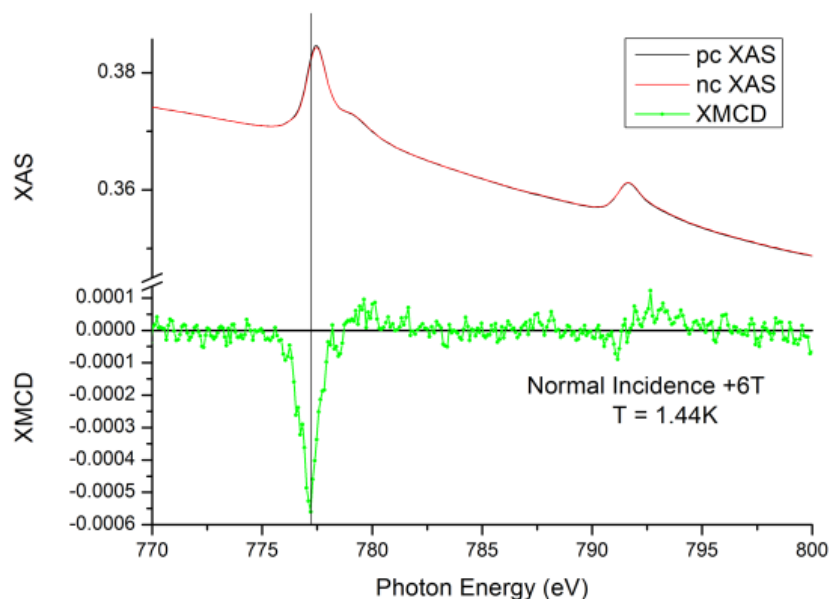

Figure 4.7: Normal Incidence ($\theta = 0°$) XAS spectra of CoDPP taken across the Co absorption range taken at 1.44K with -6T external magnetic field for positive circular (black) and negative circular (red) light polarisation at normal incidence. The resulting small XMCD (green) shows peaks at both the L_2 and L_3 absorption edges indicates a weak magnetic response to the external magnetic field.

Once again the magnetic field was reversed and the resulting XMCD was shown to also flip sign (**figure 4.13**).
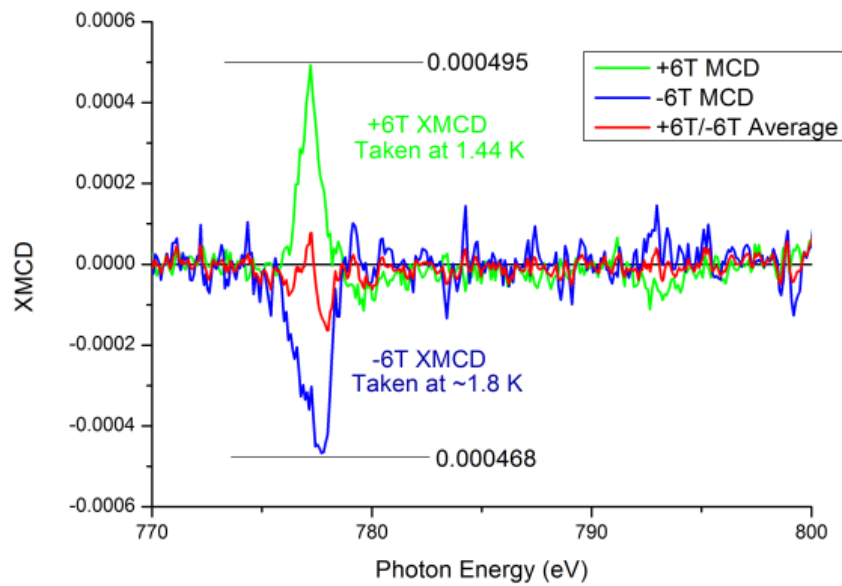
Figure 4.13: Normal Incidence (θ = 0°) comparison of XMCD spectra of Co taken at 1.44K with +6T (green) applied magnetic field and at 1.8K and -6T (blue). The average of the two curves (red) to give an indication of the degree of mismatch between the two.

The XMCD signal can be seen to be present at both magnetic field directions but again the effect is very weak with a significant amount of noise in the signal especially at the L_3 edge.

To compare the effect of vertical chains against the horizontal chain system XMCD measurements were then conducted at grazing incidence (θ = 60°) for the vertical chains (**figure 4.14**) for -6T and +6T with their comparisons shown (**figure 4.15**). A resulting XMCD signal was measured at the L_3 edge but no resolution of a signal could be made at the L_2 edge.
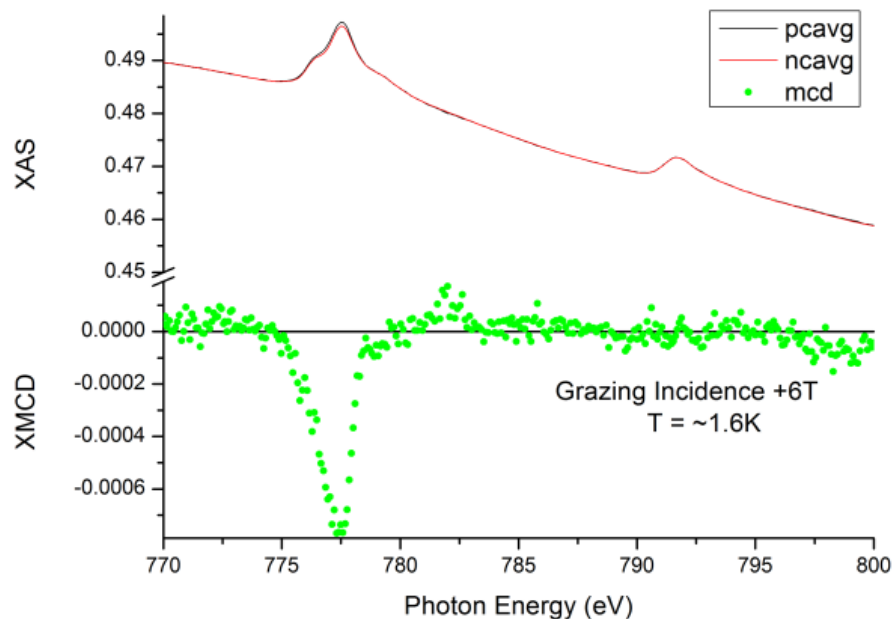
Figure 4.14: Grazing Incidence (θ = 60°) XAS spectra of CoDPP taken across the Co absorption range taken at 1.6K with +6T external magnetic field for positive circular (black) and negative circular (red) light polarisation. The resulting XMCD (green) shows some activity at the L_3 edge.
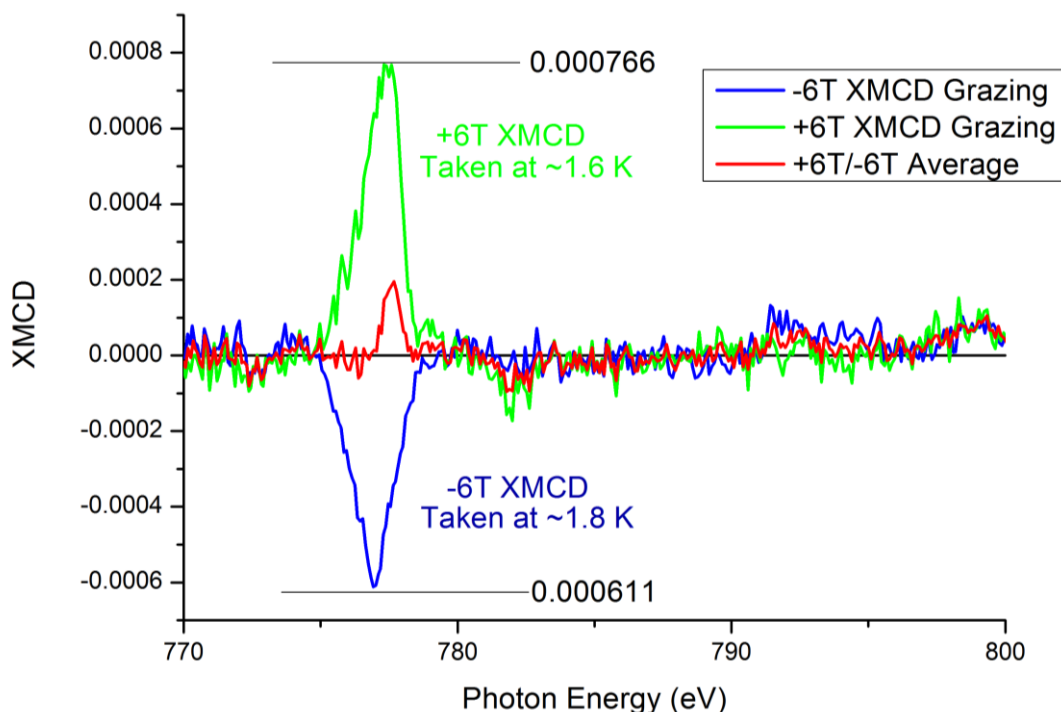

Figure 4.15: Grazing Incidence (θ = 60°) comparison of XMCD spectra of Co taken at 1.6K and +6T (green) applied magnetic field and at 1.8K and -6T (blue). The average of the two curves (red) to give an indication of the degree of mismatch between the two.

Finally, magnetisation-dependent measurements were performed for Co within the vertical chains showing a paramagnetic response at normal and grazing incidence (**figure 4.16**).
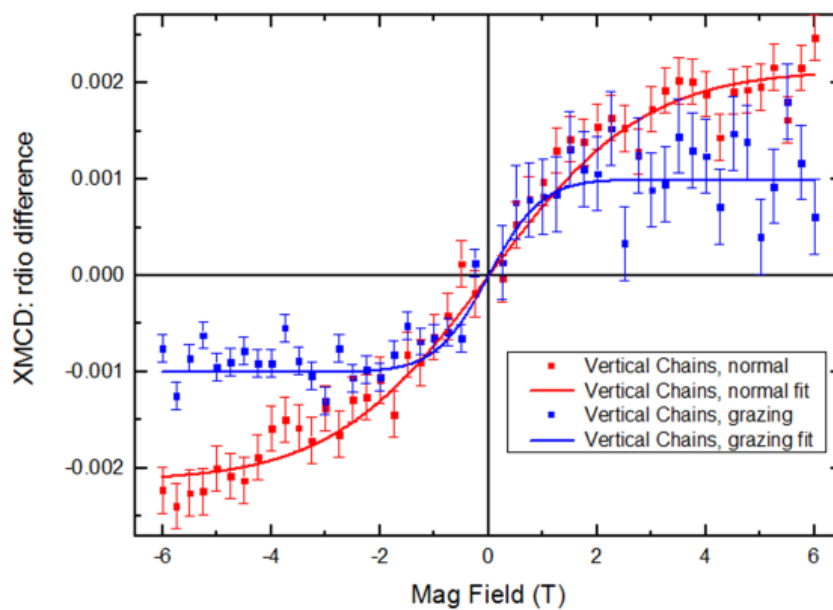

Figure 4.16: Normal Incidence (θ = 0°, red) and Grazing Incidence (θ = 0°, blue) magnetisation curves of Co taken at ~1.5K. The plot shows the size of the XMCD at the L₃ edge with changes in external magnetic field strength.

.

4.2.3.3 Horizontal and Vertical Comparisons

XMCD measurements from both the horizontal and vertical arrangements reveal that the Co centre within the CoDPP molecule is only very weakly magnetic when adsorbed on the Cu(110) substrate. The XMCD signal on Co is almost completely quenched in this system for each external magnetic field direction and at each angle. Magnetisation curves suggest that a larger out of plane moment is present for both horizontal and vertical chain systems but again this effect is small with large errors associated with measured signals.

The comparison of grazing incidence measurements are of most interest in this investigation to be able to compare the effect of the chain structure direction on the magnetic behaviour of the Co centre. **Figure 4.17**, shows a comparison of the magnetisation dependent measurements for the horizontal and vertical chain systems at grazing incidence. The curves are similar and with no distinguishable differences able to be made between the two, largely due to the significant errors associated with such weak signals.
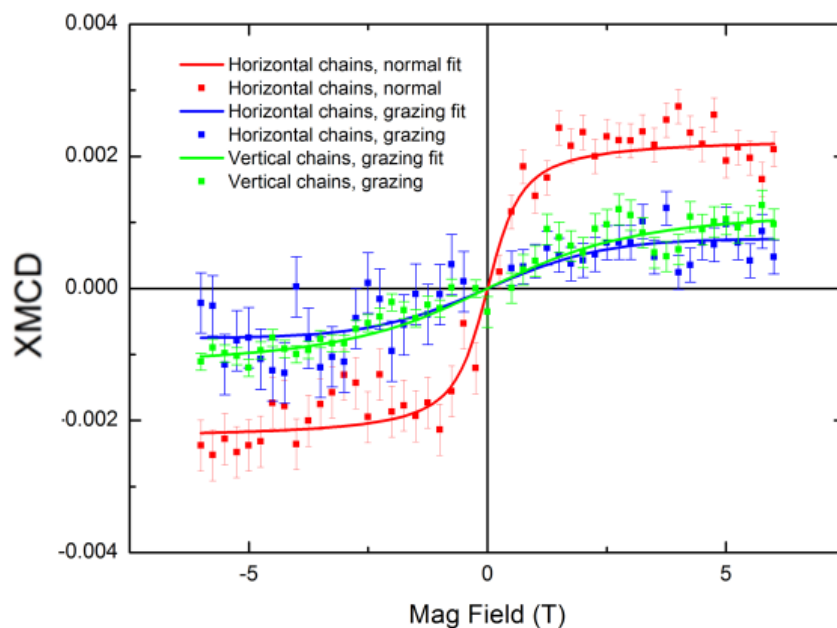
Figure 4.17: Comparisons of magnetisation dependent XMCD measurements on horizontal chains at grazing incidence (blue) and vertical chains at grazing incidence (green).

4.3 Conclusions

The CoDPP/Cu(110) samples were successfully prepared in the SIL facility with molecular chain growth in the desired directions: horizontally and vertically with respect to the incoming X-Ray beam. The magnetic behaviour of Co in the linked CoDPP molecular chains is almost entirely quenched and difficult to measure with XMCD. The XMCD signal is much smaller than that measured for the Co centre within the Phase 1 CoTPP on Cu(110) explored in **Chapter 3**. This is most likely due to an increased interaction between the CoDPP and the Cu(110) surface compared to that of CoTPP and the Cu(110) surface.

These strong molecule-surface interactions have been explored in similar experiments involving Co complexes on metal surfaces. For Co porphyrins on Cu(111), a large degree of charge transfer from the Cu surface to the Co

ion occurs which almost entirely fills the Co d_{z^2} orbital states [4.5], most intimately involved in the magnetic behaviour of the Co, resulting in an almost complete quenching of the magnetic moment. Similarly, Co ions within Co phthalocyanines on Au(111) [4.6] and Au(110) [4.7] show no magnetic response in XMCD measurments at 8K and 5T external magnetic fields for sub-monolayer coverages of molecular material owing to direct interactions with the surface.

Whilst the XMCD signal from the CoDPP chains was largely quenched there are some conclusions that can be drawn from it. This investigation provides evidence that modifying the molecular architecture around the Co centre of the porphyrin complex, from CoTPP molecule in **Chapter 3** to the CoDPP molecule in this chapter, does indeed influence its magnetic behaviour. Additionally, it highlights how sensitive the magnetic properties of the Co centre can be to small changes in the Co environment. Clearly, there is a large structural dependence of the strength of the magnetic moment observed dependent on how the assembled molecular structures affect the strength of interaction between the Co ion and the Cu surface. In the case for CoDPP this interaction was too strong and quenched the magnetic moment but by devising a way to reduce or even completely decouple a monolayer of material from the surface, it should be possible to preserve the magnetic activity of these molecules.

4.4 Cobalt Diphenyl Porphyrin on Cu(110) References

[4.1]   S. Haq *et al. Clean Coupling of Unfunctionalized Porphyrins at Surfaces To Give Highly Oriented Organometallic Oligomers*. J. Am. Chem. Soc. 133, 12031-12038. (2011).

[4.2]   F. Hanke *et al. Heat-to-Connect: Surface Commensurability Directs Organometallic One Dimensional Self-Assembly.* ACS Nano. 5, 9093-9103. (2011).

[4.3]   P. Gambardella *et al. Co Growth on Pt(997): From Monatomic Chains to Monolayer Completion.* Surface Science. 449, 93-103. (2000).

[4.4]   P. Gambardella *et al. Ferromagnetism in One-Dimensional Monatomic Metal Chains.* Nature. 416, 301-304. (2002).

[4.5]   U. Perera, *et al. Spatially Extended Kondo State In Magnetic Molecules Induced by Interfacial Charge Transfer.* Phys. Rev. Lett. 105, 106601 (2010).

[4.6]   Stepanow, S. *et al. Mixed-valence behaviour and strong correlation effects of metal phthalocyanines adsorbed on metals. Phys. Rev. B.* 83, 220401 (2011).

[4.6]   P. Gargiani *et al. Spin and Orbital Configuration of Metal Phthalocyanine Chains assembled on the Au(110) Surface.* Phys. Rev. B. 87, 165407. (2013).

5 Cobalt Diphenyl Porphyrin Multilayers on Cu(110)

5.1 CoDPP Multilayer Structure

As an extension to the linked CoDPP molecular chain investigation, the magnetic behaviour of a multilayer sample of CoDPP on Cu(110) was chosen to be explored. The aims of this experiment were to investigate the magnetic behaviour of Co ions within CoDPP molecules which are not in direct contact with the Cu(110) surface. The intention was that the additional CoDPP layers would create different Co environments which are completely decoupled from the underlying Cu(110) surface. This will help to deduce whether the small XMCD signals which were measured for the horizontal and vertical sub-monolayer CoDPP systems were indeed due to strong interactions with the Cu(110) surface, causing the majority of the magnetic behaviour of the Co in these systems to be quenched.

This sample was prepared using large doses of the CoDPP material on Cu(110). Firstly, a complete monolayer of assembled CoDPP molecular chains was prepared on the surface as before and then an extra CoDPP layer was deposited on top by dosing for the same amount of time to produce a monolayer. The first layer was annealed, forming the CoDPP molecular chains, so that even though the Co ions present in this layer contribute to the measured XAS intensity of Co they do not contribute significant intensity to the XMCD signal as the previously measured XMCD signals of Co within the sub-monolayer coverages were very small (see **Chapter 4**).

Unfortunately, the resulting sample could not be imaged under STM; however, the XAS intensity across the Co region was increased by a factor ~2 compared to that of a single monolayer suggesting that additional CoDPP were present on the sample beyond the first layer, as intended. The molecules were anticipated to lie flat in the additional layers as observed in other investigations on porphyrin and phthalocyanine multilayers [5.1-5.3].

5.2 XMCD of CoDPP Multilayer

XAS spectra on the CoDPP multilayer were collected in the 765 to 820 eV energy range across the L_2 and L_3 absorption edges of Co at normal ($\theta = 0°$) and grazing ($\theta = 60°$) light incidence for both +6 and -6T magnetic fields at a target 1.5K with both positive and negative circularly polarised light. As mentioned, even though Co ions within the first layer of CoDPP do contribute to the measured XAS intensity, this contribution will be cancelled out when taking the difference between the positive and negative XAS spectra as the XMCD effect for this Co environment is minimal. As such any resulting XMCD signals which are present after taking this difference can be confidently ascribed to Co ions in the second layer.

The XMCD signals for the Co ion in the CoDPP multilayer sample showed large XMCD peaks at both the L_2 and L_3 absorption edges of Co for normal light incidence with respect to the sample (see **figure 5.1**). The XAS spectra of Co showed much more fine structure than the sub-monolayer systems for both positive and negative circularly polarised light giving rise to XMCD signals with multiple features at both the L_2 and L_3 Co edges. These XMCD features were all reproduced to a high degree of accuracy for opposite magnetic fields verifying that they are indeed magnetic effects (see **figure 5.2**). The size of the XMCD signal measured on the Co was also much larger than in any of the previous Co systems: ~3 times larger than the Co XMCD signals for the CoTPP system (**Chapter 3**) and ~10 times larger than the XMCD signals for the monolayer CoDPP system (**Chapter 4**). Interestingly, these XMCD signals showed positive and negative features at each absorption unlike the broad single peak present in CoDPP monolayers.
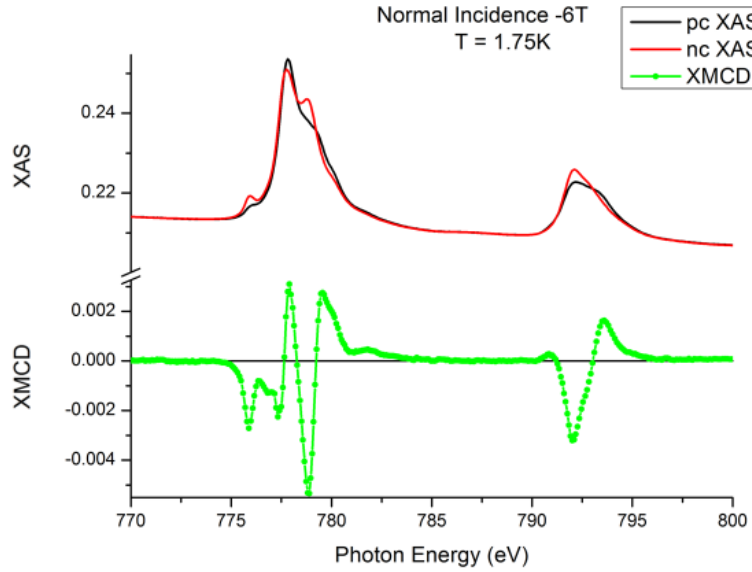
Figure 5.1: Normal Incidence (θ = 0°) XAS spectra of CoDPP Multilayers taken across the Co absorption range taken at 1.75K with -6T external magnetic field for positive circular (black) and negative circular (red) light polarisation at normal incidence. The resulting XMCD (green) shows multiple peaks at both the L_2 and L_3 absorption edges.
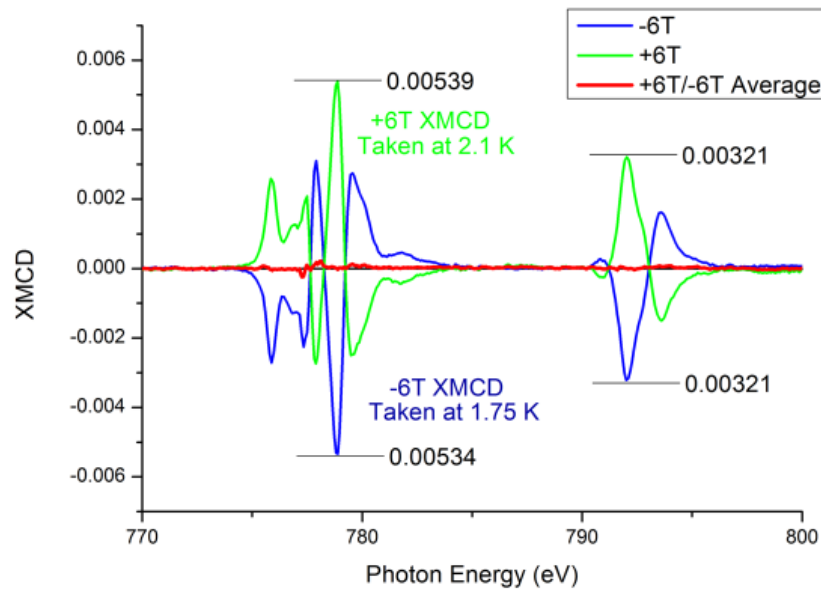

Figure 5.2: Normal Incidence (θ = 0°) comparison of XMCD spectra of CoDPP multilayers taken at 2.1K with +6T (green) applied magnetic field and -6T (blue). The average of the 2 curves (red) shows a flat line indicating very good signal to noise.

XMCD measurements were then conducted for the CoDPP multilayer system at grazing incidence ($\theta = 60°$) to explore if there was any magnetic anisotropy (**figure 5.3**). The -6T and +6T comparison spectra are also shown (**figure 5.4**). The XMCD signal at grazing incidence was drastically different from the XMCD signal measured at normal incidence and now exhibits entirely negative features at the L_3 edge and entirely positive features at the L_2 edge. This suggests that there is a difference between magnetic behaviour of the CoDPP multilayer system in plane and out of plane. The clear difference in the spectra between the normal and grazing geometries also suggests that the additional CoDPP molecules lie flat on top of the first CoDPP monolayer as expected. If they were randomly orientated then there would be no clear difference between the normal and grazing incidence measurements as there would be no directional dependence on the absorption process.
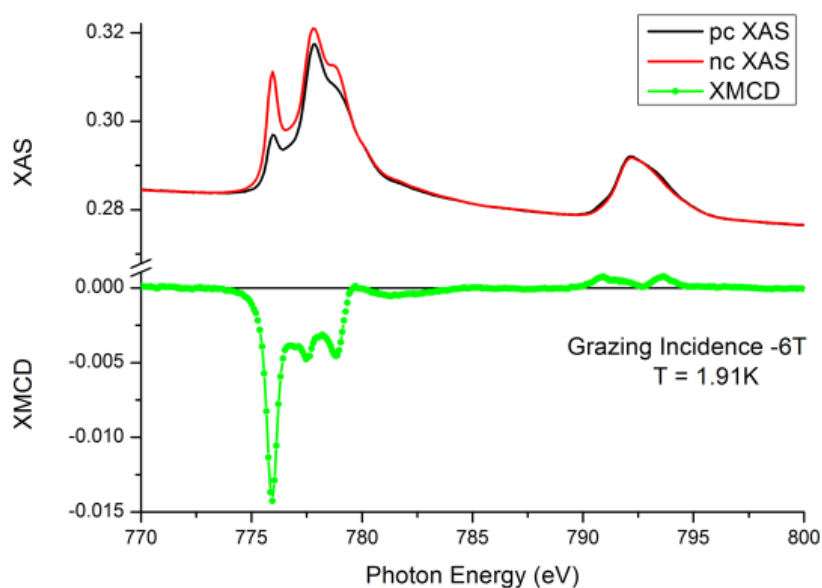

Figure 5.3: Grazing Incidence ($\theta = 60°$) XAS spectra of CoDPP Multilayers taken across the Co absorption range taken at 1.91 with -6T external magnetic field for positive circular (black) and negative circular (red) light polarisation at normal incidence. The resulting XMCD (green) shows multiple peaks at both the L_2 and L_3 absorption edges.
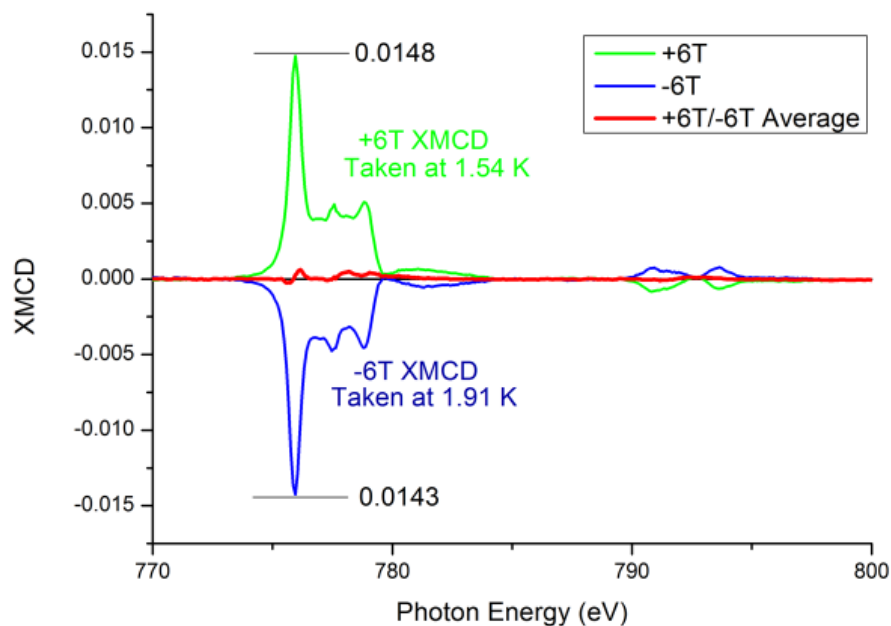
Figure 5.4: Grazing Incidence (θ = 60°) comparison of XMCD spectra of CoDPP multilayers taken at 2K with +6T (green) applied magnetic field and -6T (blue).

At grazing incidence, the individual features of the XMCD signal are the same for +6T and -6T external magnetic fields strengths, as seen with the normal incidence XMCD spectra. This shows that these spectra, even with their fine structure, are of purely magnetic origin. The XMCD signal observed at grazing incidence is indeed larger than that observed at normal incidence; however, the normal incidence XMCD spectra exhibits positive and negative contributions to the XMCD which aren't present at grazing incidence. Theoretical calculations such as multiplet simulations would be required to give a more complete picture of exactly which electronic orbital states are involved in the magnetic behaviour of the Co ion and reveal the precise origin of this anisotropy. These simulations could also predict the electronic orbital states for the Co ion within an isolated CoDPP molecule which would provide a useful comparison to the adsorbed CoDPP molecules.

5.3 Conclusions

The XMCD signals measured on the Co ion within the CoDPP multilayer sample were radically different than those measured for all of the sub-monolayer Co porphyrin samples. The magnitude of the XMCD signal was greatly increased, suggesting that the CoDPP molecules within the multilayer structure have been successfully decoupled from interactions the Cu(110) surface. The decoupling leads to a large magnetic moment present on the Co.

Comparing normal and grazing XMCD data shows that a large magnetic anisotropy is also present although the multilayer exhibits a much larger magnetic effect in plane (at grazing incidence) unlike the monolayer of CoDPP which shows a greater out of plane (at normal incidence) magnetisation (see **Chapter 4**).

The Co XMCD line shapes measured for the CoDPP multilayer system are almost identical to those which have been observed for other Co molecules which have also been decoupled from their underlying surfaces. Studies of Co phthalocyanine thin films on Au(111) [5.1], Co phthalocyanine thin films on Au(110) [5.4] and Co octaethyl porphyrin on Ni(111) with an intercalated graphene layer [5.5] all show similar Co XMCD fine structure. The duplication of these XMCD line shapes for each of these Co molecules despite using completely different underlying surfaces further suggests that the molecules are completely decoupled from the surface (either by using decoupling layers of the same molecule or an intercalated graphene layer).

This investigation on CoDPP multilayer system suggests that the surface and Co ion interaction is indeed a dominant factor in determining the magnetic properties of the Co and these interactions must be taken into consideration when designing and developing new magnetic molecular materials.

5.4 CoDPP Multilayers on Cu(110) References

[5.1] Stepanow, S. *et al. Mixed-valence behaviour and strong correlation effects of metal phthalocyanines adsorbed on metals. Phys. Rev. B.* 83, 220401 (2011).

[5.2] W. Auwärter *et al. Site-specific electronic and geometric interface structure of Co-tetraphenyl-porphyrin layers on Ag(111).* Phys. Rev. B. 81, 245403 (2010).

[5.3] J. Bartolomé *et al. Highly Unquenched Orbital Moment in Textured Fe-Phthalocyanine Thin Films.* Phys. Rev. B. 81, 195405. (2010).

[5.4] P. Gargiani *et al. Spin and Orbital Configuration of Metal Phthalocyanine Chains assembled on the Au(110) Surface.* Phys. Rev. B. 87, 165407. (2013).

[5.5] C. Hermanns *et al. Magnetic Coupling of Porphyrin Molecules Through Graphene.* Advanced Materials. 25, 25, 3473-3477. (2013).

6 Future Work

These experiments into molecular magnets on surfaces have been very encouraging: confirming that the Co centres of Co porphyrin systems can retain their magnetic properties when adsorbed onto the Cu(110) surface, demonstrates the feasibility of this molecular-based approach to spintronics. Modification of the molecular architectures of these systems has been shown to affect the magnetic behaviour of their Co centre and even leads to a quenching of it. Thus, by implementing further targeted modification of the Co porphyrin molecules it should be possible to gain a deeper understanding of the substrate-molecule interaction allowing for a more controllable handle on how to influence the resulting magnetic properties. The ultimate goal of this project is to be able to reliably predict and tailor the Co environment using these structural modifications so that more desirable and more useful magnetic properties are preserved on the Co. This opens up the opportunity to pursue investigations into how the magnetic moment on the active Co site of these molecules could be enhanced to provide magnetic behaviour comparable to the Co observed in decoupled systems.

The future work in this project can explore this idea by continuing to modify the molecular scaffolding of these Co porphyrin systems to optimise the strength of the Co magnetic moment and the decoupling of it from the metal surface. One particularly interesting system which could fulfil such a task is the tetra(mesityl) porphyrin (TMP) molecule on Cu(110) [6.1]. This system has been shown to produce 2-dimensional structures of molecules which can be covalently linked through the methyl groups on the outer phenyl rings upon annealing. These molecular structures exhibit a strong bonding mechanism which is crucially not mediated by the underlying surface. The structures can be seen to remain intact and move as a fixed unit across the surface suggesting that they are not tightly bound to the surface. The structure of this system is dominated by the intermolecular bonding mechanism and not the interaction

between the molecule and surface. This is particularly alluring from a molecular spintronics standpoint, as a surface structure which is dominated by the interaction between molecules could mean a weaker interaction between the molecule and the surface itself; the interaction which can cause the magnetic molecules to lose their magnetic properties. The behaviour of the TMP/Cu(110) system has been shown to be identical for TMP molecules complexed with a Co ion centre and thus a perfect candidate for this investigation which could be easily compared to the previously tested Co porphyrin systems studied in this project.

Finally, TMP and other organic molecules can be used as smaller components to build larger structures on surfaces as shown in [6.2]. This gives controlled growth of structures using specific molecular building blocks. Functionalising these molecular building blocks with magnetic material could pioneer a method of producing molecular spintronic devices.

6.1 Future Work References

[6.1]   In't Veld, M. *et al. Unique Intermolecular Reaction of Simple Porphyrins at a Metal Surface gives Covalent Nanostructures.* Chemical Communications 1536 (2008).

[6.2]   Haq, S. *et al. Versatile Bottom-Up Construction of Diverse Macromolecules on a Surface Observed by Scanning Tunneling Microscopy.* ACS Nano, 8, 9, 8856 (2014).